

Scanning Electron Microscopy

Yoosuf N. Picard, Carnegie Mellon University

Overview

General Uses

- Imaging of surface features from 10 to 100,000× magnification. Resolution is typically 1 to 10 nm, although <1 nm is possible.
- Depending on available detectors, the microscope enables differentiation of polycrystalline grains for unetched samples, microstructural components with and without surface etching, topographical features, crystallographic structure and material phase, extended defects, and local variations in material properties.

Examples of Applications

- Examination of metallographically prepared samples at magnifications well above the capabilities of optical microscopy
- Examination of fracture surfaces and deeply etched surfaces requiring depth of field well beyond that possible with the optical microscope
- Evaluation of phase and crystallographic orientation for individual grains, precipitates, microstructural constituents, and nanoscale particles
- Identification of the chemistry for micrometer and submicrometer features, such as inclusions, precipitate phases, and wear debris
- Mapping of elemental composition across micrometer to millimeter length scales
- Examination of semiconductor devices for failure analysis, critical length determination, and design verification

Samples

- *Form:* Any low-vapor-pressure (0.1 Pa, or $\leq 10^{-3}$ torr), conductive, solid material including particles, thin films, and bulk samples. Nonconductive solids can be imaged using a conductive coating. Uncoated nonconductive solids can be imaged using low-beam energy or using a variable-pressure/environmental scanning electron microscope (SEM). Wet and

fixed biological specimens can also be imaged using variable-pressure/environmental SEM.

- *Size:* Limited by the SEM specimen chamber size and stage travel. Generally, samples as large as ~20 cm (8 in.) can be placed in the microscope, but regions on such samples that can be examined without repositioning are limited to ~5 cm (2 in.).
- *Preparation:* Standard metallographic polishing and etching techniques are adequate for electrically conductive materials. Nonconducting materials are generally coated with a thin layer of carbon or metal. Samples must be electrically grounded to the holder, and fine samples, such as powders, can be dispersed on an electrically conducting adhesive. Samples must be free of high-vapor-pressure liquids, such as water, organic cleaning solutions, and remnant oil-based films, unless imaged inside a variable-pressure/environmental SEM.

Limitations

- Image quality on relatively flat samples, such as metallographically polished and etched samples, is generally inferior to the optical microscope below 300 to 400× magnification.
- Point resolution, although much better than the optical microscope, is inferior to the transmission electron microscope and the scanning transmission electron microscope.

Capabilities of Related Techniques

- *X-ray diffraction:* provides bulk crystallographic information
- *Optical microscopy:* faster, less expensive, and provides superior image quality on relatively flat samples at less than 300 to 400× magnification
- *Transmission electron microscopy:* provides similar information with superior resolution but is more expensive and requires thinned specimens

Introduction

A scanning electron microscope (SEM) is a type of instrument that magnifies and images sample surfaces through controlled rastering

of a highly focused electron beam across the area of interest. A variety of signals are produced, particularly backscattered and secondary electrons, as the electron beam interacts with the sample surface; these signals provide

local topographic and compositional information regarding the specimen. The SEM was invented in 1937 (Ref 1) and was first commercialized in 1965 (Ref 2). There have been continual improvements in SEM resolution,

dependability, ease of operation, and reduction in instrument size. Scanning electron microscopes are regularly used in materials research, forensics, failure analysis, geological studies, biological imaging, metallurgy, nanomaterials development, microelectronics, and fractography. Scanning electron microscopes are a common instrument in most materials characterization laboratories and are increasingly used for immediate, on-site metrology and quality control at the manufacturing floor.

The primary use of an SEM is to produce high-resolution images at magnifications unattainable by optical microscopy, while also providing direct topographic and compositional information. Magnifications up to $100,000\times$ or more are possible by modern SEMs. Scanning electron microscopes produce nanoscale-resolution imaging and mapping because the electron beam is focused to an ~ 1 to 10 nm sized probe. However, issues consider regarding electron probe size and depth sensitivity are the influence of accelerating voltage, beam current, sample composition, and the specific signal being detected. Signals are most commonly secondary electrons, backscattered electrons, and x-rays. Other possible signals that can be generated and detected in the SEM include visible light (cathodoluminescence), beam induced current, and Auger electrons.

This article provides detailed information on the instrumentation and principles of the SEM, including:

- Description of the primary components of a conventional SEM instrument
- Advantages and disadvantages of the SEM compared with other common microscopy and microanalysis techniques
- Critical issues regarding sample preparation
- Details on the physical principles regarding electron beam-sample interaction
- Mechanisms for many types of image contrast
- Details of SEM-based techniques
- Specialized SEM instruments
- Example applications using various SEM modes

The Microscope

Figure 1 illustrates the basic components of a typical SEM. The components can be categorized as the electron-optics column, the specimen chamber, the support system, and the control and imaging system. The electron beam is generated at an electron gun and accelerated toward the sample housed inside a specimen chamber, typically below the electron-optics column. Electromagnetic lenses below the electron gun focus the electron beam to a small probe at the sample surface. Scanning coils deflect the electron probe across the sample surface, and detectors housed either

in the specimen chamber or in the electron-optics column collect and report resultant signal intensity as a function of beam position. The SEM operator uses a computer to control the electron-optics, detectors, and a motorized stage for sample positioning. During SEM operation, a support system provides cooling water for the electro-magnetic lenses and maintains a low pressure within the electron-optics column and the specimen chamber using vacuum pumps.

Electron-Optics Column

The electron-optics column produces a narrowly divergent beam of electrons along the centerline of the column and steers the beam onto the sample surface. The major components of the electron-optics column are the electron gun, condenser lens, objective lens, and scanning coils.

Electron Gun

The electron gun contains the source of electrons and components that accelerate electrons to high energies. Two example guns are shown in Fig. 2. The electron gun produces a beam of electrons and focuses them to a spot of diameter, d_0 , and divergence half-angle, α_0 . The electron source is typically a tungsten hairpin, tungsten needle (Fig. 2), or a sharp-tipped crystal composed of a rare earth metal hexaboride (LaB_6 or CeB_6). Electron sources are generally classified as thermionic sources or field-emission sources. Thermionic

sources use heat to energize and release electrons from the source material; field-emission sources primarily rely on an electrostatic field for electron beam generation.

Thermionic emission sources heat a tungsten filament or La/CeB_6 crystal to temperatures of ~ 2500 or 1600°C (4500 or 2900°F), respectively. Current applied to the thermionic source resistively heats the material and energizes electrons from the sharpest radius-of-curvature (ROC) point on the source. The thermal energy imparted to the electrons at the surface must be sufficient to overcome the work function of the source material surface. Most metals reach or exceed their melting temperature before the electrons can overcome the work function. Tungsten has the highest melting temperature, lowest vapor pressure, lowest thermal expansion coefficient, and a very high tensile strength. Thus, tungsten is an ideal metal for an electron source. Tungsten filaments are bent into a "hairpin" shape with an ROC of $\sim 100\ \mu\text{m}$ (Ref 4). The LaB_6 is preferable to tungsten, because it has a lower work function and higher electron emissivity, thus requiring a lower operating temperature while emitting more electrons. The CeB_6 is less susceptible to contamination than LaB_6 and thus is seeing increased use. Stable hexaboride crystals have 90° cone tips with $\sim 15\ \mu\text{m}$ ROC.

Field-emission sources use a high electric field in the vicinity of the source. Field enhancement at the sharpest point in the source tunnels electrons off the source surface while also greatly localizing electron emission. Therefore, field-emission sources produce

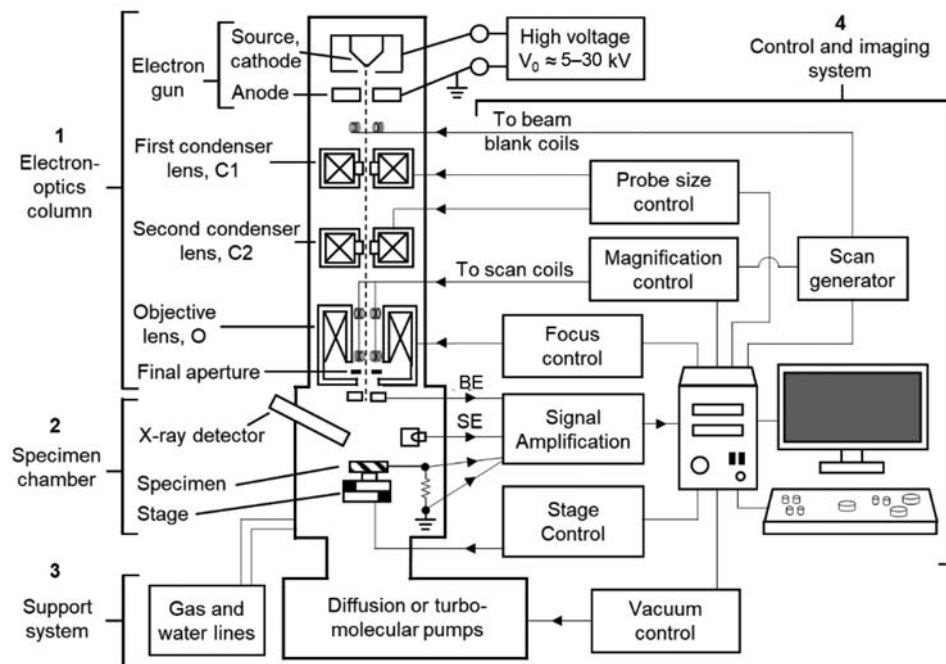


Fig. 1 Schematic of the basic components of a conventional scanning electron microscope. BE, backscattered electron; SE, secondary electron

much higher electron current densities (1000 to 10,000 A/cm²) than thermionic sources (1 to 10 A/cm²). **Field-emission sources, or emitters, are typically etched tungsten single-crystal needles with nanometer-sized ROCs. A ZrO coating on sharp tungsten needles (tens of nanometers ROC) creates a local Schottky barrier within the electric field, which lowers the work function of the tungsten (100) facet, thus requiring a much lower operating temperature (1500 °C, or 2700 °F) than a thermionic tungsten source. The ZrO-tungsten sources are called Schottky field-emission sources (Fig. 2b). Single-crystal (310) tungsten can be etched to achieve even sharper needle tips (few nanometers ROC), so the local electric field alone is enough to tunnel electrons off the tungsten (310) facet surface; these sources are called cold field-emission sources, since they operate at room temperature.**

Within the electron gun, **electron extraction from the electron source requires a voltage potential between the source (cathode) and another electrode in proximity (anode). The anode accelerates the electrons to a specific kinetic energy and directs the initial electron beam trajectory down the electron-optics column. The cathode is negatively biased, and the accelerating anode is positively biased. For thermionic sources, the cathode is considered "hot," and another electrode with an aperture is positioned near the tungsten filament or hexaboride crystal. The aperture electrode, the Wehnelt cylinder, is negatively biased to a few hundred volts and functions as an electrostatic lens, which helps control electron extraction from the thermionic source. Farther away, the accelerating anode is strongly biased positive. For field-emission guns (FEGs), the appreciable voltage gradient present between the anode and the cathode provides a sufficiently strong electrostatic field, so the much sharper tip of the field-emission sources produces adequate field enhancement for electron extraction. A negatively biased electrode, the suppressor, helps localize the electron-extraction region at the source, while a positively biased extracting anode farther away pulls the electrons toward the accelerating anode.**

The most important parameter distinguishing these four types of electron guns is the brightness, β :

$$\beta = \frac{I}{\left(\frac{\pi d_0^2}{4}\right)(\pi \alpha_0^2)} \quad (\text{Eq 1})$$

where β equals the amount of current, I , focused on an area, $\pi d_0^2/4$, entering and exiting this area through a solid angle, $\pi \alpha_0^2$ (Ref 5). Increasing β improves the overall performance of the SEM. The value of β is primarily a function of the electron source material and the type of electron gun. Cold FEG sources provide the highest β values but require ultra-high-vacuum conditions, because the room-temperature emitter is more susceptible to

contamination. Contaminants that attach to the cold FEG source are removed by flashing the emitter with bursts of current. Cold FEG sources greatly increase SEM instrumentation costs but are highly stable and long-lasting sources. Schottky FEG sources produce lower β values than cold FEG sources, but they are also less expensive and require less stringent vacuum demands. Thermionic sources have much lower β values than FEG sources but are also much cheaper. They do require occasional source replacement, particularly the less expensive tungsten filaments as opposed to the more expensive but higher-brightness hexaboride crystals. Table 1 compares important properties for the four types of electron sources.

Lenses

Lenses within electron microscopes use electromagnetism to focus electron beams. Electromagnetic lenses (Fig. 3a) consist of copper wire windings inside an iron fixture, which is carefully machined to specific dimensions with pole pieces designed to localize magnetic fields. Current passed through the windings of copper wire magnetizes the iron and produces a magnetic field, which is radially symmetric about the lens axis. As an

electron moves through the magnetic field, it experiences a radial force inward, which is proportional to the Lorentz force, $v \times B$, where v is the electron velocity, and B is the magnetic flux density. The function of the pole pieces is to produce progressively higher density magnetic flux lines farther away from the lens axis. Electrons traveling parallel, but at different distances to the lens axis, experience different inward Lorentz forces, so that they converge at the focal plane. The resulting lensing action is comparable to the function of an optical lens, in which a ray parallel to the axis of the lens is bent toward the lens axis. Eventually, the ray meets the lens axis at a distance below the lens principal plane that corresponds to the focal length, f , of the lens (Fig. 3b).

For an optical lens, f is determined by the lens surface curvature and refractive index of the lens medium; the focal length is fixed. The focal length of an electromagnetic lens depends on two factors: the acceleration voltage (which determines the electron velocity, v) and the amount of current passing through the copper winding (which determines the flux density, B). Therefore, the operator can control and tune the electromagnetic lens focal length by adjusting the currents supplied to them; an

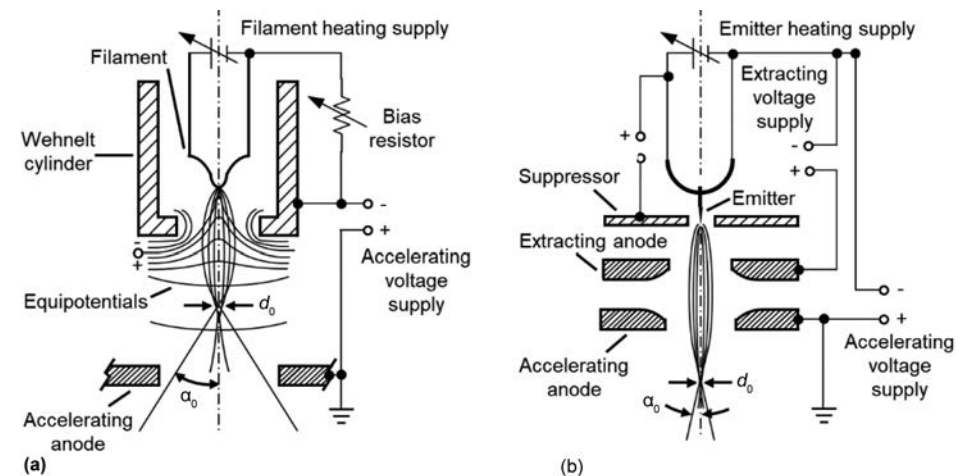


Fig. 2 Schematics of conventional (a) thermionic tungsten hairpin filament gun and (b) Schottky field-emission gun. Adapted from Ref 3

Table 1 Comparison of electron source properties

Property	Thermionic tungsten filament	Thermionic LaB ₆ /CeB ₆	Schottky field-emission ZrO/W (100)	Cold field-emission tungsten (310)
Brightness (β), A/cm ² · sr	10 ⁶	10 ⁷	5 × 10 ⁸	10 ⁹
Crossover or virtual source diameter (d_0), nm	>10 ⁴	>10 ³	15–25	3–5
Work function, eV	4.5	2.6/2.4	2.8	4.3
Energy spread, eV	1–3	>1	0.3–1	0.2–0.3
Operating temperature, °C (°F)	2500 (4500)	1600 (2900)	1500 (2700)	25 (75)
Typical service lifetime, h	40–100	1000/1500	>2000	>2000
Operating vacuum, Pa (torr)	10 ^{−4} (7.5 × 10 ^{−7})	10 ^{−6} (7.5 × 10 ^{−9})	10 ^{−8} to 10 ^{−9} (7.5 × 10 ^{−11} to 7.5 × 10 ^{−12})	10 ^{−9} to 10 ^{−11} (7.5 × 10 ^{−12} to 7.5 × 10 ^{−14})

Source: Ref 6

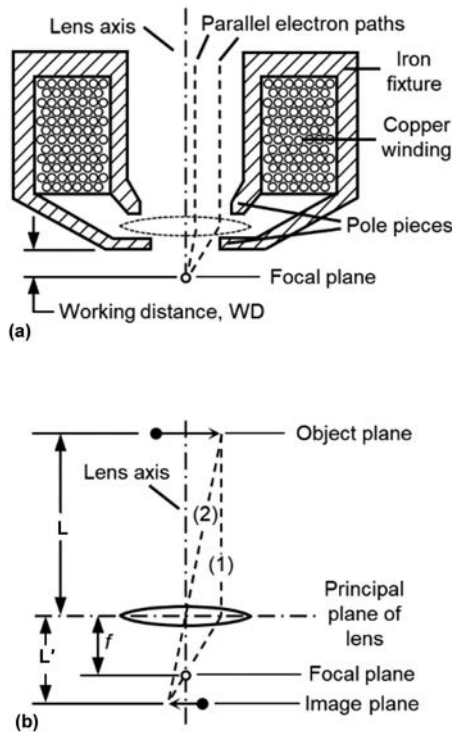


Fig. 3 (a) Schematic cross section of conventional electromagnetic objective lens. (b) Ray diagram of a standard lens. Magnification, $M = L'/L$

increase in current increases the overall radial force experienced by all electrons within the beam and thus reduces f .

Rather than achieving magnification, the purposes of lenses in an SEM is to reduce the initial electron beam diameter, d_0 , to a much smaller diameter at the sample surface. Therefore, SEM lenses demagnify the electron beam diameter, as illustrated in Fig. 3(b). The arrow in the object plane is reproduced upside down in the image plane, and the arrow-tip image can be located by following rays (1) and (2). The magnification is $M = L'/L$; as focal length f is reduced, the value of L' is reduced, reducing magnification, M . Therefore, if the length of the arrow is taken as the electron beam diameter, d_0 , produced by the gun, then the beam diameter, d_1 , after passing through the first condenser lens is $d_1 = M_1 d_0$, where M_1 is the magnification of the first condenser lens.

Figure 4 shows the coupling of two condenser lenses and one objective lens; the object plane for a given lens is the image plane from the lens above it. The net result is that the diameter of the electron beam at the sample surface, d_3 , is:

$$d_3 = d_0 \cdot M_1 \cdot M_2 \cdot M_3 \quad (\text{Eq 2})$$

where M_1 , M_2 , and M_3 are the demagnification factors for each lens. Spot size, or actual beam size, on the sample surface, d_s , is somewhat

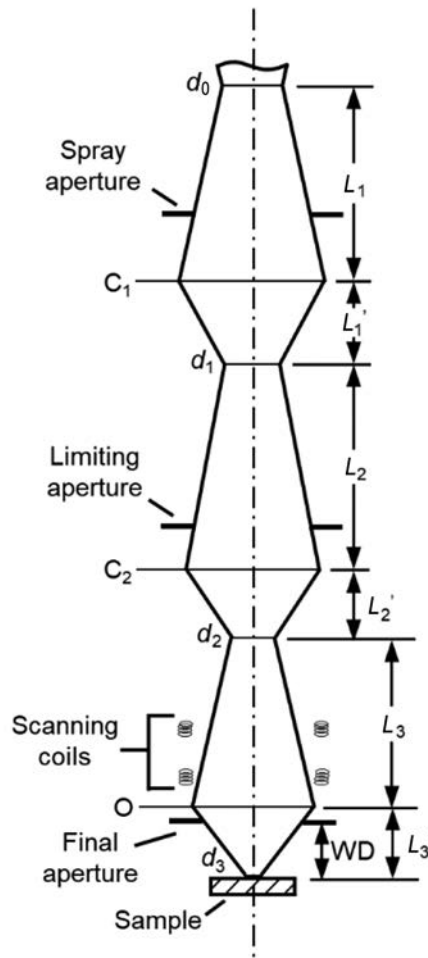


Fig. 4 Ray diagram of beam demagnification by three lenses in a scanning electron microscope. WD, working distance

larger than d_3 due to lens aberrations. Considering a typical value of $d_0 = 15 \mu\text{m}$ for a thermionic tungsten filament gun, and the value of d_3 may reach 15 nm , this corresponds to $M_1 \cdot M_2 \cdot M_3 = 1000$. Note that the $1000\times$ demagnification has no direct relationship to the actual magnification achieved by the SEM using scanning coils, as described later. Also, apertures located near each lens serve to limit the angular spread of the electron beam as it progresses along the electron-optics column axis. Apertures are metal discs with machined holes of various diameters ranging from 5 to $1000 \mu\text{m}$. The user can often select aperture sizes to adjust beam convergence angle, depth of field, and beam current (number of electrons) arriving at the specimen.

The sample position relative to the objective lens focal plane, L_3' in Fig. 4, can also be independently adjusted by the user via stage positioning inside the specimen chamber. The distance of the focal plane below the bottom of the objective lens, and/or final aperture, is termed the working distance (WD). The center

axis of the electro-optics column is typically considered the z -axis direction with respect to sample orientation. If the sample surface position is changed vertically along the z -axis, the objective lens current must be adjusted to have L_3' fall on the sample surface. The objective lens current adjustment is the focusing procedure performed by the operator to obtain the sharpest image possible. Because f_3 and therefore L_3' are functions of current applied to the objective lens, a unique value of WD corresponds to objective lens current; WD is often displayed on the control system. Therefore, once the operator ensures the sample is at focus, the associated WD value can often serve as a useful z -axis value for the stage position.

Stronger lens focusing produces a smaller beam diameter. Therefore, image resolution improves as WD is decreased. In the past, special high-resolution SEMs used an immersion lens that greatly reduced WD by positioning the sample inside the objective lens. Modern SEMs might incorporate a snorkel lens, which extends the electromagnetic field below the objective lens pole piece, effectively immersing the sample within the focusing lens field. These modes greatly reduce f_3 and further reduce d_3 to enhance resolution.

As mentioned previously, the actual beam spot size at the sample, d_s , is larger than d_3 due to lens aberrations, including spherical aberration, chromatic aberration, and astigmatism. Of these, only astigmatism is regularly corrected in a typical SEM and primarily for the objective lens, since it is the probe-forming lens of the SEM. Astigmatism arises from imperfections in the machined soft iron pole piece of the electromagnetic lenses, which diminish the radial symmetry of the electro-magnetic field produced by the lens. This leads to a larger beam diameter at the lens focal plane. To improve the field radial symmetry, an array of independently controlled stigmator coils are arranged around the inside circumference of a lens. Each coil produces additional magnetic field lines, enabling the user to adjust and balance the overall electromagnetic lens action of the entire assembly. Figure 5 illustrates the effect of astigmatism on SEM images of gold nanoparticles. When the sample is slightly out of focus, features exhibit a stretched appearance because of the elongated beam diameter overlapping adjacent image pixels. The directionality of the stretching is orthogonal when going from an underfocus to overfocus condition or vice versa. Adjusting the stigmators to ensure the beam diameter is circular in underfocus and overfocus conditions serves to reduce the beam size when at focus. For this reason, Fig. 5(d) exhibits sharper image quality than Fig. 5(a), even though both images are technically in focus. Astigmatism correction for the objective lens is a common task during SEM operation, particularly for higher magnifications where it becomes crucial to obtain the smallest possible spot size, d_s .

It may be necessary to increase the number of electrons arriving at the sample, even at the expense of producing a larger spot size. More electrons impinging the sample lead to greater overall signal, which is particularly desirable for x-ray analysis and backscattered electron imaging. The condenser lens immediately above the objective lens enables controlling both spot size and number of arriving electrons, as shown in Fig. 6. The L_2' and d_2 decrease with increasing condenser lens strength. For the same objective lens strength, a smaller d_2 beam diameter produces a smaller d_3 beam diameter at the sample surface. However, as the cross-over point for the condenser lens moves farther away from the objective lens and objective aperture, fewer electrons can pass through the objective aperture. Therefore, any reduction in the spot size accomplished by increasing condenser lens strength also results in fewer electrons arriving at the sample surface. Sacrificing beam current for smaller spot size is a standard trade-off in the SEM.

Scan Coils

The main function of scan coils is scanning the focused electron beam across the sample surface to produce an image. Two sets of scan coils located in the bore of the objective lens cage shown in Fig. 1 perform the scanning function. The coils, further detailed in Fig. 7, deflect the beam to scan over a square area of size $r \times r$ on the sample surface. The scanned area is generally termed the raster. Although the beam is shown in Fig. 7 as a line, it is diverging as it passes through the scan coils. However, because the divergence half-angle is in the milliradian range, representation as a line is reasonable. For simplicity, Fig. 7 depicts the scanning process at approximately midway during the formation of a single frame.

Scanning electron microscopes achieve magnification using this double-deflection system, with the beam deflected by the Lorentz force produced by low-impedance coil windings driven by a low-voltage power supply. The scan generator produces a voltage across each coil pair. The upper scan coil pair, X_1 , produces a magnetic field at time 1, which provides a Lorentz force that deflects the beam to the right through angle θ_{\max} . The lower scan coil pairs, X_2 , deflect the beam back to the left through angle $2\theta_{\max}$ so it strikes the sample at the left edge of the raster. The $X_1 - X_2$ voltage signal decreases stepwise with time, as shown at the upper left of Fig. 7. For each short time interval, termed dwell time, the beam sits at a single position on the sample surface. From time 1 to time 5, the beam scans along the line of length r on the sample surface.

At time 5, the $X_1 - X_2$ scan voltage “flies back” quickly to 1', causing the beam to return rapidly to the left side of the raster.

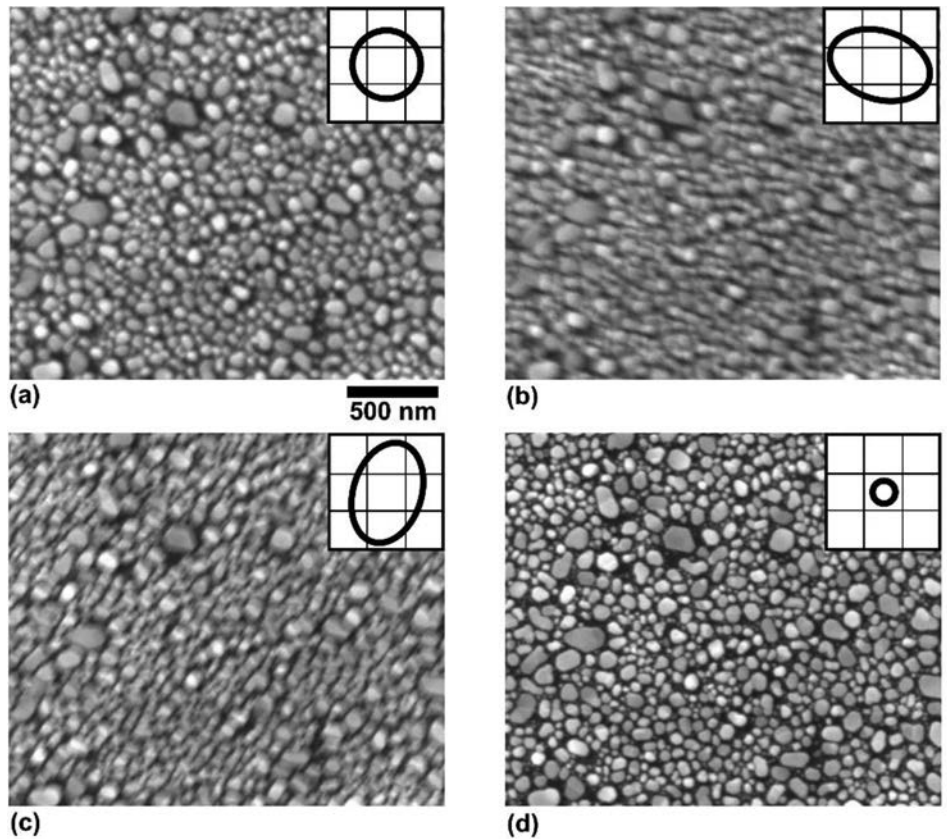


Fig. 5 Scanning electron microscope images of gold nanoparticles obtained before astigmatism correction. (a) At focus. (b) Underfocus. (c) Overfocus. (d) At focus after astigmatism correction. Inset depicts electron beam spot size relative to pixel size.

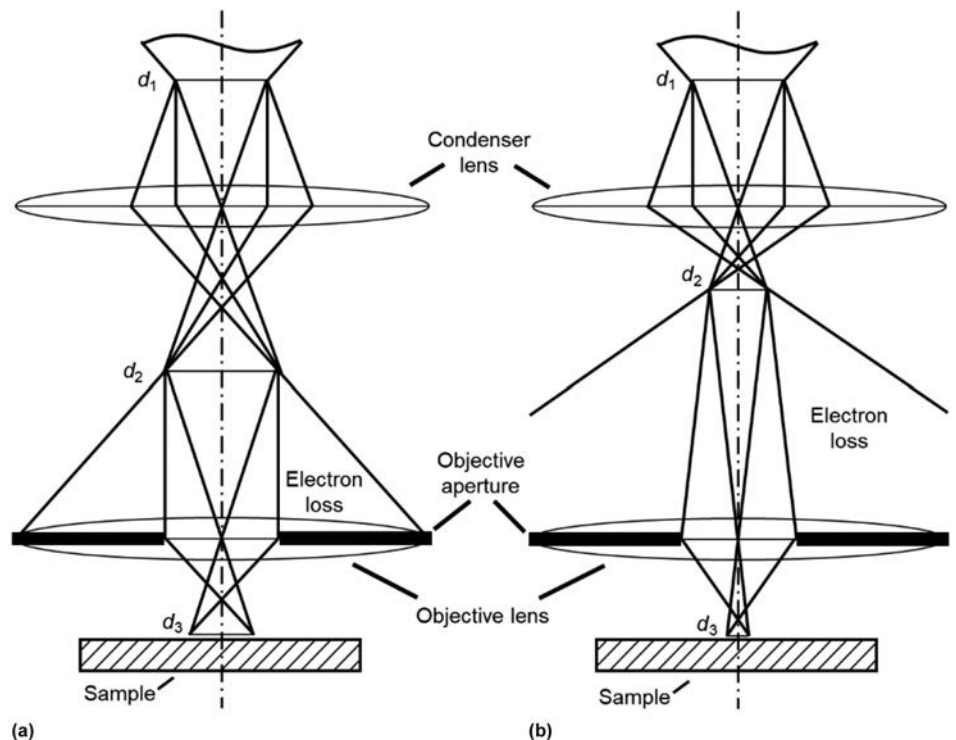


Fig. 6 Illustration of (a) lower condenser lens strength producing a larger beam diameter, d_3 , of sample surface with more electrons. vs (b) increased condenser lens strength producing a smaller beam diameter, d_3 , at sample surface but with fewer electrons. Adapted from Ref 4

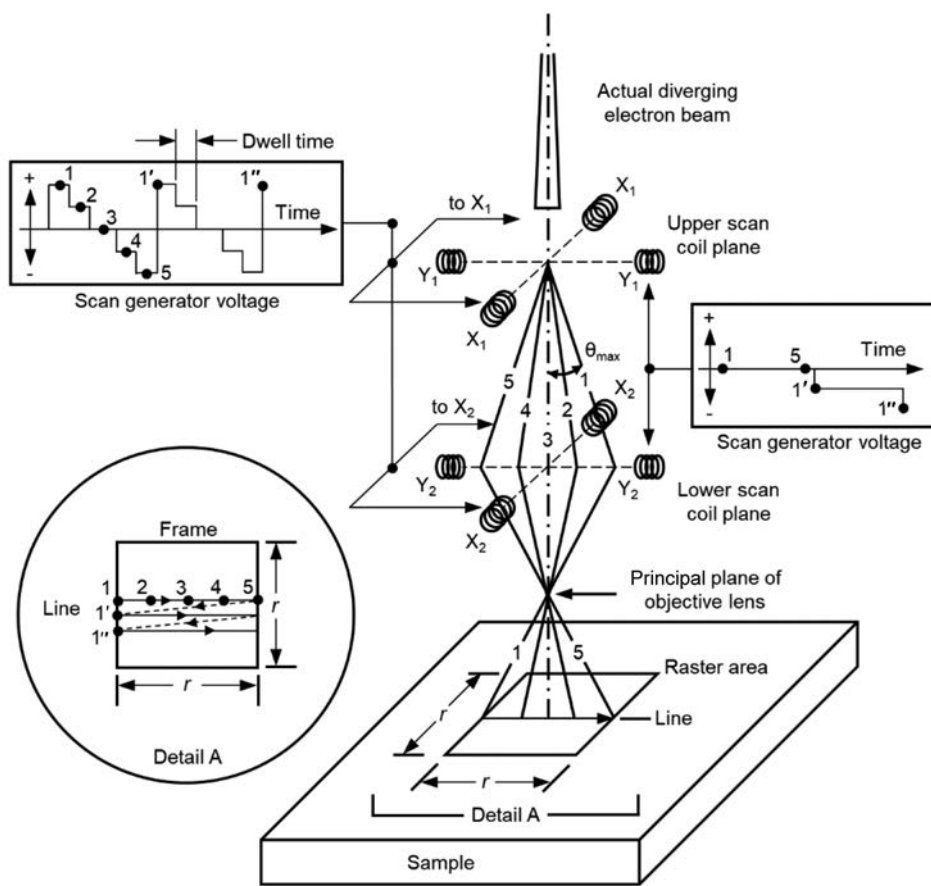


Fig. 7 Diagram of double-deflection system showing progressive line scanning to produce a frame of size $r \times r$

Concurrently, Y_1 and Y_2 coil pairs now have a small voltage, causing a small deflection so a new line begins at position 1' in detail A of Fig. 7. During the fly-back time from 5 to 1', the beam moves along the dashed line shown in detail A in Fig. 7. The next line is scanned, and the process is repeated until a full raster is accomplished and a single frame is produced. The scan generator controls the frame size, number of lines within each frame, number of positions on each line, and the dwell time for each position on each line. Each position corresponds to an individual pixel in the resultant digital image. The pixel value in terms of gray-scale depends on the relative signal intensity collected during the dwell time interval.

The magnification, M , achieved by the SEM is simply the ratio of the displayed size to the raster size, r . For example, consider a 50 cm (20 in.) screen digital display that is 44.3 cm wide by 24.9 cm high (17.5 by 10 in.) and projects in 16:9 aspect ratio with 1600×900 pixels. If the raster size matches the aspect ratio, but over a much smaller region corresponding to $32.0 \mu\text{m}$ by $18.0 \mu\text{m}$ of the sample surface, then the magnification is $M = 44.3 \text{ cm}/0.0032 \text{ cm}$ or $M = 24.9 \text{ cm}/0.0018 \text{ cm}$, which corresponds to a magnification of $\sim 13,800\times$.

The SEM magnification is determined by the user-controlled size r of the raster via the scanning coils. Higher magnification simply requires reducing r through smaller variations in the scan generator voltage, thus decreasing the deflection angles θ_{max} and $2\theta_{\text{max}}$. The double-deflection system ensures the electron beam passes through the objective lens plane consistently at the same point on the electro-optics axis. Therefore, the objective lens current can be maintained, and the sample generally remains in focus as the magnification is altered. The SEMs typically enable controlling and tuning the directionality of the raster, enabling scan rotation that effectively rotates the apparent image on the digital screen. Sometimes reduced areas within the frame can be selected, often so microscope parameters can be tuned based on a single feature of interest within the field of view. If the working distance is increased with no change to scanning conditions, then the raster size increases and M correspondingly decreases; the lowest available magnification depends on the WD used.

Because the objective lens current, is a known function of WD for a focused sample, magnification is reported based, in part, on this lens current; SEM instruments show the

magnification directly on the digital display. More importantly, a scale bar is also provided. The scale bar provides a direct correlation between the pixel units of the digital image to the actual physical size of the raster and associated surface features being imaged in the SEM. Commercially available specimens with patterned features of well-established physical sizes are used to calibrate any SEM. The calibration step is crucial to ensure the accuracy of both the displayed magnification and associated scale bar.

Specimen Chamber

The specimen chamber of an SEM contains the sample and the primary detectors for imaging and analysis. Specimen chambers range in size from small enclosures used for tabletop SEMs housing centimeter-sized samples, to medium-range sizes typical for research-grade SEMs capable of handling up to $\sim 20 \text{ cm}$ (8 in.) samples, to large enclosures designed to handle specimens up to meters in size. The chambers are vacuum capable enclosures usually constructed of nonmagnetic stainless steel. The inside chamber walls must be maintained dry and free of residue to facilitate obtaining the necessary low operating pressures during imaging and analysis, while also minimizing sample surface contamination. Plasma cleaners can be attached to SEM chambers to enable removal of residual contamination during operation. Specimen chambers can be vented to atmosphere and opened for sample loading. For SEMs that regularly operate at high-vacuum conditions $< 1.33 \times 10^{-5} \text{ Pa}$ ($< 10^{-8} \text{ torr}$), a load-lock apparatus is attached to the specimen chamber. This enables the operator to load the sample into a secondary chamber that is pumped to low pressures before sample insertion to the main specimen chamber, thus avoiding the need to vent the entire chamber to atmosphere.

Stage

When the sample is loaded into the SEM specimen chamber, it sits on a motorized, computer-controlled stage. Some SEMs with manual micrometer control and no motorization are still in use, but they are becoming increasingly obsolete. The SEM operator positions the sample in the electron beam path and selects regions of interest for imaging and/or analysis. Simple SEM systems may only have a two-axis stage, which enables x - and y -axis control of the sample position. More advanced SEMs typically have a five-axis stage for x -, y -, and z -axis positioning plus sample rotation and tilt control. As mentioned previously, the z -axis is conventionally defined parallel to the center axis of the electro-optics column. The y -axis is often oriented relative to the direction of the secondary electron detector. In an analytical SEM, the y -axis may be oriented with respect to the energy-dispersive spectrometer.

Detectors

Standard detectors are mounted on the SEM chamber, as shown in Fig. 8, and are designed to detect secondary electrons (SEs) and/or backscattered electrons (BEs), which is discussed later in this article. Most standard SEM detectors are scintillation and solid-state detectors. Historically, the most used detector has been the Everhart-Thornley detector (ETD) (Ref 7), which consists of a scintillator coupled to a photomultiplier tube with a Faraday cage typically biased by a positive voltage (50 to 300 V) to attract and enhance the signal of SEs. The ETDs are often mounted a few centimeters away from the sample surface and employ the Faraday cage to enhance SE capture. Alternatively, scintillation crystal-based detectors, such as the Robinson detector (Ref 8), are positioned directly above (within a few millimeters of) the sample surface, usually just below the pole piece. These scintillation detectors can have larger collection areas and provide high BE collection yields.

Another common method for BE detection in this geometry is using semiconductor-based solid-state detectors, which are often segmented so the BE signal to different regions of the detector can be isolated and mixed. The resultant BE images from such detectors can be added, subtracted, and/or mixed to enhance compositional contrast, topographic contrast, and quantitative surface information for three-dimensional reconstruction. Pole-piece-positioned scintillation and solid-state detectors have an

orifice in the center to enable the incoming electron beam arrival to the sample surface. Many pole-piece-positioned detectors are mounted on a retractable device so they can be inserted or removed by the operator without venting the SEM chamber and manually positioning the detector.

A newer development for SEM detectors is positioning scintillation and solid-state detectors below the sample or above the sample inside the electron-optics system, as shown in Fig. 8. To detect electrons emanating from the underside of a specimen, it is necessary to thin specimens to ~100 nm thickness and use higher acceleration voltages (>20 kV) so samples are somewhat transparent to the incoming electron beam. This scanning transmission electron microscopy (STEM) mode and associated STEM detectors can be used to detect BEs (dark field) and transmitted electron beam signal (bright field). The STEM imaging provides enhanced imaging resolution and a variety of contrast mechanisms, which provides complex information (Ref 9, 10).

In-lens and in-column detectors selectively detect SEs and BEs that have a high take-off angle from the sample surface. An internal direct current bias inside the electron-optics system facilitates SE collection, while in-lens BE detectors rely on line-of-sight positioning of the sample for optimized detection. **In-lens detectors are particularly useful when imaging at low accelerating voltages and small WDs.**

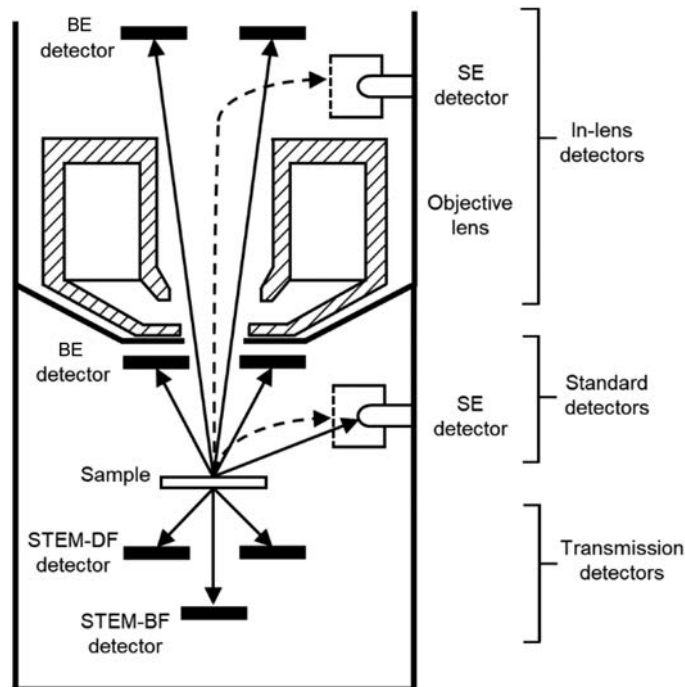


Fig. 8 Schematic of various detector positions and associated electron trajectories for secondary electrons (SE; dotted arrows) and backscattered electrons (BE; solid arrows). STEM, scanning transmission electron microscopy; DF, dark field; BF, bright field

Detector efficiencies, ϵ , relate the performance of various electron detectors (Ref 11). In-column SE detectors yield ϵ values of ~0.6, far superior to conventional ETDs with ~0.1 to 0.05 efficiencies (Ref 12).

Support System

The required support system varies depending on the comparative image resolution and functional capabilities of the SEM. At a minimum, an SEM requires electrical power to supply the voltage and current required for the electron beam. Water lines may be required to cool the electromagnetic lenses. **Air or dry nitrogen is often used as a purging gas during the venting process.** Higher-resolution SEM instruments require an air table to dampen external vibrations.

An SEM also **requires** that both the electron-optics column and specimen chamber operate under high **vacuum conditions to ensure the electron beam is not scattered by gas molecules before arriving at the sample surface.** Therefore, the sample and mounting materials used to hold the sample in place must not have a high vapor pressure. A valve isolates the electron-optics column from the specimen chamber so the electron-optics column remains under vacuum during sample loading. This arrangement enables the electron gun to remain activated during specimen exchange, hastening turnaround time for changing specimens. For SEMs that require more stringent specimen chamber vacuum conditions, an additional sample-loading chamber enables inserting a sample into the specimen chamber without venting the entire chamber to atmosphere.

Different vacuum pumps are used to achieve different levels of vacuum for SEMs. Mechanical rotary pumps are typically used as a first-stage pump for initial evacuation of SEM specimen chambers down to 10^{-2} Pa (7.5×10^{-4} torr). Oil-based diffusion pumps and **cleaner turbomolecular pumps can further reduce pressures down to 10^{-5} to 10^{-7} Pa (7.5×10^{-7} to 7.5×10^{-9} torr), respectively.** Within the electron-optics column, ion getter pumps attain low pressures in the 10^{-8} Pa (7.5×10^{-10} torr) range.

Control and Imaging System

Control of the modern microscope involves a computer-user interface that enables electron beam manipulation, image acquisition, sample positioning, detector selection, and vacuum operation. The user can define the probe based on the acceleration voltage and spot size. A scan generator enables the user to select magnification, dwell time per pixel, and number of pixels per image; a frame grabber enables digital image capture and storage on the computer. Quality of the images is a function of both the number of pixels to provide

sharpness and the contrast. Optimizing focus through control of the objective lens current and/or specimen z-position further enhances image sharpness. Contrast can be enhanced by several factors, depending on the conditions of the electron probe, the type of signal detected, and the detector gain settings used.

Image Formation

Image formation is based on detected variations in the collected signal as a function of probe position as the electron beam is scanned across the sample surface. Figure 9(a) depicts a single line scan from positions 1 to 5 across a topographical bump on a surface. Possible trajectories of SE paths are shown for beam positions 2 and 4, and the SE paths can curve to the ETD due to the positively biased Faraday cage. However, many electrons from position 2 may never reach the SE detector due to their initial escape trajectory. Consequently, the SE signal is much higher at position 4 due to its direct line of sight to the detector. Figure 9(b) illustrates the variation in SE signal intensity as the beam is scanned across the bump, demonstrating how SE signal variation can be correlated to a topographical feature.

If multiple line scans are conducted, a two-dimensional representation of detected SE signal intensity can be presented as an array of pixels, each with a corresponding grayscale value. During SEM operation, the scan generator that drives the scan coils of the electron column coordinates with both the detector and the digital display readout. Therefore, as shown in Fig. 9, there is a synchronous positioning of the beam within the raster on the sample surface and the pixel position defined in the digital display.

To prepare a picture, the grayscale intensity of the individual pixels is modulated proportionally to the magnitude of the signal from the detector. When the beam is at position 2 on the sample, the signal is low; therefore, the pixel corresponding to point 2' on the digital display is dark. Similarly, the pixel at position 4' is bright, because position 4 faces the detector and provides a larger signal. Therefore, as the beam scans the full raster, a full frame is produced on the digital display; the side of the bump facing the SE detector appears bright and the opposite side dark.

An image can be prepared with the signal from any of the detectors shown in Fig. 8. The topographic contrast in the image when using the SE signal is like the optical case in which the eye is above the sample and a light shines on the sample surface from the direction of the detector position. The side of the bump facing the light source would appear bright, and the other side would be dark, as illustrated in Fig. 9(c). Therefore, assuming the source of contrast is topographic, observed shadowing effects in SE or BE images from the SEM are comparable to the effects of typical light-source images obtained by optical microscopy.

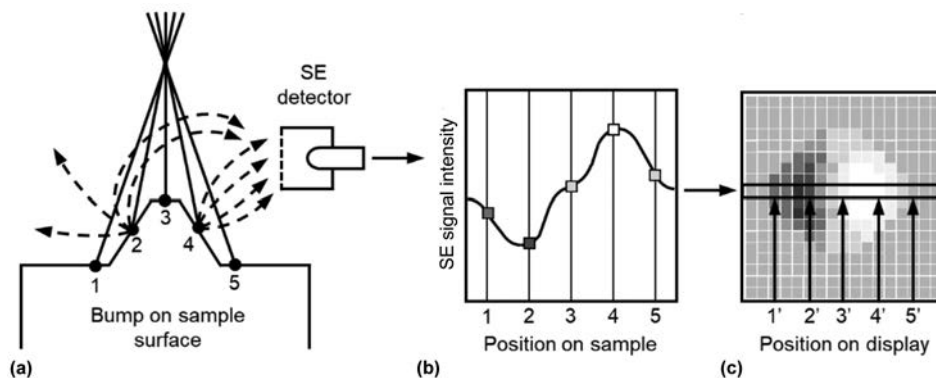


Fig. 9 Illustrations depicting (a) a line scan of the electron beam across a bump, (b) the synchronous secondary electron (SE) signal intensity, and (c) pixel grayscale values in the resultant digital image

Contrast

Contrast is the quantitative differences in grayscale values for different pixels. Percent contrast can be determined as:

$$C(\%) = (S_2 - S_1) / (S_2 + S_1) \times 100 \quad (\text{Eq } 3)$$

where S_2 and S_1 are signal intensities at two arbitrary raster positions. Information is contrast that corresponds to physical characteristics of the specimen surface. Therefore, extracting information from SEM micrographs requires evaluation and interpretation of signal differences (ΔS) attributed to features of interest as opposed to random signal fluctuations, called noise (N).

Figure 10 presents an example SEM micrograph of gold nanoparticles and corresponding grayscale signal intensity (S) for a single line of 48 pixels. Secondary electrons (SEs) emitted when the beam strikes the sample surface are weakly bound electrons emitted from near the surface (see later discussion on beam-sample interactions). The yield of SEs is increased either by the material properties of the surface or by decreasing the angle the beam makes with the sample surface, which is termed the tilt angle. As the beam moves from points 3 to 4 in Fig. 10, there is an optimally large change in material properties (carbon to gold) and beam surface angle geometry. Consequently, ΔS between points 3 and 4 is large and the contrast, $\Delta S/S$, is highest. Between points 4 and 5, the beam is scanned across the top of a single gold particle, yet some S variation is detected despite the smooth surface. The fluctuation in S is attributed to noise. When the signal change, ΔS , exceeds N by a factor of at least 5 (Ref 13), the signal change is conventionally considered meaningful in the SEM image.

Brightness

Brightness and contrast are image settings that the user can tune through control of the detector signal gain. Figure 11 demonstrates the effect of brightness and contrast gain

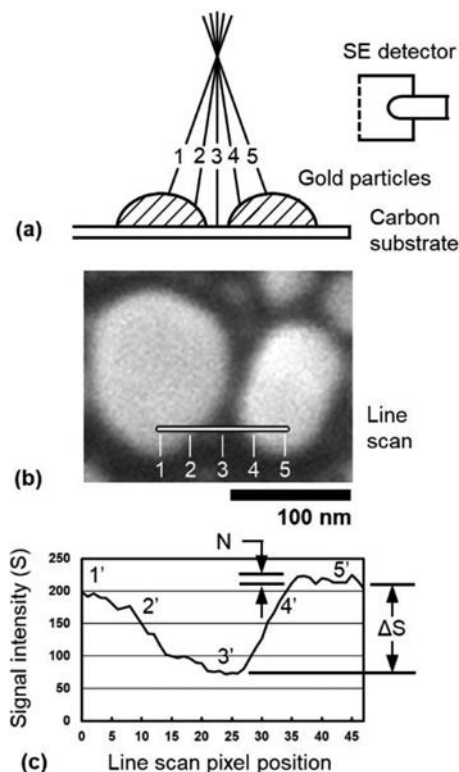


Fig. 10 (a) Illustration of electron beam scanning across gold nanoparticles. SE, secondary electron. (b) Scanning electron micrograph of gold particles. (c) Secondary electron signal intensity, S , as a function of pixel position from line scan denoted in (b)

adjustments to the resultant image. For all five images in Fig. 11, a yellow plot termed the waveform is superimposed on the image, which represents a single line of pixel grayscale intensity plotted between 0 and 255, similar to Fig. 10(c). All waveforms in Fig. 11 correspond to a centrally located horizontal line of pixels. Figure 11(c) presents an optimized brightness and contrast setting. All pixel intensities fall within the 0 to 255 range. As such, the profile of the waveform spans all

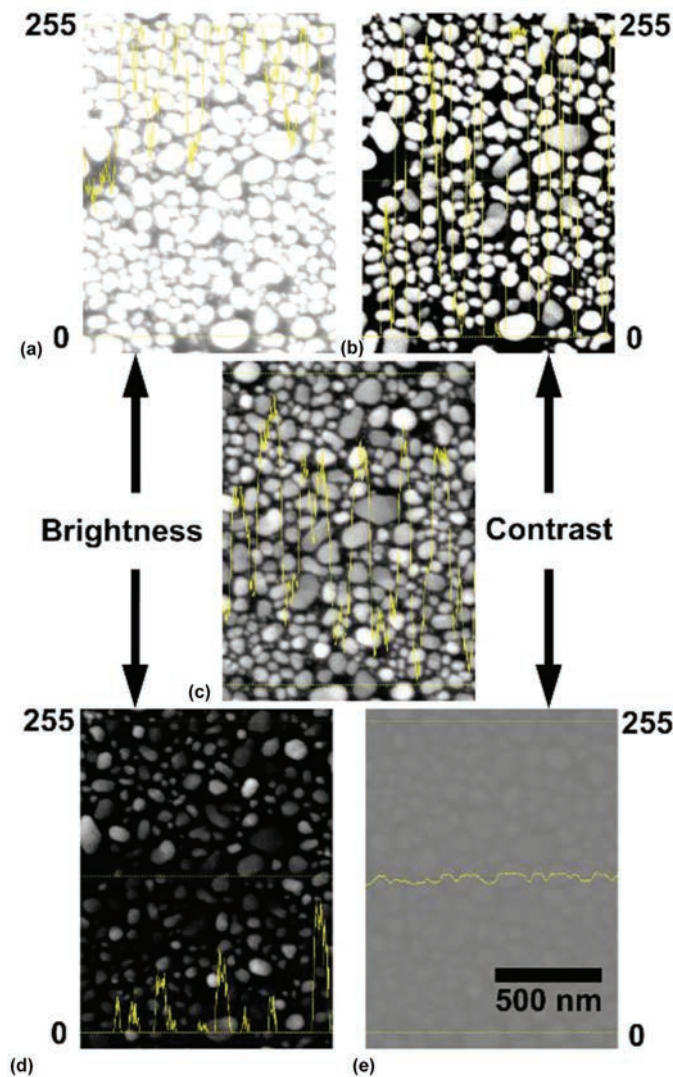


Fig. 11 Five scanning electron micrographs of gold nanoparticles recorded at various brightness and contrast settings, with superimposed waveform (yellow plot). (a) Excessive brightness leads to loss of information. (b) Excessive contrast results in saturation for both 255 and 0 grayscale values. (c) Optimized brightness and contrast settings result in all pixel intensities falling within the 0 to 255 range. (d) Too-low brightness produces a saturation where much of the pixel intensity falls below the 0 grayscale value. (e) Excessively low contrast setting produces an image where features become difficult to resolve

grayscale values without exceeding the top dotted line (255 grayscale value) or bottom dotted line (0 grayscale value). Also, the waveform exhibits seven individual peaks that correspond to seven individual gold nanoparticles spanned by the central horizontal line of pixels (central dotted line).

Increasing the brightness gain settings increases the grayscale values for all pixels. However, excessive brightness increase can lead to loss of information (Fig. 11a). If much of the waveform exceeds the 255 grayscale value, then numerous adjacent pixels are solid white and yield no contrast or useful information. This loss of information is termed saturation. Lowering brightness too far also produces a saturation, where much of the pixel intensity falls below the 0 grayscale value (Fig. 11d).

While brightness adjustments aim to position the waveform between the 255 and 0 grayscale values, contrast adjustments should aim to maximize the waveform amplitude while also avoid exceeding the 255 and 0 values. Figure 11(b) demonstrates when the contrast is too high. Saturation occurs for both 255 and 0 grayscale values. Reducing contrast decreases the waveform amplitude size. While this can ensure that saturation is avoided, an excessively low contrast setting produces an image where features become difficult to resolve (Fig. 11e).

Dwell Time

Dwell time, as mentioned previously in Fig. 7, is the amount of time the electron beam

spends on each point in the raster. Dwell times typically vary from milliseconds down to nanoseconds. Setting a short dwell time is advantageous for fast scan rates approaching “live” imaging of the specimen. Each frame may only take a fraction of a second to acquire, so images are rapidly updated. This is useful when navigating to different positions on the specimen, adjusting focus, or correcting astigmatism. Longer dwell times enable more signal collection for each pixel position, producing images with less noise, as illustrated in Fig. 12. Improving signal-to-noise (S/N) ratio helps to better define contrast and associated information regarding the specimen, such as feature width and surface topography. Using longer dwell times could mean a single frame might require a few seconds up to a few minutes to acquire. Slight drift of the beam and/or the specimen during such long acquisition times could produce a smeared image. Control software often provides drift correction combined with frame integration to mitigate this problem.

Digital images

Digital images acquired by SEM are typically stored in the tagged image file format. Scanning electron microscopes generally enable the user to define the number of pixels that make up the image and the range of possible grayscale values each pixel could be assigned. An image with more pixels provides more spatial information but at the expense of requiring longer time to acquire a single frame. Digital grayscale images can be recorded at 8 or 16 bits for 256 or 65,536 grayscale values, respectively. The human eye can resolve ~16 different shades of gray, which corresponds to ~16 units of grayscale intensity differences for 8-bit values, as shown in Table 2. Recording digital images in 24-bit format retains color associated with any graphics or annotations added to the SEM micrograph (data bar, measurements, and notes). The amount of memory required for any digital image file is a function of the total number of pixels acquired and the grayscale intensity range used. Table 2 provides example colors and bit values that are standard for digital images.

Advantages of the SEM

Two major advantages of the SEM over the optical microscope as a tool for examining surfaces are improvements in resolution and depth of field. Information on the determination of resolution and depth of field in the optical microscope is provided in the article “Light Microscopy” in *Metallography and Microstructures*, Volume 9, *Handbook*, ASM 2004. Because SEMs are also often compared with transmission electron microscopes (TEMs), this section also details various types of SEM samples and mounting strategies to highlight potential advantages over the TEM.

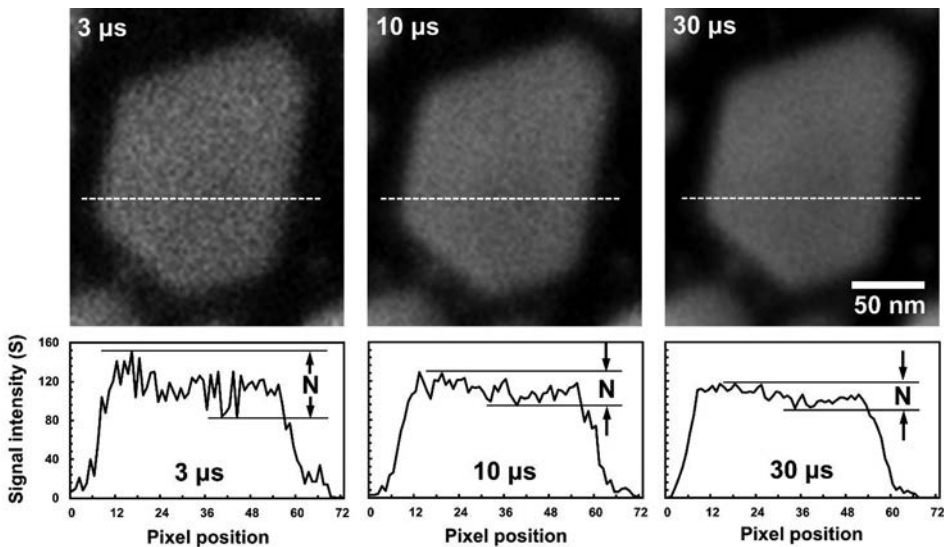


Fig. 12 Scanning electron micrographs of a single gold nanoparticle recorded at 3, 10, and 30 μ s dwell times. Longer dwell times enable more signal collection for each pixel position, producing images with less noise. Signal intensity plots correspond to the horizontal row of 72 pixels denoted by the dotted white line.

Table 2 Example colors and grayscales for 24-, 8-, and 16-bit values

Color	24-bit values			Grayscale	8-bit values	Grayscale	16-bit values
White	255	255	255		255		255 255
Gray	128	128	128		240		255 240
					224		255 224
Black	0	0	0		208		255 208
					192		255 192
Red	255	0	0		176		255 176
Green	0	255	0		160		255 160
Blue	0	0	255		144		255 144
					128		255 128
Yellow	255	255	0		112		255 112
Cyan	0	255	255		96		255 96
Magenta	255	0	255		80		255 80
Orange	255	192	0		64		255 64
Purple	112	48	160		48		255 48
Pink	255	153	204		32		255 32
					16		255 16
					0		255 0

Resolution

Resolution can be defined in terms of a point resolution and an image resolution. Point resolution is the crucial parameter that defines SEM performance and its ability to resolve features down to a minimum threshold size. Point resolution for the SEM is directly determined by spot size, which is the electron beam diameter at the sample surface plane, d_s . However, it should not be automatically assumed that the electron beam/probe size sets the point resolution. Point resolution is also influenced by the type of signal used for image formation, discussed later in this article. Additional

information on the resolution limits of the SEM can be found in Ref 13 and 14. Figure 13 illustrates the relationship between d_s and feature size for resolving topographical details of interest. Pearlite consists of alternating plates of Fe_3C in a matrix of α -iron. When etched using nital or picral, the Fe_3C plates stand in relief, as shown in Fig. 13(a). Because the Fe_3C plates are in relief, the SE yield from them is very high. Consider a scanning electron beam having a d_s much smaller than the Fe_3C spacing, S_α . As the beam scans from positions 1 to 5, the scanning electron signal intensity exhibits the sharp square wave form shown in Fig. 13(b), and the Fe_3C plates appear in sharp contrast on

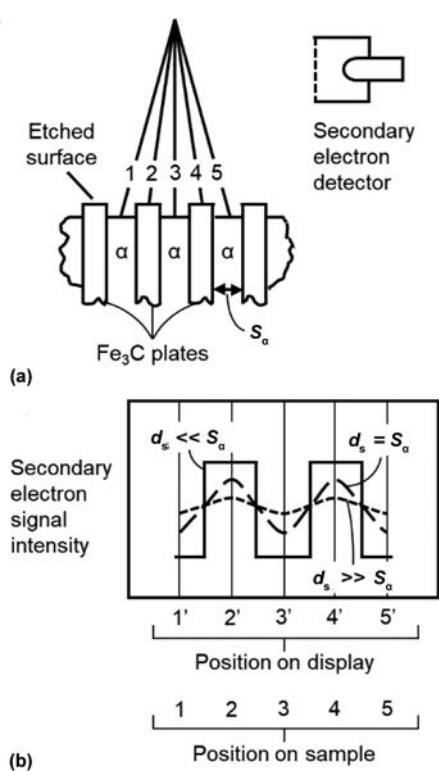


Fig. 13 (a) Line scan across an etched pearlite sample surface. (b) Effect of beam diameter, d_s , on secondary electron signal intensity. A beam with d_s much smaller than the lamella spacing, S_α , results in lamella plates appearing in sharp contrast on the digital display.

the digital display. If the beam diameter is increased such that $d_s = S_\alpha$, the signal would become more like a sine wave, and the edges of the Fe_3C plates would become very fuzzy on the digital display. Finally, for $d_s > S_\alpha$, the Fe_3C plates would no longer be distinguishable on the display. In general, to resolve a feature of size S_α , a beam diameter less than S_α is required.

A line scan across a feature produces signal intensity variations, ΔS , visible as various grayscales in the digital display (Fig. 10). A generally accepted rule for the ability of the eye to discern a feature is that $\Delta S > 5N$ (see Fig. 10 for an explanation of S , ΔS , and N). Based on this criterion, the signal current, i_s , required to see a feature that produces a signal jump of ΔS is (Ref 15):

$$i_s = i_B \epsilon > \frac{(4 \times 10^{-18} \text{ coulombs}) n_{\text{pixels}}}{\left(\frac{\Delta S}{S}\right)^2 t_f} \quad (\text{Eq 4})$$

where i_B is the beam current in the beam diameter, d_s ; ϵ is the detector efficiency in terms of signal collection per incident electron; n_{pixels} is the number of pixels in a digital image; and t_f is the time to acquire the image, that is, the frame time. As the spot size is made smaller, it contains less current. The current in the

beam spot is a function of the brightness of the electron gun, β ; the beam voltage, V ; and the aberrations of the electron lens.

Spherical aberration is generally considered to be the limiting factor for SEM resolution, and it is characterized by a constant, C_s , where the larger the value of C_s , the greater the aberration. For conditions of optimum aperture size selection, beam current varies with beam diameter on the sample (Ref 14):

$$d_s = \left[\frac{16i_B}{3\pi^2\beta} \right]^{3/8} C_s^{1/4} \quad (\text{Eq 5})$$

The value of d_s is larger than the d_3 value given by Eq 2 due to lens aberrations. Equations 4 and 5 illustrate the important factors in resolution limits with an SEM. Assuming a single megapixel (10^6) digital image, resolving a feature with $\Delta S/S$ greater than a certain minimum value requires a certain critical minimum beam current in picoamps, $(i_B)_c$:

$$(i_B)_c = \frac{4}{\varepsilon \left[\frac{\Delta S}{s(\min)} \right]^2 t_f} \quad (\text{Eq 6})$$

By increasing the collector efficiency, ε , and by using longer frame times, t_f , the value of $(i_B)_c$ can be reduced. Equation 5 shows that reductions of d_s are limited, because decreasing d_s decreases i_B , and eventually it will fall below $(i_B)_c$. For the crucial value of $(i_B)_c$, Eq 5 shows that smaller beam diameters are achieved by increasing β and decreasing the spherical aberration coefficient, C_s . Maximum resolution requires a minimum d_s , which requires maximum values of β , ε , and t_f and minimum C_s values. Field-emission sources have higher brightness than thermionic sources and thus are preferable for high-resolution imaging. In general, C_s decreases as the sample is moved closer below the objective lens; that is, as the WD decreases.

More advanced commercial SEMs provide specialized lens configurations to obtain ultra-high resolution (UHR). One type of lens is an immersion lens, where the sample is positioned inside a gap between the upper and lower parts of an objective lens pole piece. In either case, the lenses greatly reduce the WD and reduce C_s significantly, but they require the use of in-lens detectors. Immersion lens instruments provide improved resolution, and current UHR-SEMs have point resolution <0.5 nm.

Any point resolution value reported for a given SEM depends on many factors, including whether the electron source is thermionic versus a field-emission source, what type of signal is detected, and what lens configuration is used. Typical resolution values claimed by manufacturers for general types of SEMs are given in Table 3 and are compared with those of optical microscopy (OM). The SEM offers a distinct advantage over OM for high-resolution imaging.

Table 3 also lists the maximum useful magnification ranges; at magnifications above approximately twice these values, features become fuzzy and unresolvable.

Another way to compare SEM and OM resolution is to assess micrographs of fine pearlite, as shown in Fig. 14. The optical micrograph (Fig. 14a) of a pearlitic gray iron specimen was taken at the upper magnification limit of an optical microscope using optimum resolution conditions (Ref 16). Pearlite lamellar spacing of 1 to 2 μm can be defined, but finer spacing is unresolvable. Figures 14(b) and (c) show micrographs for a hypereutectoid steel acquired using an SEM at higher magnifications. The pearlite lamellae are much finer in the hypereutectoid steel. Nevertheless, the SEM can readily resolve the pearlite plate spacing (~ 200 nm) at a magnification 20 times higher than OM.

Image resolution is often mistakenly used in place of point resolution. Image resolution refers to the quality of the digital image itself in resolving fine-scale features. Image resolution is influenced by the digital image characteristics, such as contrast gain settings, grayscale range, and number of pixels used to resolve features. As such, image resolution pertains to the quality of the digital image instead of the actual point resolution, probe size, or performance of the SEM.

Depth of Field

At a distance below and above the focal plane, the beam diameter becomes large

enough to overlap adjacent pixels. Depth of field refers to the distance above and below the focal plane where features are still resolvable, and the image is still considered in focus. Calculating depth of field requires consideration of how the primary beam diameter broadens from a diameter at focus, d_s , to a diameter large enough to overlap an adjacent pixel. Therefore, depth of field depends on the magnification used as well as the beam convergence angle, α . A useful criterion is to presume a typical observer can discern image blur once two adjacent pixels completely overlap (Ref 17). Thus, depth of field (DOF) is given as:

$$\text{DOF}(\text{mm}) = \frac{2p}{\alpha \times M} \quad (\text{Eq 7})$$

where M is the magnification, α is the convergence angle of the beam striking the sample, and p is the physical pixel size in millimeters. For example, a standard 21.5 in., 1080p digital display has a p value of 0.248 mm. Table 4 presents calculated values of depth of field based on Eq 7 for beam convergence angles, α , of 2 and 30 milliradians. At higher magnifications, the pixel size approaches the focused beam diameter, and features quickly become blurry and out of focus when displaced even a small distance from the focal plane. Therefore, higher magnification leads to a smaller depth of field.

Table 4 also indicates that reducing beam convergence angle, α , increases depth of focus. The value of α is determined by the

Table 3 Typical resolution and magnification ranges for general types of scanning electron microscopes and for an optical microscope

Microscope	Minimum resolution range, nm	Maximum useful magnification
General-purpose scanning electron microscope	5–10	20,000–50,000×
General-purpose field-emission scanning electron microscope	1.0–2.5	250,000–400,000×
Ultrahigh-resolution field-emission scanning electron microscope	0.3–1.0	400,000–1,000,000×
Optical microscope	100–200	1,000–2,000×

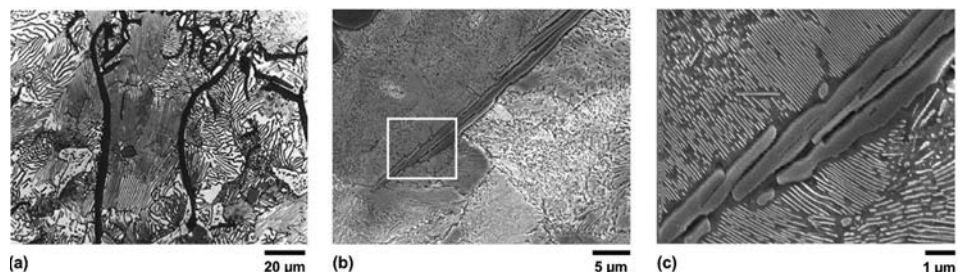


Fig. 14 (a) Optical micrograph of pearlitic gray iron taken using a high-quality optical microscope with an oil immersion lens and green filter; 4% picral etch. Fine pearlite lamellar spacing is unresolvable. Source: Ref 16. (b) Scanning electron micrograph of pearlitic hypereutectoid steel taken using a conventional scanning electron microscope, secondary electron detection, and 15 keV beam; 4% nital etch. Courtesy of M. Hecht, Carnegie Mellon University. (c) The center region denoted by white rectangle in image (b) with magnification increased by a factor of 4. Scanning electron microscopy resolves spacing (~ 200 nm) at a magnification 20 times higher than optical microscopy.

Table 4 Calculated values for depth of field based on Eq 7 for a digital scanning electron micrograph

Magnification	Image width, μm	Depth of field, μm	
		$\alpha = 2 \text{ mrad}$	$\alpha = 30 \text{ mrad}$
10×	47,600	24,800	1,653
50×	9,520	4,960	331
100×	4,760	2,480	165
500×	952	496	33
1,000×	476	248	17
10,000×	48	25	1.7
100,000×	4.8	2.5	0.17

Note: Micrograph encompasses entire standard 21.5 in., 1080p digital display, with a 19 in. wide horizontal display composed of 1920 pixels.

WD and the diameter of the objective aperture, d_a :

$$\alpha \approx \frac{d_a/2}{WD} \tag{Eq 8}$$

Figure 15 illustrates the effect of increased WD and reduced objective aperture size in extending depth of focus. From Eq 7 and 8, for a given magnification, the user can increase the spatial region that is in effective focus for a highly tilted or irregular surface using a longer WD and/or smaller d_a .

Depth of field of an SEM is very good compared with an OM. The difference in the two microscopes is illustrated in Fig. 16, which compares images of 1 to 10 μm -sized tin spheres obtained by OM using a 50 \times objective lens and by SEM. The OM image is focused to the smallest ($\sim 1 \mu\text{m}$) spheres and exhibits significant blurring for the larger-sized spheres. However, spheres of all sizes are in focus in the SEM image. In general, the SEM depth of field exceeds that of the OM by a factor of approximately 300. Therefore, SEMs have found widespread use for examination of fracture surfaces and deeply etched samples.

The SEM is generally inferior to the OM for routine examination of samples prepared using standard metallographic techniques when examined at magnifications less than 300 to 400 \times . Standard metallographic techniques can produce surface relief (especially after etching) suitable for contrast in the SEM at these lower magnification ranges. However, color variations detectable by OM can provide subtle and useful material information not obtainable by SEM. Due to the relatively limited contrast of the SEM on metallographically polished and etched samples at low magnifications, it is generally useful to use microhardness indentations as fiducial marks. Placing such marks near a point examined in the OM facilitates locating that same point in the SEM for examination at higher magnification.

Samples

Scanning electron microscopy is amenable to a broad array of samples, but there are some

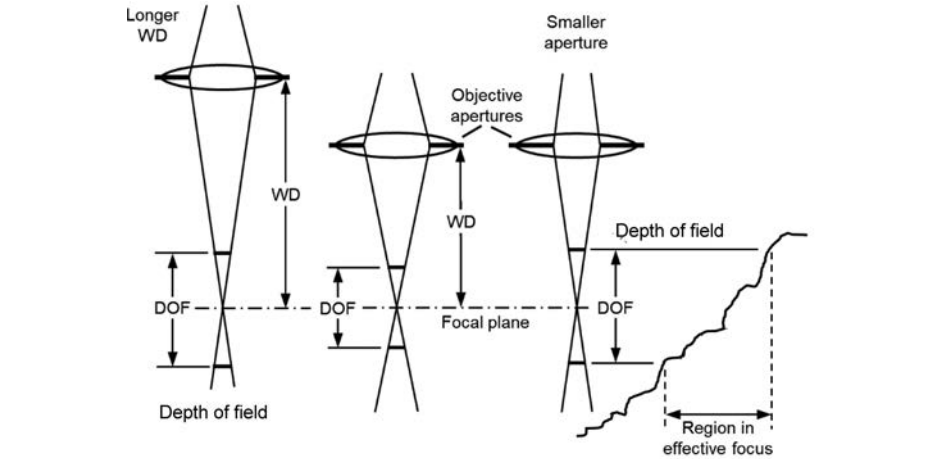


Fig. 15 Effect of (left) longer working distance (WD) and (right) smaller objective aperture size on depth of field (DOF) and associated size of region in effective focus

limitations. Conventionally, samples should be electrically grounded to the holder and SEM stage. As such, solid specimens that are electrically conductive require no sample preparation. Nonconductive solids can be imaged if coated with a conductive metallic or graphitic carbon thin film that grounds the imaged surface. If there are concerns with surface coatings, uncoated nonconductive solids can be imaged using low-electron-beam energy (Ref 18) or using a variable-pressure or environmental SEM (Ref 15), which can remove surface charge in the absence of electrical grounding. Another approach is the use of flood guns, an add-on capability for SEMs. Flood guns direct charged particles at the sample surface, thereby removing surface charge for nonconductive specimens. Wet and fixed biological specimens can also be imaged using a variable-pressure or environmental SEM in this manner. New SEM stages have been developed to allow imaging of liquid specimens (Ref 19).

Because specimens are placed under vacuum inside the SEM, samples should have a low vapor pressure ($\leq 0.01 \text{ Pa}$, or 10^{-3} torr) and be free of any high-vapor-pressure liquids, such as water, organic cleaning solutions, and remnant oil-based films (Ref 20). Unwanted carbon buildup at the imaged region often occurs. This buildup occurs due to electron-beam-stimulated surface reactions with hydrocarbon contamination originally trapped within sample surface pores and surface cracks. Therefore, it is important to dry the samples thoroughly, to use gloves to avoid skin contact with the sample and holder, and to avoid introducing plastic mounting materials into the specimen chamber, which can have high vapor pressures and trap hydrocarbon films at the mount-sample interface. Add-on accessories to the SEM chamber can generate a plasma to help capture and remove hydrocarbon contamination during SEM analysis (Ref 21).

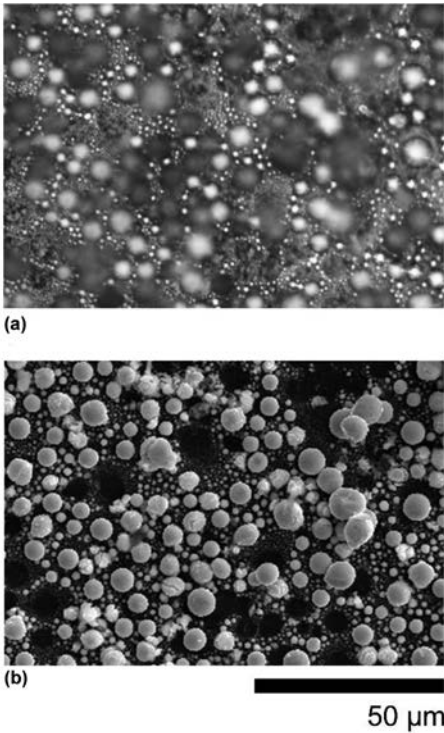


Fig. 16 Micrographs of tin spheres recorded by (a) optical microscope (OM) and (b) scanning electron microscope (SEM). Focusing the OM on the smallest spheres results in blurring of larger spheres, while spheres of all sizes are in focus with the SEM due to better depth of field.

The SEM offers an important advantage over the TEM with regard to sample size and preparation issues. Samples as large as 20 cm ($\sim 8 \text{ in.}$) can be placed in the SEM, although regions on such samples that can be examined without repositioning are limited to $\sim 5 \text{ cm}$ (2 in.). Nevertheless, this is an exceptional advantage over the TEM, where samples can

only be as large as 3 mm (0.125 in.) and areas for analysis must be transparent to the electron beam. Electron transparency requires that TEM specimens are thinned down to <200 nm at any region of interest. Because the SEM is primarily a surface analysis technique, specimen thinning is not necessary. However, thinned specimens amenable for TEM analysis can also be mounted, imaged, and analyzed in the SEM using transmission-mode detectors described previously (Fig. 8). Transmission-mode SEM (Ref 9) offers a cost advantage for those interested in nanoscale imaging using Z-contrast and diffraction-contrast modes instead of using the TEM. Also, the use of transmission Kikuchi diffraction (Ref 22) offers an exceptional capacity for nanoscale crystallographic orientation and phase analysis in the SEM instead of using precession-diffraction techniques in the TEM (Ref 23).

The SEM sample preparation varies depending on the material to be analyzed and the type of SEM analysis to be performed. Consideration must be given to the electrical conductivity of the specimen and if a conductive coating should be used. For bulk samples, consideration should also be given regarding the desired configuration of the surface in relation to the beam and detectors, and the desired state of that surface (as-is, polished, etched). Samples are conventionally attached to a metal support, such as a brass cylinder or aluminum pin stub. These supports are often designed for an SEM manufacturer. Pin stubs may be flat or could provide a particular pretilt angle (45°, 90°). Some supports hold the samples in place using metal pins or screws. Otherwise, bulk materials are conventionally affixed to flat pin stubs using a vacuum-compatible, conductive adhesive, such as graphitic carbon or copper adhesive tape. Carbon (graphitic flakes) paste and colloidal silver paint are also common adhesives, but they must be cured for some time in air or in an oven (~80 °C, or 175 °F). Carbon tape and conductive paints can later be removed using solvents such as acetone. The support stub has a pin that fits inside the SEM stage. The stub is held in place either by a spring-mounted connection or by tightening a set-screw. Good mechanical and electrical contact between the support stub and the SEM stage surface ensures minimal vibration and charging effects during SEM analysis. For more details, an excellent reference on SEM sample preparation can be found in Ref 24.

Electron Beam Interactions with Samples

An image of the scanned surface region can be acquired using any signal generated by the electron beam. In a typical SEM, it is possible to use as many as three or more different signals to generate complimentary images detailing the topography and composition of a

sample. To understand the potential utility of scanning electron microscopy, it is necessary to understand some elementary ideas regarding the nature of signal generation when high-energy electrons strike a sample surface.

Types of Signals

When an electron beam strikes a solid surface, a variety of signals can be generated, as illustrated in Fig. 17. **Backscattered electrons (BEs) are those electrons from the primary electron beam that have scattered back out of the specimen surface.** Deceleration of the high-energy electron beam by the specimen produces x-rays and other electron signals. Electrons bound to atoms within the specimen can be energized by the primary beam. **Secondary electrons (SEs) are electrons initially within the specimen that have absorbed sufficient energy from the primary electron beam to escape the specimen surface.** Electron transitions within an atom that result from the interactions associated with SE production will also produce x-rays of specific energies characteristic to the elemental identity of that atom. The electron energy transitions resulting from the primary beam can also produce Auger electrons; semiconductors also produce light through a process called cathodoluminescence. Electrons from the primary beam that do not escape as BEs are absorbed electrons, which can produce an electric current. If the

specimen is sufficiently thin, some electrons from the primary beam could pass through the sample to become transmitted electrons.

Interaction Volume and Escape Depth

Most of the signals previously mentioned emanate from different depths within the specimen. Figure 18 depicts a typical interaction volume where the primary electron beam produces various signals within the specimen surface. As high-energy electrons penetrate the surface, they undergo elastic and inelastic collisions, which lead to the various signals mentioned previously. The collisions scatter the primary beam electrons mostly in forward directions but also laterally within the sample. This gives rise to the characteristic “teardrop” shape of the interaction volume in Fig. 18. Many signal types are generated throughout the entire interaction volume. However, each signal type varies considerably in its ability to escape the specimen surface. The escape depth is the extent within the specimen surface that a signal can exit the sample and be detected.

Electron signal escape depths are a direct function of the type and energy as well as the chemical composition of the sample. Electromagnetic radiation, such as x-rays and visible light, travels through solids much easier than electrons. Therefore, x-rays can be detected even when generated from the bottom of the

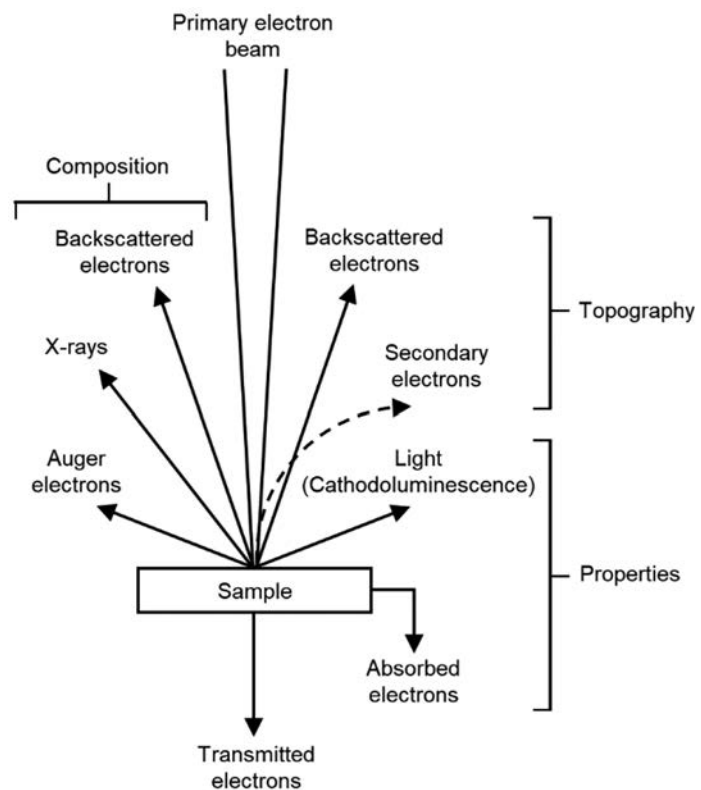


Fig. 17 Various signals generated when an electron beam interacts with a specimen

interaction volume, where electrons from the primary beam have penetrated deep into the specimen (Fig. 1). Therefore, x-rays have an associated information depth. Secondary electrons are also generated at these depths but are readsorbed by the specimen well before escaping the surface. Only SEs generated within ~5 to 50 nm of the surface can escape and reach a SE detector placed above the sample. Metals absorb SEs more readily than insulators, so SE escape depths are generally a factor of 10 smaller for metals than insulators. Backscattered electrons have higher energy than SEs and thus can escape from greater depths than SEs. Escape depths for BEs and information depth for x-rays change based on the primary beam energy, but SE escape depths remain constant.

Depth of penetration by the primary electron beam is a function of electron beam energy and the chemical composition of the specimen. A useful expression for determining the maximum range, R (nm), of primary electron beam penetration into a specimen is the Kanaya-Okayama formula (Ref 25):

$$R = \frac{27.6AE_0^{(5/3)}}{\rho Z^{(8/9)}} \quad (\text{Eq 9})$$

where E_0 is the primary electron beam energy (keV), A is the atomic weight (g/mol), ρ is the density (g/cm³), and Z is the atomic number of the specimen. From this expression, the depth of the beam-sample interaction volume increases with higher SEM acceleration voltage. For example, the calculated R value for iron using Eq 9 is 0.51, 1.6, and 3.2 μm at 10, 20, and 30 keV primary beam energy, respectively. Figure 19 presents Monte Carlo simulations, generated using CASINO v3.3 (Ref 26), of 100 primary beam electron trajectories into iron at different beam energies.

Monte Carlo simulations help to visualize the degree of depth penetration and lateral travel the primary electrons undergo inside the specimen.

It is crucial to consider this interaction volume when evaluating the SEM as a probe into the chemical composition and structure of a specimen. Spot size, d_s , is an important parameter regarding the physical size of the electron beam diameter as it enters the specimen. However, the lateral size and sampling depth of the actual electron probe is influenced by the interaction volume and specific signal to be detected. Figure 18 shows that the same probe produces x-rays from a much larger volume and wider lateral probe size, x_x , of the sample than BEs and SEs, corresponding to x_B and x_S , respectively. Therefore, the actual point resolution of the SEM is a direct function of acceleration voltage and detected signal, in addition to spot size. This raises important concerns regarding how to interpret images generated simultaneously inside an SEM by one signal

type versus another; discrepancies between an x-ray map and SE/BE image obtained in the SEM can be readily attributed to different signal escape information depths within the interaction volume. This point is discussed later in the section "Sampling Volume for Various Signals" in this article.

Electrons

Electron signal emitted by the sample can be partitioned into three types based on energy distribution, as shown in Fig. 20: secondary, backscattered, and Auger. Secondary electrons are <50 eV. Backscattered electrons range from energies equal to the primary beam energy, E_0 , down to ~50 eV. Auger electrons can exceed the number of detected BEs at specific energies characteristic of the elements within the specimen. Auger electron energies fall in the 50 to 2000 eV range. Energies of SEs and Auger electrons are fixed, but BEs

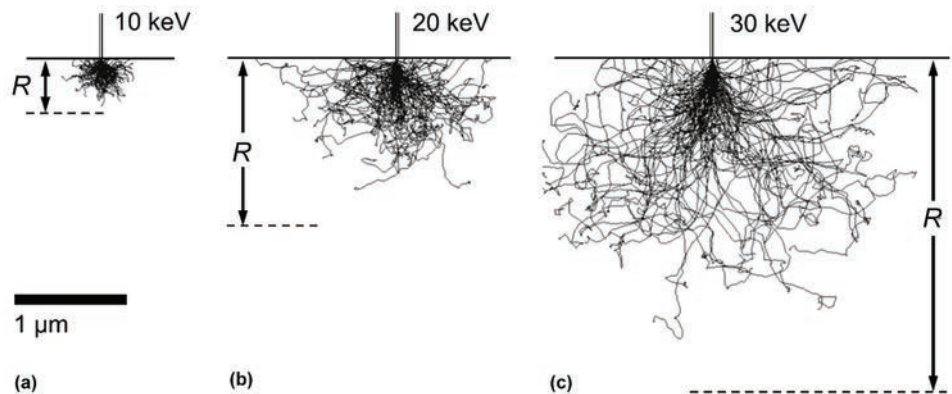


Fig. 19 Monte Carlo simulations of 100 primary beam electron trajectories in iron for (a) 10, (b) 20, and (c) 30 keV beam energies. Monte Carlo simulations help to visualize the degree of depth penetration, R , and lateral travel the primary electrons undergo inside the specimen. Reprinted/adapted from Ref 27 with permission of Springer Nature

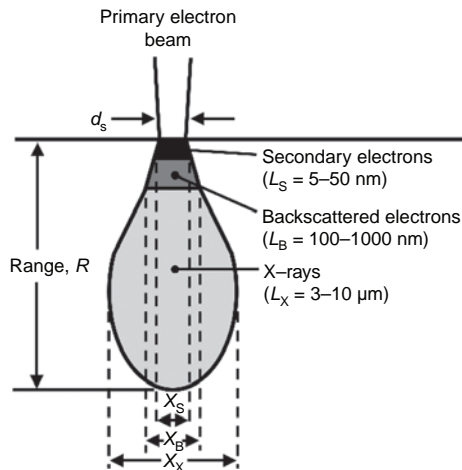


Fig. 18 Illustration of interaction volume of depth, R , with corresponding escape depths and information depth, L , and lateral probe size, x , for different signal types

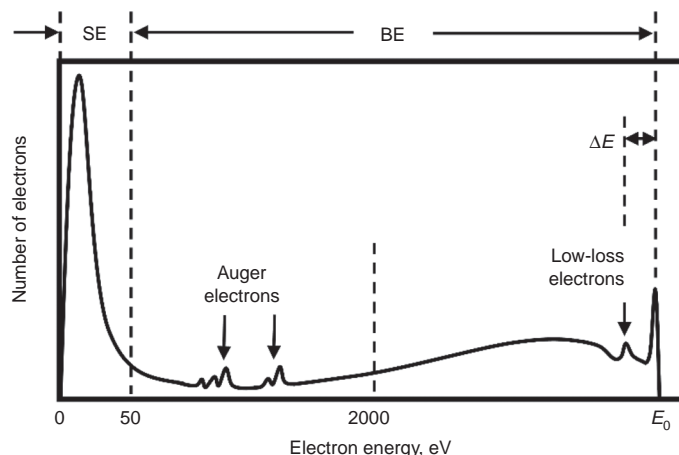


Fig. 20 Energy distribution of emitted electrons produced by a primary electron beam energy, E_0 . SE, secondary electrons; BE, backscattered electrons

shift their energy values as the primary beam energy changes. The BEs and SEs can be further partitioned into three types, so all possible electron signals include:

- Backscattered electrons
 - a. Type 1: elastically scattered
 - b. Type 2: inelastically scattered
 - c. Type 3: plasmon and interband transition low loss
- Secondary electrons
 - a. Type 1: inside primary beam
 - b. Type 2: outside primary beam
 - c. Type 3: other nonspecimen surfaces
- Auger electrons

Backscattered Electrons

When a primary beam electron strikes the sample, it can take one of many possible pathways through the sample. A number of these trajectories terminate inside the sample, particularly those trajectories that penetrate deep into the bulk, but some trajectories curve their way back to the surface (Fig. 19). Primary electrons that escape the surface by such trajectories are termed backscattered, and there are three general processes by which this can occur. Figure 21 illustrates primary electron (PE) trajectories into a sample surface. The first PE trajectory, (A), illustrates a PE that, upon entry into the specimen, immediately scatters elastically out of the specimen and emerges with the same energy as the beam energy, E_0 ; this type of BE is called BE(1). A second PE trajectory, (B), propagates a longer distance within the specimen surface before escaping, losing some energy through inelastic collisions along the way. This type of BE is called BE(2) and can have any energy value below E_0 . The PE trajectory (C) illustrates a PE that has penetrated so deep into the specimen that it is unable to escape and becomes absorbed. The BE(3) is a primary beam electron scattered by interactions that produce either a plasmon oscillation of the electrons in the sample material or a transition of specimen electrons between different energy bands.

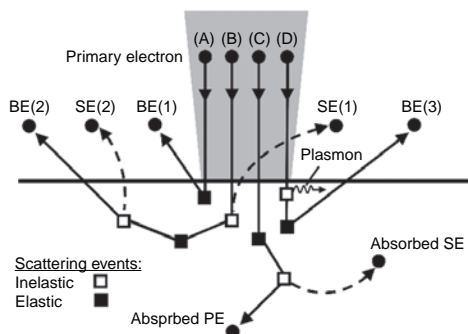


Fig. 21 Illustration of various types of backscattered electrons (BE) and secondary electrons (SE) generated by primary electrons (PE)

The PE trajectory (D) illustrates a PE that produces a plasmon and immediately escapes the specimen without losing additional energy. The energy to excite plasmons or interband excitations have fixed values denoted as ΔE in Fig. 20; therefore, BEs that emerge after one of these interactions have an energy lower than E_0 by the amount ΔE . Two types of plasmon oscillations occur in which surface electrons or bulk electron oscillations are excited. The interband transitions also require a specific ΔE . The ΔE s for all these small peaks differ from element to element, and sometimes they differ according to whether the element is present as a pure element or an oxide, hydride, nitride, and so on. The BE (3)s are often termed low-loss electrons (LLEs) because they lose a small but specific amount of energy. The LLE energy is readily measured in the TEM through electron energy loss spectrometers (EELS) to provide a variety of useful information on chemical identity, chemical bonding, and plasmonics (Ref 28). However, SEMs conventionally use BE detectors that measure the number of collected BEs and not the energy of individual BEs. The incorporation of EELS in the SEM is under development.

The BE yield is quantified by a coefficient, η , that relates the ratio of number of BEs produced per number of primary beam electrons. Two factors that influence η are the atomic number of the specimen, Z , and the tilt angle, θ , of the primary beam with respect to the sample surface normal direction. Therefore, detected variations in η give rise to BE image contrast sensitive to specimen composition and/or surface topography. Figure 22 plots calculated BE yields, η , as a function of θ for different elements. For a 0° tilt angle, values of η range from 0.05 to 0.55 from low to high

atomic number. At high sample tilt angles, η values increase to a range of 0.6 to 0.8.

Figure 23 illustrates why BE yield increases with both higher atomic number and higher tilt angle. As shown in Fig. 23 (a), for a given primary beam energy, the penetration range decreases with higher atomic number. Therefore, a greater portion of the interaction volume is closer to the surface and within the BE escape depth, L_{BE} , which leads to a higher probability for primary beam electrons to escape the surface. A similar effect occurs with increasing tilt angle, illustrated in Fig. 23(d, e). The interaction volume is brought closer to the surface, enhancing the probability for primary beam electrons to escape the surface as BEs.

The angular distribution of BEs is important to consider. Figure 23(b) depicts the angular distribution of BE yield as a function of take-off angle, Φ , for a nontilted specimen ($\theta = 0^\circ$). The shaded circular area represents the total number of BEs generated, so the size of the circle can be related to η (Ref 29). The angular distribution is a sine function of Φ as defined here, so the number of BEs generated can be related to a maximum value when $\Phi = 90^\circ$. For example, the number of BEs emitted along trajectory 1 in Fig. 23(b) is $\eta_n \sin(\Phi_1)$, where η_n is the fraction of total BE yield, η , emanating parallel to the sample normal direction, \mathbf{n} . As the take-off angle decreases, the number of BEs emitted at that trajectory decreases. Therefore, vector 1 is a larger value than vector 2 in Fig. 23(b). This demonstrates why BE detectors are conventionally positioned directly above the sample. Preferential collection of high-take-off-angle trajectories maximizes BE collection for nontilted samples.

As the sample is tilted, the angular distribution becomes an ellipse, with the maximum BE yield located at an angle, $\Phi = 90^\circ - \theta$

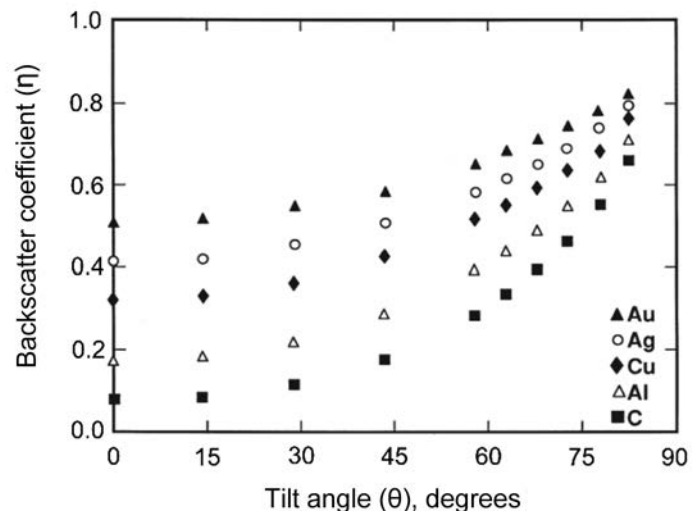


Fig. 22 Backscattered electron yield as a function of tilt angle, θ , calculated for different elements using Monte Carlo simulations. Source: Ref 27

(Ref 29). Thus, for a sample tilt of 60° , the take-off angle with the highest BE emission is $\Phi = 30^\circ$, as illustrated by trajectory 4 in Fig. 23(c). Note that Φ_4 is similar in magnitude to Φ_2 , but the BE yield is substantially higher for Φ_4 due to the 60° sample tilt. As such, angles Φ_3 and Φ_1 are also similar in magnitude, but the corresponding BE yield is much lower for Φ_3 . Therefore, a BE detector positioned at the electron source collects a very small number of BEs from a highly inclined surface. This effect gives rise to topographic contrast due to BE signal-collection variations.

Lower-atomic-number elements show a more dramatic increase in BE yield as a function of sample tilt angle. It is instructive to consider values of η for copper and aluminum in relation to Fig. 22 and 23. According to Fig. 22, η_{Cu} is ~ 0.31 and η_{Al} is ~ 0.18 at $\theta = 0^\circ$. The differences in η are reflected in the areas of the shaded circles depicting angular BE distribution in Fig. 23(a) for the high-Z (copper = 29) and low-Z (aluminum = 13) cases. According to Fig. 22, η_{Al} increases to ~ 0.35 at a sample tilt angle of $\theta = 60^\circ$. This corresponds to the depicted shaded ellipse of angular BE emission, η_{LZ} , in Fig. 23(e), which

has an area comparable to the η_{HZ} shaded circle in Fig. 23(a). It should be noted that as a larger portion of the interaction volume reaches the BE escape depth, as shown in Fig. 23(e), the spatial region of BE emission increases. This effect makes the point resolution worse when BE imaging highly tilted samples. Note that the take-off angle and the symbol Φ are defined differently in this article compared with Ref 27 and 29.

Secondary Electrons

Secondary electrons are electrons that originally existed in the specimen and have been energized by the primary beam with enough excess kinetic energy (< 50 eV) to escape the surface. Secondary electrons are predominantly in the 5 to 10 eV range (Fig. 20). Because of their lower energy, SE escape depths are 1% of BE signal depths for 10 to 30 keV incident beam energies (Ref 13). Secondary electron escape depth is also independent of the primary beam energy. Image resolution is generally superior when detecting more localized SEs versus more spatially extensive BEs.

Like BEs, SEs are distinguished by three types, but the distinction is determined based on the proximity of their generation in relation to the primary beam position rather than by energy. Figure 24 shows the main sources of SEs using an etched pearlite sample as an example. Type 1 SEs are generated within the area of the primary beam, while type 2 SEs emanate from the surrounding area. Additional type 2 SEs are generated by primary electrons that emerge through the protruding cementite phase and strike the surrounding sample surfaces, such as the etched ferrite. Type 3 SEs are generated when BEs strike surfaces elsewhere in the SEM chamber, such as the bottom plate of the objective lens. Thus, SE(1)s and SE(2)s contribute signal from the sample, while SE(3)s contribute noise and are undesirable.

Even for a flat specimen, the effect of SE (2) signal on the point resolution can be significant. Figure 25 illustrates the spatial distribution of SE signal in relation to the primary beam spot size, d_s , at the specimen surface. As primary beam electrons propagate into the specimen, the lateral spread of primary electrons within the interaction

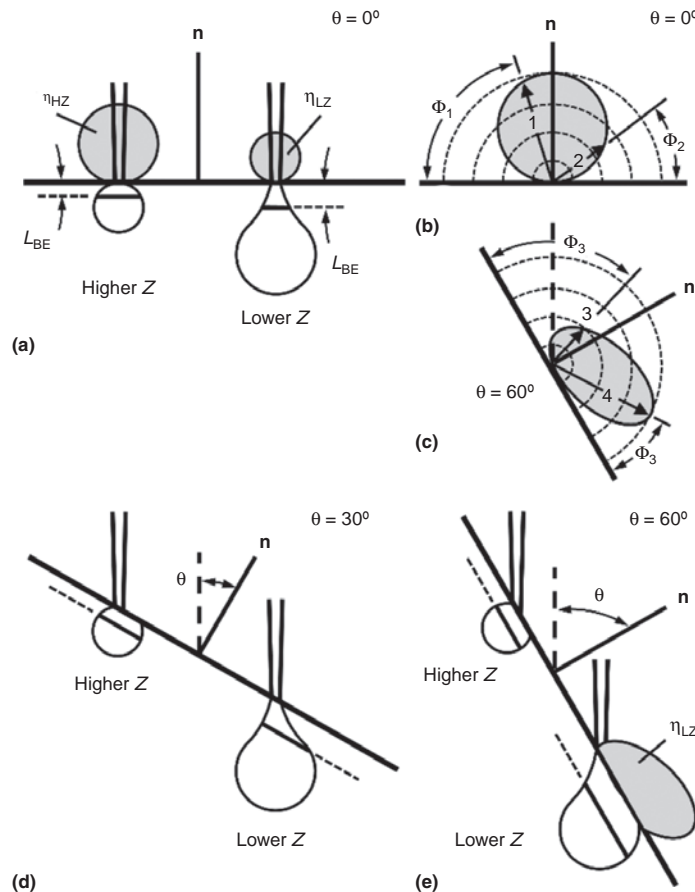


Fig. 23 (a) Illustration of primary beam interaction with 0° sample tilt (θ) for higher and lower atomic number (Z) and the resulting interaction volumes, backscattered electron (BE) escape depths (L_{BE}) and BE yields (η). Angular distribution of BEs as a function of take-off angle (Φ) for (b) 0° and (c) 60° sample tilt. Illustration of primary beam interaction with (d) 30° and (e) 60° sample tilt for higher and lower Z and resulting interaction volumes

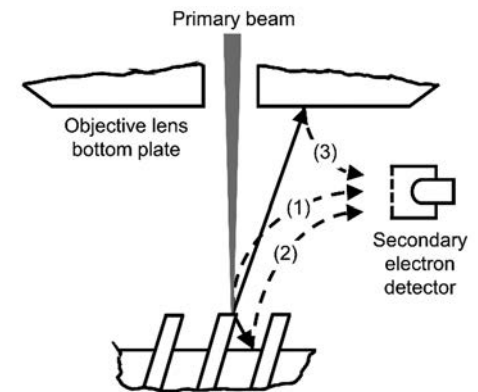


Fig. 24 Three types of secondary electrons defined by proximity to the primary beam

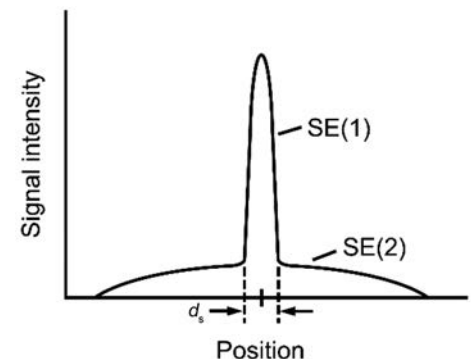


Fig. 25 Illustration of secondary electron (SE) spatial distribution in relation to primary beam diameter at specimen surface, d_s , for both SE(1) and SE(2) signals

volume produces SE signal outside the spot size diameter.

Secondary electron yield is quantified by a coefficient, δ , which relates the ratio of number of SEs produced per number of primary beam electrons. Similar to η , δ is influenced by the tilt angle, θ , of the primary beam with respect to the sample surface normal. Unlike η , δ can change significantly depending on the primary beam energy; SE yield increases substantially below 10 keV, because a significant portion of the interaction volume is brought within the SE escape depth, ~ 5 nm for metals and ~ 50 nm for insulators (Ref 27). The escape depth is larger for insulators, because there are fewer free electrons that can interact and absorb the <50 eV SEs as they propagate to the free surface. Chemical composition has very little effect on δ , so SE imaging is generally used for topographic contrast and not compositional contrast.

Auger Electrons

Auger electrons are generated as a result of incoming electrons knocking out intershell electrons (K, L, and M, depending on atomic number) from atoms near the surface. The knock-out events occur within the interaction volume (Fig. 18). After a K electron is knocked out, the surface atom emits either a characteristic x-ray or an Auger electron, as illustrated in Fig. 26. The probability for Auger emission exceeds that for x-ray emission at low atomic number. This is one of the reasons why Auger analysis has some

advantages for light-element analysis. As with the characteristic x-ray emission, the energy of the Auger electron is different for each element; therefore, analysis of Auger energies yields information on chemical identity. In addition, as with LLEs, Auger energy levels sometimes shift when an atom becomes oxidized, nitrated, and so on; therefore, information on the chemical state of the surface atoms may sometimes be obtained from Auger analysis.

A highly specialized SEM-type instrument operates at chamber pressure levels in the 10^{-7} Pa (7.5×10^{-9} torr) range to detect and analyze these low-energy Auger electrons. Scanning Auger electron spectroscopy (AES) requires cleaning surfaces by ion sputtering inside the chamber or by fracturing the sample in the chamber and examining the fractured surface. Auger electrons are collected from sample depths of 0.5 to 3 nm below the surface, depending on their energy. Auger electron energies are relatively low, and only those electrons near the sample surface can escape without suffering additional energy loss. Therefore, the Auger signal is very surface sensitive. This is particularly important when considering metal samples, which are typically covered with a thin oxide layer. The energy-loss electrons can be used as a signal in the AES instrument; the depth of its sample volume is a function of the beam energy contrary to the Auger signal. By using beam energies from 70 to 100 eV, surface sensitivities of less than half that of the Auger signal can be achieved, that is, down to 0.25 nm, or approximately one monolayer. More details on AES

can be found in the article “Auger Electron Spectroscopy” in this Volume.

X-Rays

X-rays are emitted by a specimen under high-energy electron bombardment. Bremsstrahlung x-rays are “braking x-rays” produced as the primary beam electrons are decelerated by the specimen. These x-rays are a continuum in energy distribution and form a background signal in x-ray spectroscopy. Characteristic x-rays are another type of x-ray produced by the primary beam and in higher numbers than bremsstrahlung x-rays, but only at specific energy values. Both x-ray types are illustrated in Fig. 27.

Similar to Auger electrons, characteristic x-rays are generated as a result of incoming electrons knocking out intershell electrons (K, L, and M, depending on atomic number) for atoms within the specimen. After an intershell electron is knocked out, a higher-energy electron from an outershell moves to replace that electron. This transition requires the emission of a photon that corresponds to the difference in outershell and innershell energy. Every element has specific energy values, ranging from hundreds to tens of thousands of electron volts, for its different electron shells. Therefore, the emitted photon is an x-ray with energy characteristic of the element. Figure 27 depicts three characteristic x-rays emitted by iron: $K_{\alpha} = 6.4$ eV, $K_{\beta} = 7.1$ eV, and $L_{\alpha} = 0.7$ eV. The α and β x-rays correspond to single- and two-level energy shell transitions, respectively. Thus, K_{α} is a single-level transition to the K-shell,

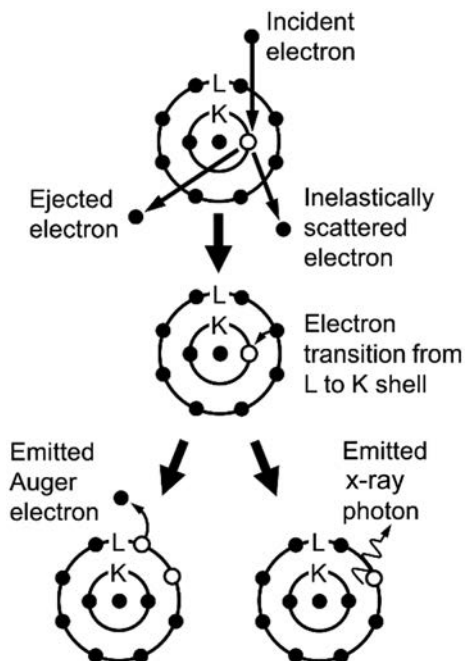


Fig. 26 Generation of Auger electron and x-ray photon by inner shell ionization of an atom and subsequent electron transitions

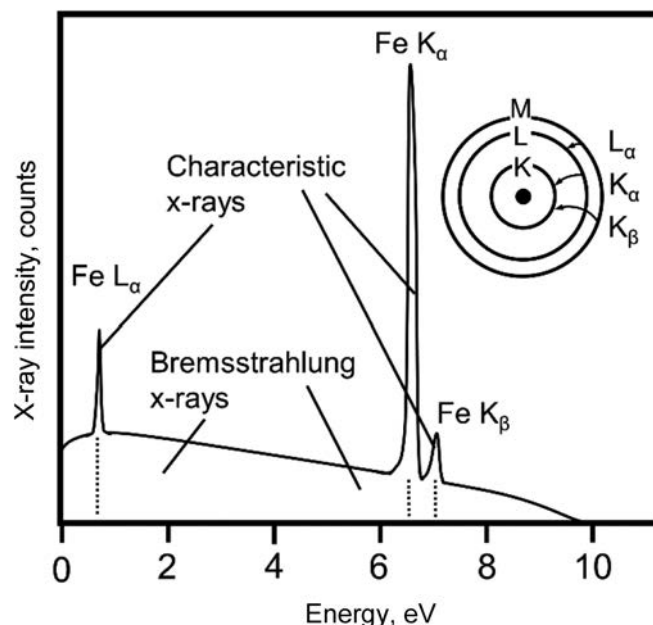


Fig. 27 Illustration of Bremsstrahlung x-rays and characteristic x-rays produced by a pure iron specimen. Energy transitions between M, L, and K shells are diagrammed for different characteristic x-rays.

L_{α} is a single-level transition to the L-shell, and K_{β} is a two-level transition to the K-shell. Note that the sum of the energies for the iron K_{α} and L_{α} peaks equals the energy of the K_{β} . Each element has specific characteristic x-ray energies that can be used to identify elements and quantify chemical composition inside the SEM. The larger the atomic number, Z , the higher the x-ray energies will be and the more transitions are possible to produce various characteristic x-rays.

The addition of an x-ray detector enables determination of the energy of emitted characteristic x-rays. Because each element in the periodic table has a different set of characteristic energies, the x-ray analyzer enables SEM determination and quantification of the elements present in the sample, from point to point on the sample surface. After obtaining a scanned image of the surface with the SE or BE detector, the user can position the electron probe to a specific pixel position on the static image. The scan coils deflect the probe to the user-defined position, such as a particle or region of interest. An x-ray spectrum can be collected from that point. Additionally, the user can define multiple analysis points, often equidistant, as defined by a line, rectangle, or other arbitrary shape. A single x-ray spectrum can be integrated from all points, or individual x-ray spectra can be recorded for each individual sample position. Furthermore, based on elements of interest, the measured intensity of specific x-ray energies can be plotted as a function of position to produce elemental distribution maps. A more detailed discussion of x-ray analysis can be found in the article “Electron Probe X-Ray Microanalysis” in this Volume.

Two approaches for x-ray analysis in the SEM are wavelength-dispersive spectrometers (WDSs) and energy-dispersive spectrometers (EDSs). Most SEMs with x-ray analysis capabilities are equipped with EDS detectors. X-ray detectors, such as lithium-doped silicon detectors or silicon-drift detectors, absorb x-rays, one at a time, and convert the x-ray energy to electron-hole pairs. The resultant charge is measured, stored as a single count assigned on the basis of measured energy, and the process is repeated for the next x-ray. The result is an x-ray spectrum plotted as number of x-rays, or counts, as a function of energy.

The EDS detectors detect elements with atomic number, Z , above boron ($Z = 5$) with 0.1 to 1.0 at.% sensitivity; more specialized “windowless” detectors are required to detect beryllium and lithium, while hydrogen and helium produce no characteristic x-rays and thus are undetectable. The WDS method also enables detection of all elements with $Z = 5$ and above, but with improved sensitivity (analysis down to approximately 0.01%), enabling superior quantitative analysis and resolving x-ray peaks that may overlap in EDS-produced spectra. However, WDS detectors are large,

slow, and not compatible with commercial TEMs. Specialized SEMs can be designed to accommodate multiple WDS detectors; the instruments are commonly referred to as electron microprobe analyzers. A detailed discussion of WDS can be found in the article “Electron Probe X-Ray Microanalysis” in this Volume.

Sampling Volume for Various Signals

To correctly interpret the physical significance of various signals used in scanning electron microscopy, the volume below the surface from which the signal is originating must be known. Monte Carlo simulations (Fig. 28) depict 2000 electron trajectories for a 20 keV primary beam in iron. The BEs correspond to the red trajectories and help to provide an estimate of the BE signal volume. The BEs emerge from depths extending up to $\sim 0.5 \mu\text{m}$ from the surface, according to Fig. 28. The x-ray signal can be presumed to emanate from a volume that corresponds to the entire interaction volume, as denoted by the blue trajectories. Therefore, although the electron spot size, d_s , may be 1 to 10 nm, x-rays are generated over a volume exceeding $\sim 1 \mu\text{m}^3$. Table 5 lists some estimates of sampling volume in iron for various signals generated by a 20 keV electron beam.

In general, some considerations must be made when quantitatively analyzing size and composition for particles with diameters less than approximately 1 to 2 μm (Ref 30). It is important to note that the x-ray sampling volume and shape vary with the electron beam energy and the sample atomic number. In general, higher voltages, lower density, and lower-atomic-number elements produce larger volumes, which tend to “balloon out” below the beam. Thin foil samples are used to reduce BE and x-ray generation volume. Sampling diameters $< 5 \text{ nm}$ can be achieved simply by using thin foil samples (Ref 23).

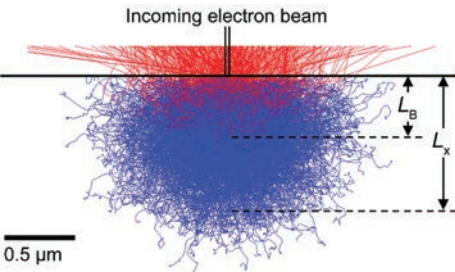


Fig. 28 Monte Carlo simulations of 2000 electron trajectories for a 20 keV primary beam in iron; red denotes trajectories that produce backscattered electrons, and blue denotes those that do not. Backscattered electrons emerge from depths extending up to $\sim 0.5 \mu\text{m}$ from the surface.

Image Contrast

The primary types of image contrast in the SEM are topographic and compositional. Topography refers to the physical shape and arrangement of surface features. Composition refers to the identity, density, and distribution of chemical elements present in the specimen. The SEM image results from variation in signal intensity, S , as the beam moves from point to point on the sample surface. Information on composition and topography of the sample requires interpretation of contrast, $\Delta S/S$, between different points or areas in the image. Variations in the detected signal from two points on a surface can arise from two physically different mechanisms: emission (the number of electrons emitted from the surface) and collection (the number of electrons reaching the detector).

Consider the SE signal shown in Fig. 9(a). When the beam is at positions 2 and 4, the number of SEs emitted from the surface is roughly the same, because the beam/surface tilt angle is the same. However, because point 4 faces the detector and 2 does not, the SE signal is much higher at point 4. Consequently, in this example, the contrast between points 2 and 4 results entirely from differences in the number of electrons collected. When two points have similar line of sight to the detector, as is the case for positions 3 and 4 shown in Fig. 9 (a), the contrast results mainly from a variation in SE emission due to differences in the beam-surface tilt angle. Therefore, interpreting contrast requires careful consideration of both the effects of variations in electron emission and collection as a function of local topography and/or composition.

Topographic Contrast

Topographic contrast is often intuitive and can be directly interpreted as prominent features exhibiting higher signal intensity than recessed, buried, and shadowed features. Different phase constituents of a microstructure often have different etch rates. Therefore, microstructures can be studied, defined, and identified by a combination of metallographic sample preparation and SEM imaging using topographic contrast. The SEM micrographs

Table 5 Estimation of the volume of various signals produced in iron by a 20 keV electron beam

Signal	Approximate volume dimensions	
	Diameter	Depth
X-ray	$\sim 1.3 \mu\text{m}$	$\sim 1 \mu\text{m}$
Backscattered electrons (BE)		
Elastic (BE 1)	$\sim d_s$...
Inelastic (BE 2)	$\sim 0.8 \mu\text{m}$	$\sim 0.5 \mu\text{m}$
Low loss (BE 3)	$\sim d_s$...
Secondary electrons	$\sim 1.2 d_s$	$\sim 10 \text{ nm}$

are usually recorded with the beam at normal incidence to the surface. Variations in detected signal attributed to topographic features are a function of variations in both collected and emitted electrons.

Collection Variation due to Topography

The SE/BE detector position and collection angle both influence topographic contrast, because surface features influence local collection efficiency for both SEs and BEs emitted from various points on the sample surface. Figure 29(a) depicts the primary beam at two positions relative to a topographic surface bump. At position (1), any emitted SE has clear line of sight to the SE detector (consider an Everhart-Thornley detector), because the surface is high and prominent. At position (2), some SEs can feel the positive +300 V potential at the detector and swing a wide arc to fly over the bump. However, many other SEs with an initial trajectory already toward the detector are reabsorbed by the bump. Therefore, position (1) has higher SE signal intensity than position (2) due to collection variations. Note that from the detector perspective, position (2) lies inside a shadowed region.

The same shadowing effect is also true for BEs. Many BEs emanating from the sample at position (1) in Fig. 29(b) have clear line of sight to a BE detector positioned similar to the SE detector. The collection variation due to topography is perhaps more pronounced for BEs than SEs if considering similar detector geometries. Higher-energy BEs do not change trajectory in the presence of a +300 V bias like the <50 eV SEs. Therefore, virtually

none of the BEs emitted at position (2) can reach the detector in Fig. 29(b).

The resulting shadowing effect can provide intuitive assessment of surface topography. Raised areas of the surface inclined toward the detector are bright, and recessed and shadowed regions are dark. The resultant image appears as if the surface was illuminated by a light source located at the detector position. The degree of shadowing can be enhanced by lowering the collection angle. Everhart-Thornley detectors are conventionally mounted above, but to the side of, the specimen. Solid-state detectors (SSDs) positioned directly above the sample are sufficiently large enough in size to collect electrons at both low and high take-off angles. Many SSDs compartmentalize circular collection areas into segments such as quadrants and annular rings. This enables the user to select the electron signal from particular take-off angle ranges. In-lens detectors can only collect high-take-off-angle electrons, so shadowing effects and associated topographic contrast from collection variations are low.

Emission Variations due to Topography

The relative angle between the incoming primary electron beam and sample surface has a strong influence on the resultant emission of both SEs and BEs. As mentioned previously, it is

standard in the SEM for the primary beam to be normal, or 90°, to the sample surface plane. Decreasing the incident angle of the primary beam serves to lift more of the interaction volume closer to the surface, as previously shown in Fig. 23 in the case of sample tilting.

Figure 30(a) depicts a similar situation for a topographic feature, where a larger fraction of the interaction volume is closer to the surface at position (1) than position (2). For the same SE escape depth in both situations, more SEs are emitted at position (1) than for position (2). Therefore, detected SE signal is higher at position (1) than for position (2) due to emission differences. Note that position (2) in Fig. 30 is located far enough away from the bump that the collected SE signal is comparable to position (1) in Fig. 29 (the top of the bump). Thus, Fig. 30(a) illustrates topographic contrast purely due to emission differences instead of collection differences. The same topographic contrast result also occurs for the case of BE emission, although the corresponding BE escape depth is larger.

Edge effect is a phenomenon where electron emission is significant as the primary beam approaches edges nearly parallel to the incident beam direction; edge effect is more pronounced at higher accelerating voltages. Comparing Fig. 30(a) and (b) illustrates the edge effect. Figure 30(b) depicts a higher-energy primary beam interacting with the same

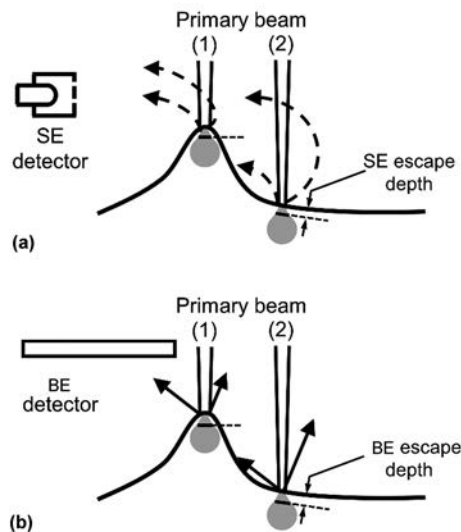


Fig. 29 Illustration of (a) secondary electron (SE) and (b) backscattered electron (BE) collection variations due to line of sight that produces topographic contrast during scanning electron microscope imaging. Position (1) produces more signal intensity than position (2).

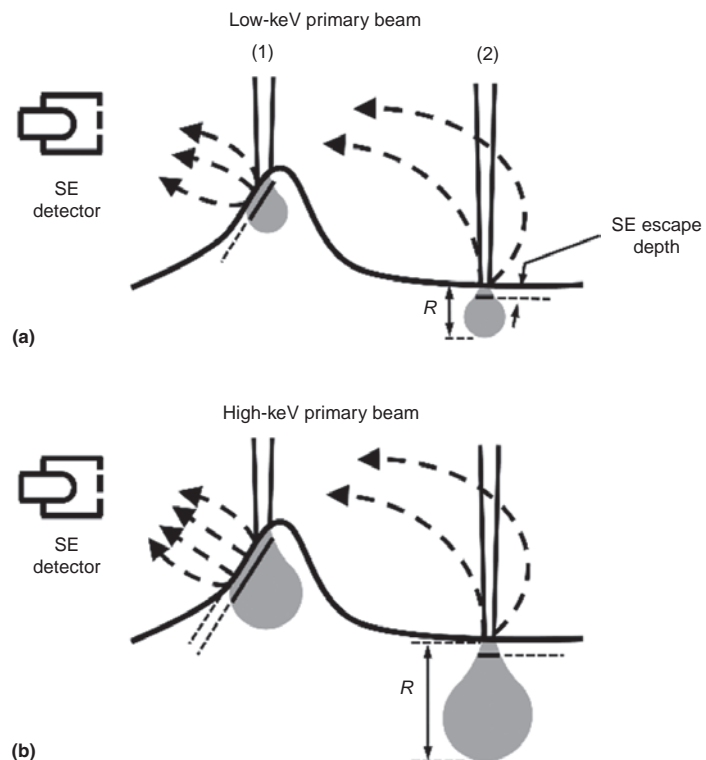


Fig. 30 Illustration of secondary electron (SE) emission variations for (a) low- and (b) high-kiloelectron volt (keV) primary beam energy. Topographic contrast is produced due to sample tilt effects on SE emission variations, such that position (1) produces more signal intensity than position (2). This effect is more pronounced at higher primary beam energies.

bump feature as Fig. 30(a). The interaction volume and corresponding penetration depth range, R , is larger for the higher-energy primary beam. However, the SE yield does not change significantly at position (2), because the interaction volume is extended away from the flat surface. However, increasing the interaction volume at an inclined surface extends the amount of interaction volume that falls within the SE escape depth. Therefore, increasing the energy of the primary beam (higher acceleration voltage) produces higher SE emission at position (1). In addition to the intuitive shadowing effect described previously, SEM imaging at higher (>15 kV) acceleration voltages produces a significant glow at steep edges due to the edge effect. The edge effect is less pronounced for BEs, because the average take-off trajectory from steep edges is often too low to reach the BE detector positioned somewhere above the specimen.

Compositional Contrast

Backscattered electron detection is advantageous for producing SEM images with compositional contrast. Compositional contrast exhibits relatively brighter and darker regions based on the local average atomic number and material density. Composition contrast is indirectly possible by SE detection even though SE emission is generally insensitive to atomic number. Enhancing overall SE collection yield improves the total signal, S , and thus can improve sensitivity to small but detectable signal variations induced by local changes in composition.

Backscattered Electron Emission Variations due to Composition

While SE and BE detection are both useful for topographic imaging, BE detection is also advantageous for producing SEM images with compositional contrast. Polyphase materials and complex alloys can be prepared using standard metallographic polishing techniques yet produce no surface relief. Therefore, topographic contrast by SEM imaging is minimal, and no insight on the microstructure can be obtained. Compositional contrast exhibits relatively brighter and darker regions based on the local average atomic number and material density. Microstructures composed of various constituent phases can be analyzed and identified based on the spatial variations in grayscale attributed to compositional contrast. Backscattered electron detection is more sensitive to compositional variations of a flat surface than SE detection.

Compositional contrast by BE detection is explained by considering the primary beam interaction with the specimen. Backscattered electrons are high-energy electrons from the primary beam that are scattered back out from the specimen surface. It is the individual atomic nuclei within the specimen that serve to scatter primary beam electrons. The

scattering is a strong function of the physical size of the atomic nuclei, which is defined by the element and associated atomic number, Z . With higher Z , more primary beam electrons are scattered closer to the surface. Therefore, the overall probability of BEs escaping the interaction volume is increased, and higher BE emission is produced with larger Z .

Figure 31(a) illustrates composition contrast by BE imaging. Position (1) corresponds to a higher- Z region, which produces a smaller interaction volume than the lower- Z region corresponding to position (2). In Eq 9, R decreases with increasing Z and p . Because R is smaller in the higher- Z region, more of the interaction volume falls within the BE escape depth. Therefore, for the same primary beam electron energy, position (1) emits more BEs than position (2). Because BE detection relies on line of sight, a large-area BE detector position above the specimen surface can collect a large fraction of BEs produced at both positions. The result is clear contrast due to BE emission differences between the high- Z region (high BE signal intensity) and low- Z region (low BE signal intensity). Figure 31(b) presents measured SE and BE yield as a function of atomic number. The SE yield increases moderately with higher atomic number. However, BE yield increases significantly with higher atomic number.

Figure 31(c) illustrates the enhanced compositional contrast provided by BE imaging over SE imaging. The iron sample in Fig. 31(c) contains 3 wt% Y, forming a dual-phase alloy composed of iron and Fe_{17}Y_2 . The specimen was oxidized at 1000 °C (1830 °F) and cross sectioned to determine the extent of oxygen penetration inside the sample (from the top in the micrographs) and the oxidized region thickness denoted by the white line in Fig. 31(c). The SE image on the left in Fig. 31(c) exhibits very little contrast throughout the sample. Because the Fe_{17}Y_2 phase has a higher average Z than iron, it also has a higher BE yield. Therefore, the BE image on the right in Fig. 31(c) exhibits clear composition contrast between the Fe_{17}Y_2 (bright regions) and iron (dark regions) below the oxidation zone. Because Fe_{17}Y_2 preferentially oxidizes, the average Z differences between the two phases are reduced inside the oxidation zone, so the compositional contrast becomes weaker above the white dotted line. Thus, the BE image also provides a clear indication of the oxidation zone through compositional contrast.

Increasing the acceleration voltage has only a small effect on overall BE yield. The higher-energy primary beam produces larger R , deeper penetration, and larger interaction volumes. In the higher- Z region, a slight lateral extension of the interaction volume leads to slightly more area within the BE escape depth where BE emission can occur for position (1). So, a slight BE emission increase is possible with higher acceleration voltage for high- Z regions. However, the lower- Z region does not scatter the primary

beam as efficiently as the higher- Z region. Therefore, much of the interaction volume progresses deeper into the low- Z region with corresponding increase in the BE escape depth, because the primary beam electrons have more energy. The result is a negligible change in overall BE emission with increased acceleration voltage for low- Z regions.

Figure 32 presents SEM micrographs of an as-polished (not etched) multiphase alloy acquired using a segmented, annular pole-piece BE detector. The insets in Fig. 32 depict which segment of the BE detector is used. Two phases, denoted as areas (1) and (2), exhibit different signal intensities due to compositional contrast in Fig. 32(a) and (b) when using either half-segment of the BE detector, A or B. However, the compositional contrast becomes stronger in Fig. 32(c) when both half-segments are used together, A + B. When segment B signal is subtracted from segment A, the resultant

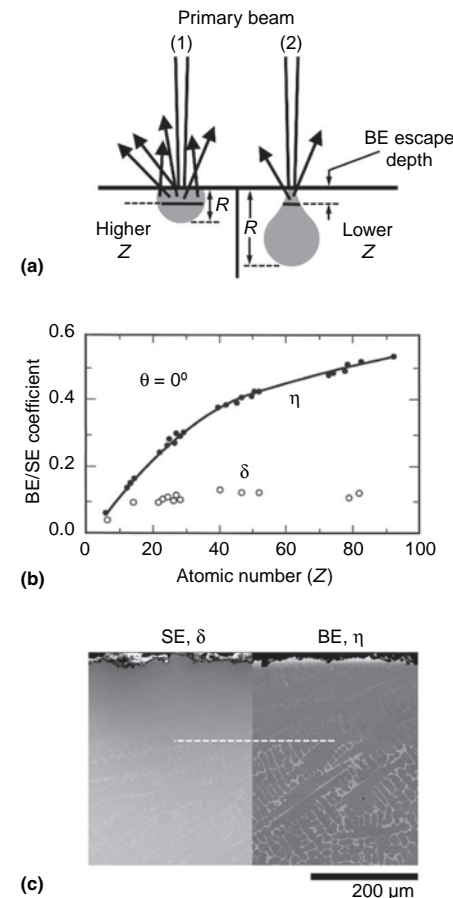


Fig. 31 (a) Illustration of compositional contrast due to backscattered electron (BE) emission variations from a flat surface with regions of higher and lower average atomic number, Z . (b) Plot of measured secondary electron (SE) and BE yield as a function of atomic number. Source: Ref 27. (c) Reprinted/adapted from Ref 27 with permission of Springer Nature. Copyright 2003. (c) Cross-sectional scanning electron micrograph of an oxidized dual-phase iron-yttrium alloy recorded by (left) SE and (right) BE detection. Courtesy of A. Weiss and B. Webler, Carnegie Mellon University

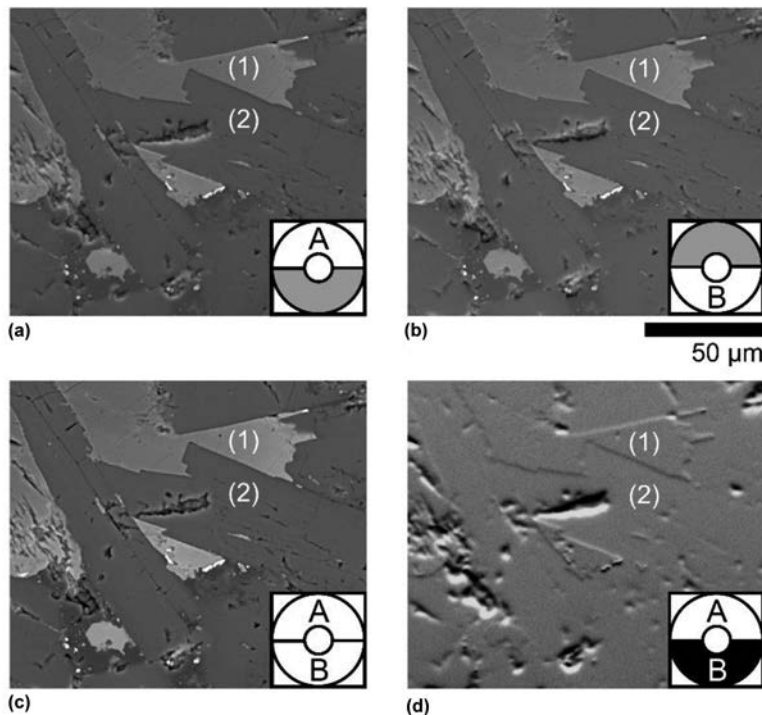


Fig. 32 Backscattered electron (BE) micrographs of a polished multiphase alloy surface recorded using a segmented, annular BE detector mounted to the scanning electron microscope pole piece. Insets indicate BE signal contribution from the detector segments: (a) A, (b) B, (c) A + B, and (d) A – B. Courtesy of Thermo Fisher/FEI

image shows no compositional contrast between the two phases. An elongated gouge near area (2) in the center of the image provides a useful topographic, fiducial feature. In Fig. 32(a), the lower edge of the gouge is bright due to higher BE emission, and the upper edge is dark due to lower BE collection when using the A segment. The topographic contrast is reversed for the case of the B segment in Fig. 32(b). Summing A and B segment signals together serves to reduce topographic contrast, as shown in Fig. 32(c), while subtracting B signal from A serves to enhance topographic contrast, as shown in Fig. 32(d). Topographic contrast in Fig. 32(d) is sufficiently strong enough to indicate that area (1) is raised in relation to area (2). This shows that signals from segmented BE detectors can be used to preferentially boost or suppress either contrast mechanism.

Secondary Electron Emission Variations due to Composition

Composition contrast is indirectly possible by SE detection even though SE emission is generally insensitive to atomic number, as was shown in Fig. 31(b). Secondary electron emission is a strong function of electrical properties of the material surface, so SE contrast between metals and insulators can be significant (Ref 31). Even variations in the doping level of semiconductors can be resolved by

SE emission variations (Ref 32). Enhancing overall SE collection yield improves total signal, S , and thus can improve sensitivity to small but detectable signal variations induced by local changes in composition. Reducing acceleration voltage decreases the range of beam penetration, R . Consequently, more primary beam electrons undergo scattering closer to the near surface, improving overall SE emission. Thus, lowering the acceleration voltage for a very flat sample produces higher S , lower N , and potentially enough ΔS , which could be attributed to composition or general material variations.

Another way to enhance SE signal sensitivity is by optimizing the SE detector position. Like BE emission, SE emission increases at higher take-off angles. In-lens detectors are optimally positioned to detect these high-take-off SEs. Shadowing due to line-of-sight effects is mitigated by the detector geometry, so any competing contrast from specimen topographic effects is relatively low. It is possible to optimize the collection of SEs by using a combination of low (<10 kV) acceleration voltage, smaller WD, and in-lens/in-column detectors. This approach helps to enhance point resolution, because high-take-off SEs are predominantly SE(1) type. Although this combination of approaches also improves SEM sensitivity to possible local SE emission variations due to composition, great care must be exercised in attributing SE signal variations to composition

(Ref 31). Many other physical characteristics of the sample surface can influence SE emission, as discussed in the next section.

Other Contrast Mechanisms

In addition to topography and composition, several other contrast mechanisms are directly related to SE and BE emission variations. Contrast mechanisms described are readily accessible in conventional SEMs using typical SE and BE detectors. This section describes SEM contrast due to a variety of material surface properties, including surface charge, surface potentials, magnetic properties, and crystal structure/orientation.

Charge Contrast

During SEM imaging, the sample is bombarded by negatively charged electrons. If unable to dissipate, electrons accumulate and produce electrostatic charge of the surface. Negative charge buildup lowers the primary beam landing energies and enhances SE emission. Charge buildup can be stochastic and fluctuate the SE signal during beam raster across insulating surfaces. The resulting charge contrast is generally unwanted in SEM images and can be problematic when imaging nonconductive samples. Generally, nonconductive samples are coated with a thin layer of an electrically conducting material to avoid charging effects. However, charge contrast can arise even in nominally conductive samples, such as a steel containing ceramic inclusions. Despite being flat and having lower average atomic number, an insulating particle, such as an alumina (Al_2O_3) inclusion in steel, exhibits higher signal due to charge contrast than the surrounding iron matrix. Charge contrast must be considered when SEM imaging composite materials containing nonconductive components. Charge contrast can be mitigated by using a higher acceleration voltage, lower beam current, and faster scan speed. Backscattered electron imaging is less susceptible to charge contrast than SE imaging.

Voltage Contrast

Electrically isolated or floating structures at the specimen surface can produce different surface potentials. As mentioned previously, the presence of a surface potential alters the landing energy of the primary beam in the SEM. At low SEM acceleration voltages (<5 kV), any variation in the landing energy of the primary beam makes detectable changes in the SE yield. Therefore, local SE emission variations, or voltage contrast, can be used to image and even measure surface potentials for various electrical structures and devices. In-depth studies of electrical device behavior can be performed by applying an external bias to device elements and spatially measuring

surface potentials via voltage contrast SEM. Another approach to obtain voltage contrast in the SEM is by measuring SE energy distribution using an energy analyzer. Applied voltage to a specimen induces a systematic, measurable shift of the entire SE energy spectrum. More details regarding voltage contrast in the SEM can be found in Ref 33.

Magnetic Contrast

It is possible to obtain images of magnetic domains in the SEM. Ferromagnetic materials are composed of small subgrain-sized regions termed domains. In every domain, the magnetic moment of each electron has a common direction along a certain crystallographic axis, which is often termed the easy axis. In certain crystals, such as cobalt, there is only one easy axis; such crystals are termed uniaxial crystals. In the crystals, the magnetic moment at a surface often has a component normal to the surface, which means that a small magnetic flux, **B**, will “leak” out of the surface. Thus, an SE ejected from the surface of a uniaxial crystal with velocity *v* experiences a Lorentz force $\mathbf{v} \times \mathbf{B}$. Because the local external flux changes sign over each domain, the change in the Lorentz force causes the SE detector signal to change when the beam moves over each domain; thus, images of domains can be obtained using the SE signal. This contrast is known as type I magnetic contrast.

In most ferromagnetic crystals, there is more than one easy axis; for example, in α -iron they are [100], [010], and [001]. In these crystals, closure domains form at the surface that have their moment lying along the easy axis most closely parallel to the surface, which greatly reduces the magnetic flux leakage outside the surface. Domains are revealed by type II magnetic contrast in these crystals. Inside the metal, there is an abrupt change in the magnetization direction at a domain boundary. This means that the direction of **B** switches from domain to domain inside the metal. Therefore, after entering the sample, a primary electron experiences a Lorentz force in different directions from domain to domain, which results in changes in the backscattering yield as the primary beam sweeps across a domain boundary. Therefore, the BE detector is used to detect type II magnetic contrast. More details regarding magnetic contrast can be found in Ref 29 and 34. Detailed information on techniques used to observe domain structures can be found in the article “Microstructure and Domain Imaging of Magnetic Materials,” *Metallography and Microstructures*, Volume 9, ASM Handbook, 2004.

Channeling Contrast

Channeling contrast relates to emission variations due to the local crystal structure and orientation of the specimen. Figure 33 illustrates the mechanism for electron channeling contrast. Consider the case of low-magnification

(<100 \times) SEM imaging of a monoatomic, topographically flat, nominally strain-free single-crystal sample with a crystallographic surface plane oriented normal with respect to the incoming primary electron beam. Because of the cubic single-crystal orientation, at least one set of (*hkl*) planes lies vertically with respect to the surface, as illustrated in Fig. 33(a). As the beam scans from positions 1 to 4, it scans over angular range, γ , while also varying an angle θ with this (*hkl*) plane set. If θ_B scans over angular range, γ , while also varying the Bragg angle for diffraction, then:

$$n\lambda = 2d_{hkl} \sin \theta_B \quad (\text{Eq 10})$$

where λ is the wavelength of the electron beam. Wavelength varies inversely with the acceleration voltage.

Figure 33(b) illustrates BE emission variations due to electron channeling plotted as a function of angle θ . As the primary beam scans across θ_B at points 2 and 3, a strong drop and then increase in BE yield results. The term *channeling* is a slight misnomer, because it implies that the primary beam electrons channel down the (*hkl*) planes and penetrate deeper within the material. However, it is more accurate to regard the electrons as having a stronger interaction with the vertical planes when $\theta < |\theta_B|$; this produces elevated BE yields (Ref 35). Therefore, when the beam lies between positions 2 and 3, the BE signal is higher over a spatial angular width, *B*, with strong dips in signal intensity just outside positions 2 and 3.

Figure 33(c) presents an experimental BE image obtained at low magnification of a single-crystal aluminum specimen with the (111) crystallographic surface oriented normal to the incoming 30 keV electron beam. The black cross denotes $\theta = 0^\circ$, where the electron beam is exactly parallel to the [111] direction. Assuming the (111) surface is exactly normal to the electron-optic axis, this point also corresponds to $\gamma = 0^\circ$. Thus, this position is considered the center of the electron channeling pattern. Three pairs of channeling lines are clearly observable, and each line corresponds to a specific set of aluminum {220} planes. The white dotted line in Fig. 33(c) corresponds to the BE intensity profile illustrated in Fig. 33(b). Using Eq 10, θ_B is $\sim 0.7^\circ$ for the aluminum {220} family of planes. Therefore, the channeling bandwidth, *B*, for each pair of channeling lines corresponds to the $2\theta_B$ value, or 1.4° . This illustrates that the electron channeling pattern (ECP) provides angular information regarding the primary beam trajectory with respect to crystallographic planes. Any location along a single channeling line represents satisfaction of the Bragg condition for that specific set of planes. For example, points 2', 2a', and 2b' in Fig. 33(c) represent positions where the primary beam is at an angle θ_B with respect to the ($\bar{2}20$) planes.

The crystallographic orientation of the single-crystal region beneath the beam can be evaluated from the ECP. Decreasing image

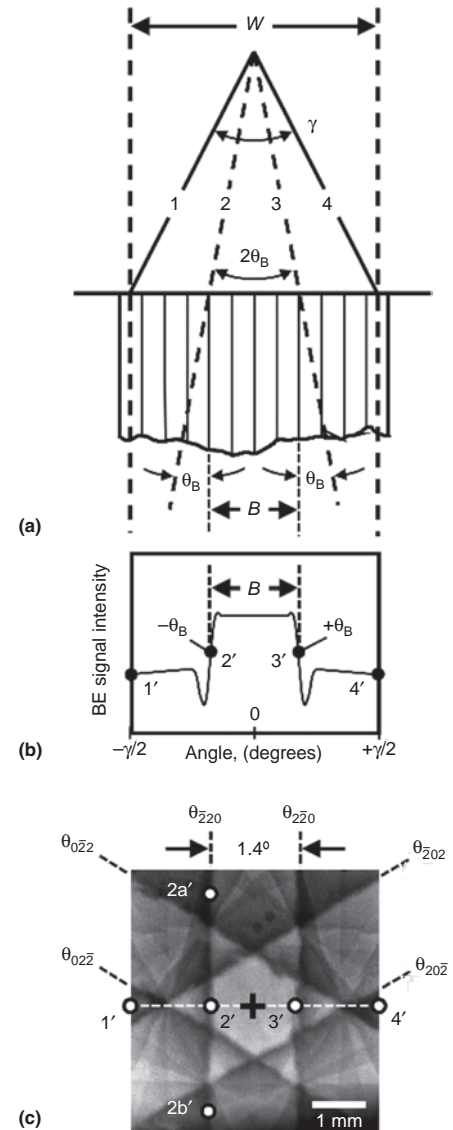


Fig. 33 Electron channeling contrast. (a) Illustration of low-magnification, underfocused imaging of a single-crystal sample. (b) Resultant backscattered electron (BE) signal variation due to electron channeling. (c) Experimental low-magnification BE image of an aluminum (111) single crystal exhibiting channeling contrast that results in an electron channeling pattern. Vertical {220} planes with respect to the aluminum (111) surface are identified. Courtesy of J. Kamaladasa, Carnegie Mellon University

magnification increases the range of scan angle, γ , as well as the image width, *W*. The result is a broader crystallographic view of the single-crystal sample. Considering typical SEM acceleration voltages of 2 to 30 kV, the nonrelativistic wavelength can vary from 0.007 to 0.027 nm. Because the values are an order of magnitude smaller than typical crystallographic plane spacings, d_{hkl} , the Bragg angles from Eq 10 range in values from ~ 0.3 to 5° . Therefore, only very low-magnification (<100 \times) imaging can swing the beam over an angular range, γ , large enough to span $2\theta_B$

for any set of crystallographic planes. Electron channeling patterns are essentially the same as Kikuchi patterns obtained from thin foil samples in transmission electron microscopes. Just as Kikuchi patterns enable evaluation of crystallographic orientation more precisely than is possible with the electron diffraction pattern, the ECP enables more precise orientation evaluation than an x-ray Laue pattern. In general, ECPs for phase and orientation determination have not seen development as compared to the more established and commercialized electron backscatter diffraction approach, described in the section “Special Techniques” in this article.

Channeling contrast is surface sensitive, because signal contribution is dominated by BEs with little or no energy loss. Therefore, crystallographic information is carried by electrons scattered from depths below the surface of only 10 to 100 nm, so sample preparation is important. For metals, the worked surface layer produced by standard metallographic specimen-preparation techniques degrades and, in some cases, eliminates ECPs due to the variation in d_{hkl} produced by residual strains. With more brittle materials, such as intermetallic compounds and semiconductors such as germanium and silicon, residual strains are less of a problem. Because the effect that produces channeling contrast involves BEs with minimal energy loss, channeling patterns and channeling contrast are better observed using dedicated BE detectors, where maximizing overall BE collection efficiency and increasing signal gain is critical.

Figure 34 illustrates channeling contrast as a method to observe grain size and twinning for a polished, highly flat polycrystalline copper sample. Grain boundaries would not be visible in the optical microscope and may only vaguely be detected by the SE imaging in the SEM. The contrast shown in Fig. 34 is due to the different crystallographic orientations of the various grains, which result in grayscale variations across the BE image. As the sample is tilted or rotated, the BE emission for each grain changes. For the largest grain located at the bottom-center in the images, a 1° stage tilt is enough to cause inversion of the dark/light contrast compared with microtwins within the grain. Examples 3 and 6 in the section “Applications” in this article show BE micrographs exhibiting orientation contrast by electron channeling.

Material extended defects, such as dislocations and stacking faults, induce localized atomic structure variations due to elastic strain, which results in subtle orientation changes detectable by electron channeling contrast only when the beam is oriented near a diffraction condition. Used as an imaging technique, electron channeling contrast enables SEM-based defect imaging and identification. The electron channeling contrast imaging (ECCI) method relies on controlled orientation of the incoming electron beam to a specific Bragg angle, θ_B .

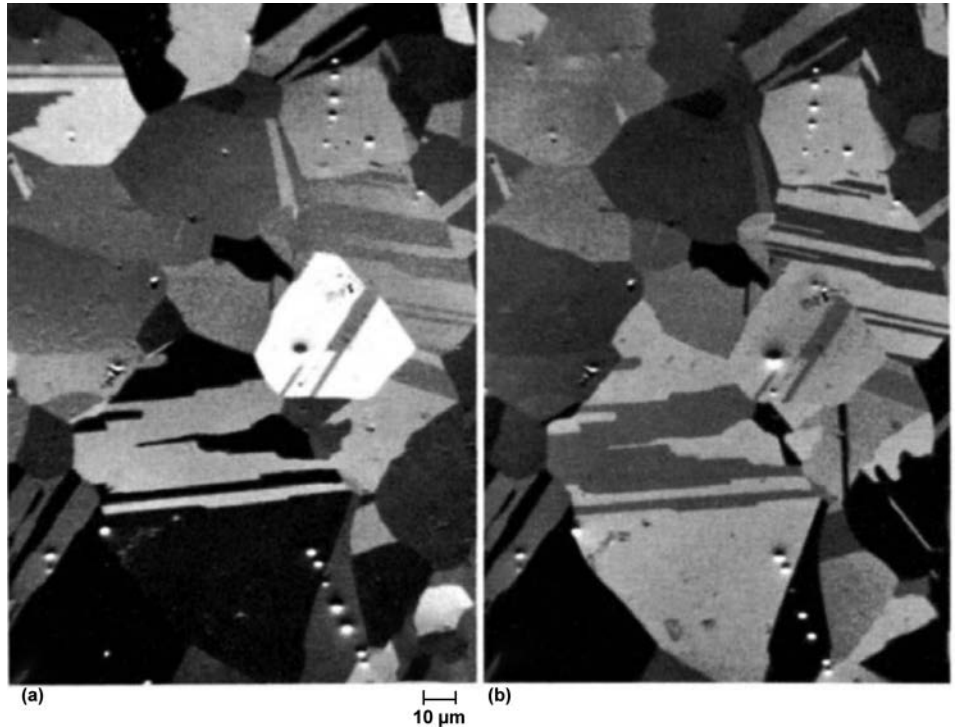


Fig. 34 Backscattered electron micrographs of electrolytically polished polycrystalline copper exhibiting orientation contrast due to electron channeling effects. A 1° tilt produces significant changes in the grain contrast between (a) and (b). Reprinted/adapted from Ref 14 with permission of Springer Nature. Copyright 1998

Any local lattice strain that bends the specific set of crystallographic planes corresponding to θ_B yields BE contrast, as illustrated in Fig. 35.

Figure 35(a) illustrates high-magnification SEM imaging of a single-crystal surface containing a single near-surface edge dislocation. The dislocation produces elastic strain that varies the local crystallographic plane orientations with respect to the incoming electron beam. An angle, $\Delta\theta_s$, denotes this orientation variation induced by the defect. The beam is scanned across this defect at an initial trajectory that satisfies the Bragg condition for these planes: $+\theta_B$ at points 1 and 5, and $-\theta_B$ at points 6 and 10. The resulting BE yield is presented in Fig. 35(b) as a function of angular deviation from the Bragg angle, θ_B . Points 2 and 9 in Fig. 35(a) correspond to conditions where the crystallographic planes are oriented more parallel to the incoming electron beam. This leads to a higher BE yield, as illustrated for points 2' and 9' in Fig. 35(b). Likewise, there is a drop in BE yield for points 4 and 7 where crystallographic planes are bent away from the Bragg condition toward a direction less parallel to the incoming electron beam trajectory.

Figure 35(c) presents BE images of near-surface dislocations in a SrTiO_3 (100) single-crystal sample. The dark-light vertical line feature is a near-surface dislocation parallel to the surface; spot features denote surface-penetrating dislocations inclined 45° to the

(100) surface. The observed channeling contrast of the dark-light vertical line correlates to the BE intensity profiles illustrated in Fig. 35(b). It should be noted that the change in sample tilt/orientation is only $\sim 1^\circ$ to go from $+\theta_B$ to $-\theta_B$, yet the features in Fig. 35(c) exhibit a complete reversal in BE intensities. Thus, features cannot be attributed to topographic contrast or composition contrast. The directionality of the BE intensity fluctuation depends on whether the incoming trajectory is initially at $+\theta_B$ or $-\theta_B$ for a specific set of crystallographic planes.

The implication regarding channeling contrast is that the user must select which set of planes will yield channeling contrast. This is accomplished by obtaining an ECP and adjusting the sample orientation so the channeling line is centered on the optic axis. This ensures that the primary electron beam is nominally at an angle corresponding to θ_B . The diffraction vector, \mathbf{g} , defines the direction normal to the planes selected for channeling contrast. A series of ECCI micrographs can be recorded at different channeling conditions for dislocations of interest. Based on the contrast behavior as a function of \mathbf{g} , dislocations can be identified by their Burgers vector either through comparisons to dynamical diffraction simulations (Ref 36) or through the use of the invisibility criterion (Ref 37).

Because it is necessary to obtain crystal orientation information from a localized region,

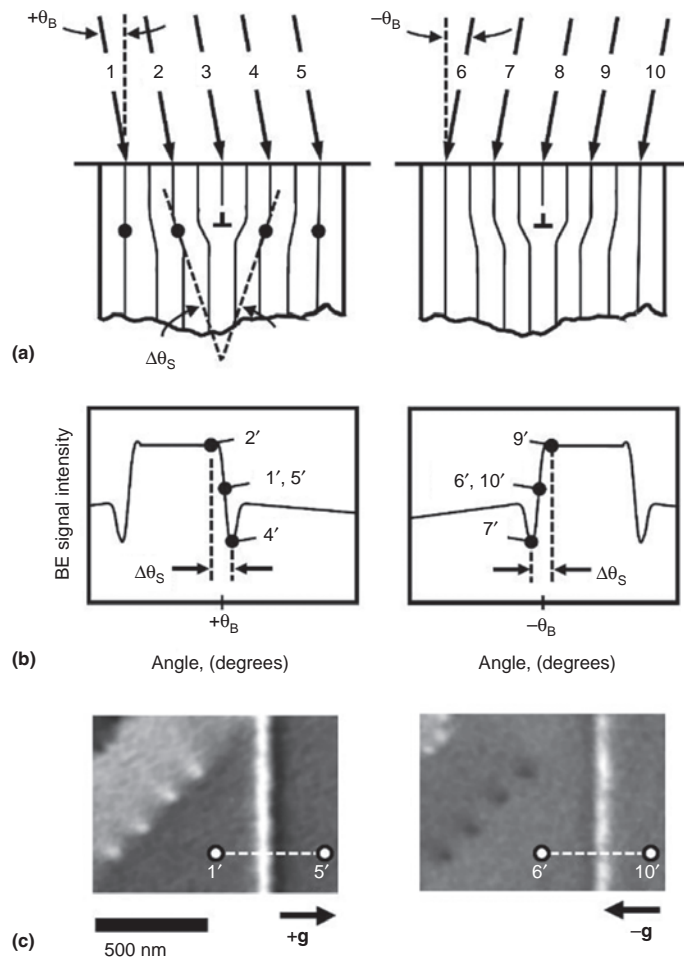


Fig. 35 (a) Illustration of scanning electron microscope imaging of a single-crystal surface containing a single near-surface edge dislocation producing local orientation variation, $\Delta\theta_S$. (b) Resultant backscattered electron (BE) yield as a function of beam position. (c) Experimental electron channeling contrast imaging micrographs of near-surface dislocations in a SrTiO_3 (100) single-crystal surface imaged under two different tilt conditions, corresponding to trajectory angles $+\theta_B$ and $-\theta_B$, or $+g$ and $-g$. Experimental micrographs courtesy of J. Kamaladasa, Carnegie Mellon University

the SEM must acquire an ECP for a specific location. Therefore, the SEM must swing the incoming electron beam across a wide angle, γ , but consistently sample a selected area of the specimen surface. An example electron-optics arrangement is shown in Fig. 36(a), which can accomplish the selected-area channeling pattern (SACP) acquisition using a conventional SEM. Both sets of scan coils coordinate with the objective lens to maintain a consistent rocking point at the sample surface. Rocking angles of ~ 5 to 15° are possible for selected areas from $20\ \mu\text{m}$ down to $<1\ \mu\text{m}$ in size (Ref 38). Figure 36(b) shows an example BE micrograph of a steel sample where individual grains exhibit orientation contrast due to channeling. The SACPs acquired from four different grains highlight the orientation differences from grain to grain. Some commercial SEMs are designed with a beam-rocking or SACP mode to facilitate the use of channeling contrast.

Special Techniques

Special techniques include electron backscatter diffraction capable of determining local crystal structure to map microstructure; electron beam induced current, which is useful for semiconductor device characterization, defect imaging, and failure analysis; cathodoluminescence, where detected photons have energies characteristic of the local sample electrical and optical properties; in situ and in operando methods for imaging and analysis of specimens under specific conditions to observe dynamic phenomena, such as phase transitions, surface chemical reactions, and microstructural transformations; low-voltage SEM analysis performed using a low acceleration voltage that leads to improved detail of fine surface features when detecting SEs or BEs; and commercial TEM detectors inside the SEM chamber to facilitate transmission-mode imaging for enhanced image resolution

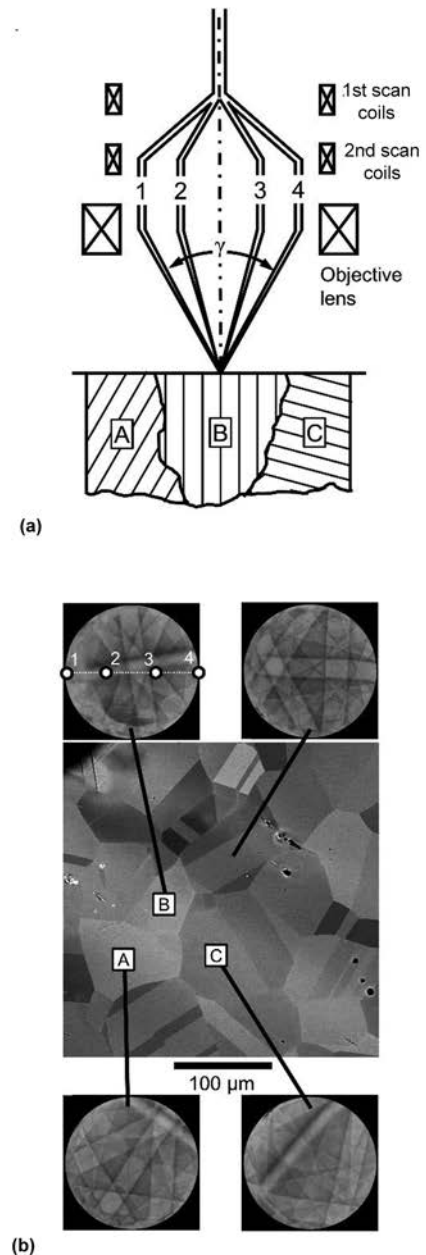


Fig. 36 (a) Illustration of beam rocking to produce a selected-area channeling pattern (SACP) from a single grain (grains denoted by A, B, and C). (b) Backscattered electron micrograph of a polished steel sample with four example SACPs acquired from individual grains. Courtesy of S. Singh and M. De Graef, Carnegie Mellon University

sufficient to resolve atomic structure and produce diffraction contrast images.

Electron Backscatter Diffraction

Electron backscatter diffraction (EBSD) is an SEM-based approach capable of determining the local crystal structure, including phase and orientation, to map microstructure. Electron backscatter diffraction is used to produce

a variety of maps that provide tremendous insight on the crystallographic properties of materials, including elastic strain, plastic deformation, grain size, grain boundaries, geometrically necessary dislocations, and texture. While predominantly applied for investigating metal microstructures and geological samples, EBSD is being increasingly used for semiconductors and nanomaterials.

Electron backscatter diffraction, illustrated in Fig. 37, uses a two-dimensional scintillator detector and a charge-coupled device camera to image the angular spread in BE intensity emanating from a single point. Because the electron beam undergoes both inelastic and elastic scattering within the BE escape depth of the specimen, the projected BE intensity on an area detector produces a Kikuchi pattern. The pattern contains bands, each of which represents a set of crystallographic planes, similar to the channeling bands described in the earlier section "Channeling Contrast" in this article. Band configurations can be used to identify both the crystallographic phase and the orientation of the local crystal structure. Point-by-point acquisition of multiple Kikuchi patterns produces a comprehensive map of crystallographic structure for in-depth analysis of material microstructure.

Typically, the sample is tilted $\sim 70^\circ$ with respect to the incoming electron beam; the EBSD camera is brought within a few centimeters of the inclined sample surface. This geometry is advantageous, because the forward-scattering electron yield is substantially higher than for a backscattered geometry at 0° sample tilt, as illustrated in Fig. 23 and demonstrated in Fig. 22. Gain control and background subtraction are used to improve the Kikuchi pattern quality. Conventionally, a Hough transform is applied to an acquired Kikuchi pattern so individual bands can be identified.

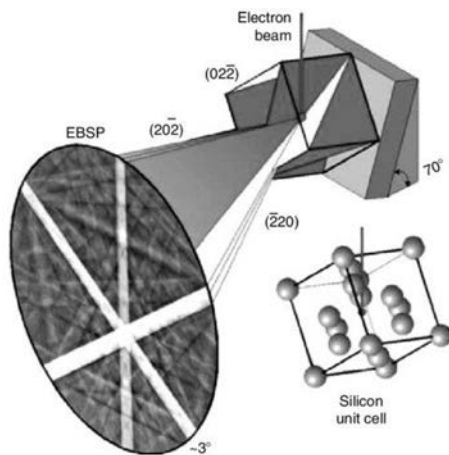


Fig. 37 Illustration of electron backscatter diffraction method where a sample is tilted 70° and the band configurations within an acquired electron backscatter pattern (EBSP) indicate the local crystal orientation. Reprinted/adapted from Ref 39 with permission of Springer Nature. Copyright 2006

The user proposes possible crystal structures, and the software compares the configuration of the detected bands to a look-up table of interplanar angles for the phases of interest. A best match is determined, and the corresponding orientation is assigned to each pixel position. The orientation is assigned based on three Euler angles, which define the necessary rotation of the local crystal structure to the sample reference orientation. As such, each individual point is assigned both a phase and orientation to produce a map of crystal structure. Adjacent pixel positions with identical phase and similar orientations (within some user-defined threshold misorientation angle) can be assigned to a single grain. Larger changes in orientation for adjacent pixels define the location of grain boundaries. See Examples 2 and 3 in the section "Applications" in this article for cases using EBSD analysis. More details on the EBSD method can be found in the article "Crystallographic Analysis by Electron Backscatter Diffraction in the Scanning Electron Microscope" in this Volume.

Electron Beam Induced Current

This technique is useful for semiconductor device characterization, defect imaging, and failure analysis. Electron beam induced current (EBIC) works by measuring the current between two electrodes in contact with the semiconductor sample. The current is induced by the electron beam as it is scanned across the contact-semiconductor interface and used to modulate grayscale intensity when producing a digital image. When the electron beam strikes the sample surface, electron-hole pairs are created within some interaction volume. If the semiconductor contains an internal electric field near these charge carriers due to, for example, a depletion layer at a p - n junction, as shown in Fig. 38, the charge carriers create a current between the two attached electrodes.

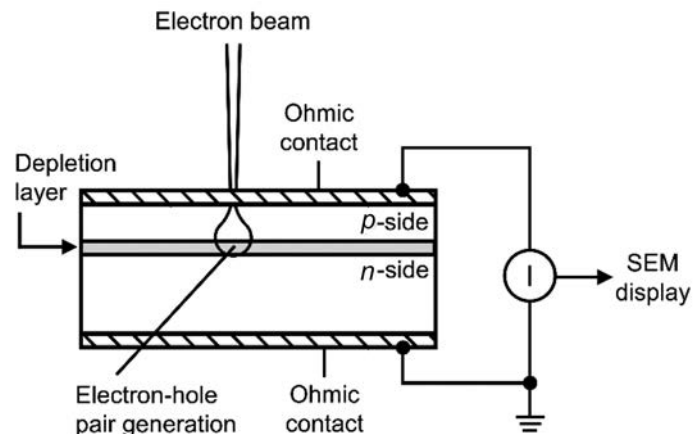


Fig. 38 Illustration of electron beam induced current setup for a p - n junction. SEM, scanning electron microscope

To study crystals that do not contain p - n junctions, a surface Schottky barrier is fabricated on the crystal surface by deposition of a thin metallic layer. The thickness of material beneath the junction depleted of mobile carriers is a function of the applied reverse bias voltage. Crystal defects and composition gradients within this zone that affect the charge dissipation current can be imaged by EBIC. The current used in the EBIC technique is different from the current flow to ground used for specimen current detectors.

It is possible to obtain images of localized crystal defects such as dislocations and stacking faults. In addition, crystal growth defects, such as dopant inhomogeneities, can also be imaged. Factors that control image formation are reviewed in Ref 40. Many electrical parameters of semiconductor devices can be evaluated by using quantitative EBIC techniques, for example, doping level, diffusion length and lifetime of minority carriers, mobility and surface recombination velocity, surface potential, electric field, multiplication factor, and ionization coefficients. In addition, the EBIC technique is used for failure analysis and device diagnostics in such ways as locating a defective device in an array, locating a defect in a device or junction, or locating an irregularity in a junction. A review of EBIC is provided in Ref 41.

Cathodoluminescence

Cathodoluminescence (CL) is the emission of light by a solid under electron beam bombardment. A sufficiently high-energy electron beam excites electrons within the material to elevated energy states that emit photons as they decay back down to their original energy (Ref 42). The photons sit in the visible, near-infrared, and ultraviolet regions of the spectrum with photon energies ranging from 0.5 to 6 eV. Furthermore, the photon energies are

characteristic of the local sample electrical and optical properties. To use CL in the SEM, the light given off by the sample under electron beam irradiation must be collected using a special photon analyzer inside the specimen chamber. This photon analyzer/collector converts the emitted light intensity to an electrical signal. The detected light intensity can be modulated to produce a digital image or measured as a function of photon energy for spectral analysis.

Cathodoluminescence can be performed in the SEM using different modes and detector configurations. By implementing a photomultiplier tube or solid-state diode (SSD), the overall light signal, regardless of color, can be measured as a function of electron beam position to produce two-dimensional panchromatic images. An optical filter or exit slit enables the user to select a specific wavelength or photon energy of interest, thus resulting in monochromatic images. A CL spectrometer disperses all emitted light from a single position, enabling the recording of light intensity as a function of wavelength for one specific pixel. A series of CL spectra recorded at multiple pixel positions produces a three-dimensional, hyperspectral data volume, which can be further analyzed postacquisition. See Example 4 in the section "Applications" in this article for an example monochromatic CL image.

Cathodoluminescence is applicable for any material with an energy gap between the valence band and the conduction band, which applies to semiconductors and insulators. In the case of semiconductors, electron-hole pairs are generated by the energetic electron beam, and the radiative recombination of those electron-hole pairs produces a light signal indicative of the semiconductor bandgap and other optoelectronic properties. The physical basis of CL in semiconductors is comparable to EBIC, being governed by generation, motion, and recombination of excess charge carriers. Therefore, with semiconductors, CL is broadly applied for measuring electronic bandgap, imaging dislocations, and evaluating minority carrier diffusion length and life (Ref 43). It is often used as a complementary tool with EBIC for semiconductor materials and devices. Ceramics, minerals, and gemstones also yield useful information when analyzed by CL (Ref 44). Trace elements present at concentrations too low for detection by EDS or WDS can often be detected and even mapped by CL. Minerals can be dated for geochronology based on CL characteristics (Ref 45).

In Situ and In Operando Methods

For SEM, *in situ* and *in operando* refer to the imaging and analysis of specimens under specific conditions. It may be desirable to perform SEM analysis of specimens at a specific temperature, under a certain strain condition, under applied voltage, or within a liquid/gas

environment. In this way, dynamic phenomena, such as phase transitions, surface chemical reactions, and microstructural transformations, can be observed.

Commercial *in situ* stages are available to apply one or more combinations of external loads. Hot stages are designed to elevate the specimen temperature to as high as 2500 °C (4530 °F) (Ref 46). Water cooling and heat shielding could be required, depending on the target temperature. Cold stages can bring specimens down to cryogenic temperatures, usually through Peltier cooling, liquid nitrogen, or liquid helium. Tensile and compressive stress testing is possible using commercial mechanical stages (Ref 47). These systems typically use a force transducer to monitor and measure applied force and displacement for producing stress-strain measurements. Other mechanical stages provide movable tips and appendages to controllably manipulate features on the specimen surface with submicrometer control. The nanomanipulators can also be used to apply voltage or current to a specific location in a controlled manner. Alternatively, stages can be equipped with prepatterned electrical leads so the specimen can be placed in electrical contact with an external voltage/current source for *in situ* biasing studies. See Example 6 in the section "Applications" in this article for an example study using a hot stage inside an SEM.

Specialized stages are produced with environmental cells that enable the flow of liquids or gases inside the SEM (Ref 19). The cells are encased in a thin membrane capable of retaining the internal pressure of the cell. The membrane also enables transmission of the primary electron beam to the sample as well as signals to the SEM detectors. The user has external control of the interior cell pressure or fluid flow rate during SEM analysis. Noise reduction is crucial under these circumstances because of extensive unwanted scattering due to the cell membrane and the fluid surrounding the specimen. In cases where actual operating conditions (temperature, applied voltage, gas environment) for a specimen are replicated inside the SEM, the analysis is referred to as *in operando*.

Low-Voltage SEM

Low-voltage SEM generally refers to analysis performed using an acceleration voltage lower than 5 kV (Ref 48). The primary effect of using such low-energy electrons is significant reduction in the interaction volume, which leads to improved detail of fine surface features when detecting SEs and BEs. Tilt influence on SE yield decreases with lower voltage, leading to reduced edge effect and improved definition of surface features. For beam energies less than 1 keV, BE escape depths approach the same scale as SE escape depths, leading to BE image resolution comparable to SE imaging (Ref 49).

Other advantages of low-voltage SEM include the ability to image nonconductive specimens, analyze beam-sensitive materials, and access other contrast mechanisms linked to material properties such as electrical conductivity. More details regarding low-voltage SEM can be found in Ref 48 and 49.

Nonconductive specimens present a challenge for conventional SEM due to unwanted charge buildup while the electron beam impacts the specimen. At high voltages, the number of electrons accelerated into the target specimen exceeds the number of BEs and SEs produced. Therefore, excess negative charge accumulates at the site of imaging unless the charge is conducted to ground, either by the specimen itself or with the help of a conductive surface coating. In the absence of a pathway to ground, the buildup of negative charge serves to decelerate incoming electrons and reduce beam penetration to the sample. Lowering incident electron energy has the effect of increasing overall BE and SE yield until a balance is reached and charge is conserved. The critical energy value, E_2 , is an important parameter for low-voltage SEM (Ref 18). The E_2 value is material specific (ranging from 0.5 to 3.0 keV), and represents the desired electron beam energy that ensures charge balance and thus optimal imaging in the SEM for nonconductive specimens. The E_2 values for a variety of glasses, ceramics, and polymers are provided in Ref 18 and 48.

Low-voltage SEM also provides an advantage in reducing the possibility of electron beam induced damage to the specimen, including electrostatic charging, atomic displacement, and specimen heating. Excess charge accumulation can produce electrostatic forces strong enough to modify features on the sample surface. Therefore, attaining charge balance during imaging is a first step in minimizing surface alterations. Damage by individual atom displacement is statistically unlikely to occur when using primary beam electron energies below 100 keV, so displacement damage is negligible for conventional SEM (Ref 50). However, atomic/molecular structural damage can also occur if chemical bonds are altered or even broken by the incident electron beam due to inelastic scattering. For electron energies <30 keV, this form of damage scales with the incident beam energy, so low-voltage SEM is best for sensitive materials.

Note that SEMs are sometimes equipped to enable the user to apply a negative bias at the sample to decelerate the incoming electron beam. This approach enables obtaining electron landing energies down to the electron volt range without sacrificing image resolution. At such low energies, electron penetration into the sample may only extend 1 nm or less. Therefore, contrast is strongly influenced by surface chemistry and surface electrical/magnetic properties. Interpretation of image contrast at such low landing energies is still being explored (Ref 49).

Transmission-Mode SEM

Historically, the primary distinctions between SEM and TEM were the energy range of the primary electron beam and the detector geometry. The SEM uses 5 to 30 keV beam energies compared with the 80 to 300 keV range for conventional TEM. The higher beam energy for TEM also means a preference for positioning detectors below the specimen, because beam-sample interactions predominantly result in very low-angle scattering. Commercial TEM detectors (Fig. 8) were introduced inside the SEM chamber to facilitate transmission-mode imaging. Advantages of conducting SEM in transmission mode include enhanced image resolution sufficient to resolve atomic structure (Ref 51) and producing diffraction contrast images (Ref 9). See Example 5 in the section "Applications" in this article for further demonstration of transmission-mode SEM.

Scanning Electron Beam Instruments

Historically, the SEM was an advanced instrument requiring significant training and extensive maintenance. Conventional SEMs required mounting the electron-optics column and sample chamber on an air table with a standard desktop personal computer adjacent to the microscope for user control. These instruments had to be housed in a dust-free environment, preferably on the ground/basement level within a building. Users had to manually control many aspects of the instrument during imaging. Specimens had to be vacuum compatible or risk significant degradation to the contamination-sensitive electron-optical components.

Developments in SEM instrumentation during the 1990s and 2000s produced compact SEMs, which are smaller and more robust instruments, including some that are portable for remote analysis. More powerful computers, automated stages, and automated SEM control enabled significant advances in high-throughput analysis. Focused ion beams were combined with SEM to produce dual-beam instruments. Specially designed SEMs, called variable-pressure/environmental SEMs, are equipped with differential pumping so the specimen chamber can operate under higher background pressure environments, a capability that accommodates high-vapor-pressure specimens inside the SEM, such as biological samples, polymers, and liquids.

Compact SEMs

During the 2010s, commercial SEMs were sufficiently scaled down in size so they can sit on a simple table. "Tabletop" instruments are largely self-contained and are relatively

easy to relocate. Often, the instruments are limited to x and y control with limited sample tilt capability. Sample sizes can be limited due to smaller specimen chamber sizes. Compact SEMs generally use thermionic sources and are limited to magnifications no higher than $\sim 50,000\times$. Nevertheless, the systems are designed for ease of use, require less maintenance, and are more user friendly for new users. Most compact SEMs connect to vacuum pumps displaced a few feet away. Many systems integrate a silicon-drift detector for EDS in addition to SE and BE detection using an annulus, pole-piece-mounted SSD, or scintillator detector.

Variable-Pressure/Environmental SEM

Variable-pressure/environmental SEMs (VP-ESEMs) are a specific class of SEM instruments that enable the user to flow gas to the specimen surface inside the SEM specimen chamber. Gas incorporation at the imaging site provides many advantages. Primary beam electrons ionize gas molecules, producing positively charged ions, which can balance negative charge accumulation during SEM imaging of an insulating sample surface. Thus, VP-ESEMs facilitate imaging of nonconducting specimen surfaces without the use of a conductive coating. The VP-ESEMs can also introduce water vapor to the specimen surface, suppressing evaporation for moist or liquid specimens inside the SEM chamber. User

control of gas type and local pressure enables SEM imaging of surface reactions occurring at the specimen surface, including oxidation, reduction, hydration, evaporation, corrosion, phase transformations, and so on.

The primary distinction for a VP-ESEM is differential pumping, the main objective of which is to keep as much of the primary electron beam pathway at extremely low pressures ($<1.33 \times 10^{-4}$ Pa, or $<10^{-7}$ torr) while also maintaining a much higher pressure (100 to 1000 Pa, or 0.75 to 7.5 torr) immediately at the specimen surface. To accomplish this, the VP-ESEM uses multiple pressure-limiting apertures (PLAs) to separate different pumping zones between the electron source and the specimen surface, as illustrated in Fig. 39. Each pumping zone is evacuated by its own pump. Ion getter pumps maintain the 1.33×10^{-6} Pa ($\sim 10^{-9}$ torr) pressure within the electron-optics column (zone 1), which constitutes most of the primary electron beam path to the sample. The next pumping zone (zone 2) includes the interior of the objective lens and a small distance between PLA 1 and PLA 2. This zone is maintained at a slightly higher pressure (0.133 to 0.0133 Pa, or 10^{-4} to 10^{-6} torr) by a turbomolecular pump. Finally, the electron beam passes through PLA 2 and into the high-pressure (100 to 1000 Pa, or 0.75 to 7.5 torr) zone 3 inside the SEM specimen chamber. An external source provides the desired background gas (water vapor, oxygen, argon, nitrogen, etc.) through an inlet attached to the specimen chamber.

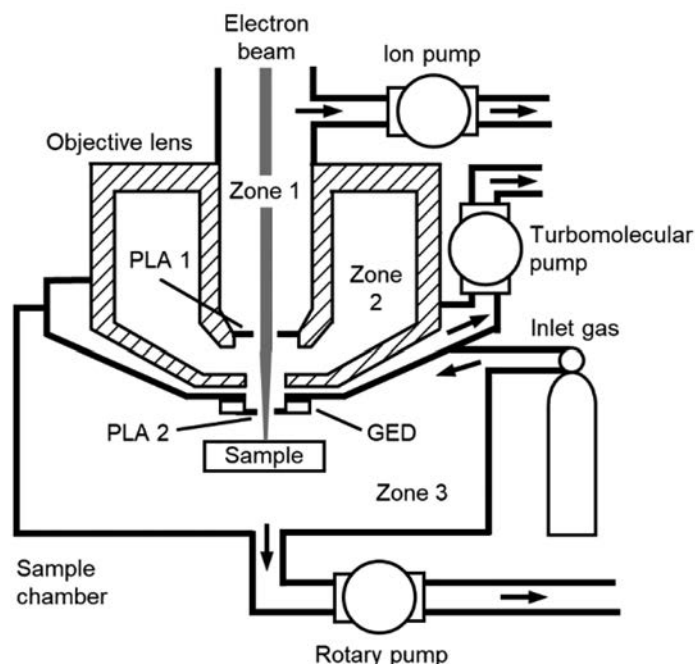


Fig. 39 Schematic illustration of a variable-pressure scanning electron microscope system with three distinct differentially pumped pressure zones: zone 1 (1.33×10^{-4} to 1.33×10^{-6} Pa, or 10^{-7} to 10^{-9} torr), zone 2 (0.133 to 0.0133 Pa, or 10^{-4} to 10^{-6} torr), and zone 3 (100 to 1000 Pa, or 0.75 to 7.5 torr). Each zone is separated by a pressure-limiting aperture (PLA). GED, gaseous electron detector

The primary electron beam path inside zone 3 must be minimized, because the gas molecules significantly increase primary electron scattering prior to their arrival at the specimen surface; thus, the smallest WD must be used. Specialized gaseous electron detectors (GEDs) can be mounted at the bottom of the objective lens pole piece to extend zone 2 closer to the sample surface. The bottom surface of a GED consists of silicon-drift detectors or scintillator detectors for high-take-off-angle SE and BE collection. Alternatively, a narrow conical component with a PLA at the nose can be mounted at the bottom of the objective lens pole piece. The conical component ensures extension of zone 2 right to the sample surface, as well as clear line of sight for x-ray spectroscopic analysis during VP-ESEM operation. See Example 6 in the section “Applications” in this article for an example experiment using a VP-ESEM. An excellent resource covering VP-ESEMs can be found in Ref 15.

High-Throughput Instruments

Developments in SEM design enabled automated acquisition of images and spectral analysis over numerous locations of a specimen surface. A multibeam SEM separates a single, high-current primary electron beam into dozens of individual lower-current primary beams. The primary beams are scanned in parallel across different points of the specimen surface. Individual detectors for each primary beam collect SEs that emanate from each primary beam location. In this manner, dozens of SEM images can be acquired in parallel over $\sim 100\ \mu\text{m}$ field of view, with each image containing sufficient pixels to resolve $<10\ \text{nm}$ details (Ref 52).

A particle analyzer is a specific class of SEM designed for automated, coordinated imaging and spectroscopic analysis (Ref 53). After recording an SE/BE image, contrast is interpreted and analyzed by the computer to identify particle types based on grayscale values and/or particle size/morphology. With input from the user regarding particles of interest, point EDS analysis is performed for different particle classifications to assign quantified composition to different particles. Next, automated SE/BE imaging and EDS analysis is performed over additional specimen locations, producing large-scale maps and highly statistically significant details regarding the morphologies and compositions for hundreds or even thousands of individual particles. See Example 1 in the section “Applications” in this article for an example study using particle analyzers.

Dual-Beam Instruments

Dual-beam instruments combine SEM with focused ion beam (FIB), another scanning beam instrument (Ref 54). Focused ion beams

generate and accelerate beams of ionized atoms (typically gallium or xenon) to high energies (2 to 30 keV). The ion beams can be electrostatically focused and scanned across a sample surface in a manner similar to scanned electron beams. The FIBs are capable of controllable deposition of materials by a process called ion-beam-assisted chemical vapor deposition (CVD). The process uses the ion beam to stimulate CVD reactions at the surface while a reactive precursor gas is injected at the sample site using a nozzle. Additionally, FIBs direct high-energy ions to controllably remove, or sputter, material away from the sample. Because the 2 to 30 keV ion beam can be focused to $<10\ \text{nm}$ spot sizes, FIB sputtering is similar to atomic sandblasting or nanoscale milling.

Enabling site-specific, cross-sectional SEM is a major advantage of a dual-beam instrument. The instruments enable deposition of a protective layer over a region of interest, nanoscale precision sputtering of unwanted material adjacent to the region of interest, and SEM imaging/analysis of the newly revealed surface. Dual-beam instruments have automated control of the ion beam, electron beam, and stage for three-dimensional analysis. Surfaces can be ion milled, imaged, and ion milled again to form a new surface for subsequent imaging. The process is repeated hundreds or thousands of times, so numerous SEM images can be obtained and combined to reconstruct the three-dimensional physical characteristics of the material. Dual-beam instruments are commonly equipped with nanomanipulators so that thin specimens can be removed and mounted to predesigned sample holders. Thus, dual-beam instruments are often used for site-specific preparation of specimens for the TEM, transmission-mode SEM, and atom probe tomography. See Example 6 in the section “Applications” in this article for an example cross-sectional analysis by FIB milling. For more details on FIBs and dual-beam instruments, see the article “Focused Ion Beam Instruments” in this Volume.

Ultrahigh-Resolution SEMs

Ultrahigh-resolution (UHR) is a general term used in reference to SEMs specifically designed for the highest point resolution obtainable using current technology. The UHR-SEMs typically use cold field-emission guns to obtain maximum brightness, β , as well as minimum primary beam energy spread, or chromatic aberration. The UHR-SEMs use either immersion lens or snorkel lens configurations to minimize WD and minimize spherical aberration, C_s . The UHR-SEM instruments use extensive vibration damping and electromagnetic field shielding, yet they still require stringent ambient conditions with minimal external vibrations and electromagnetic fields. Sample size can be limited, especially for cases where an immersion lens is used.

Nevertheless, the SEM immersion lens configuration is similar to TEM, so transmission-mode SEM can be readily implemented in certain UHR-SEMs; scanning TEM detectors are often available in UHR-SEMs for transmission-mode imaging (Ref 55). As mentioned in Table 3, UHR-SEMs can achieve point resolution down to 0.3 nm.

Applications

This section presents examples in which SEM instruments are used for particle analysis, EBSD analysis, EDS and contrast by electron channeling, monochromatic CL imaging and ECCI, transmission-mode SEM, and in situ investigation using an environmental SEM.

Example 1: EDS for Steel Inclusion Analysis

Molten steel contains dissolved oxygen, which can form unwanted porosity during solidification. Aluminum added to molten steel captures the oxygen, typically forming spinel inclusions, which are solid solutions of MgAl_2O_4 and Al_2O_3 . High-melting-temperature inclusions present a problem where the ceramic particles can agglomerate and degrade crucial components of the steel casting process. Calcium treatment of the molten steel serves to partially or completely liquefy the spinel inclusions. This study used particle analyzers to investigate the morphology and composition of spinel inclusions at various stages of the calcium treatment process. Particle analyzers, combining automated SEM with EDS, are well established for analyzing steel inclusions (Ref 53).

Two SEMs operating at 20 kV acceleration voltage were used to study inclusions in cross-sectioned steel samples from laboratory tests and industrial casting operations. Figure 40 (a) presents SE images of the spinel inclusions at various stages of calcium treatment. Inclusion sizes ranged from 1 to $2.5\ \mu\text{m}$. The calcium addition initially converted faceted Mg-Al-O spinel inclusions to a transient Al_2O_3 -CaS combination, or a rarely observed spinel-CaS combination. After 4 to 5 min of calcium treatment, spinel inclusions were either partially or fully liquefied, with the liquid phase being lower $\text{MgO-Al}_2\text{O}_3$ mixtures. The results indicate that calcium modifies the spinel inclusions through a transient calcium sulfide formation process, with magnesium eventually dissolving into the steel. Figure 40(b) further illustrates the phenomenon through analysis of hundreds of inclusions for three industrial samples: ladle 1 (no calcium), ladle 2 (immediate calcium treatment), and ladle 3 (5 min after calcium treatment). Initial inclusion compositions for ladle 1 are either Al_2O_3 or MgAl_2O_4 - Al_2O_3 . Inclusion compositions in ladles 2 and 3

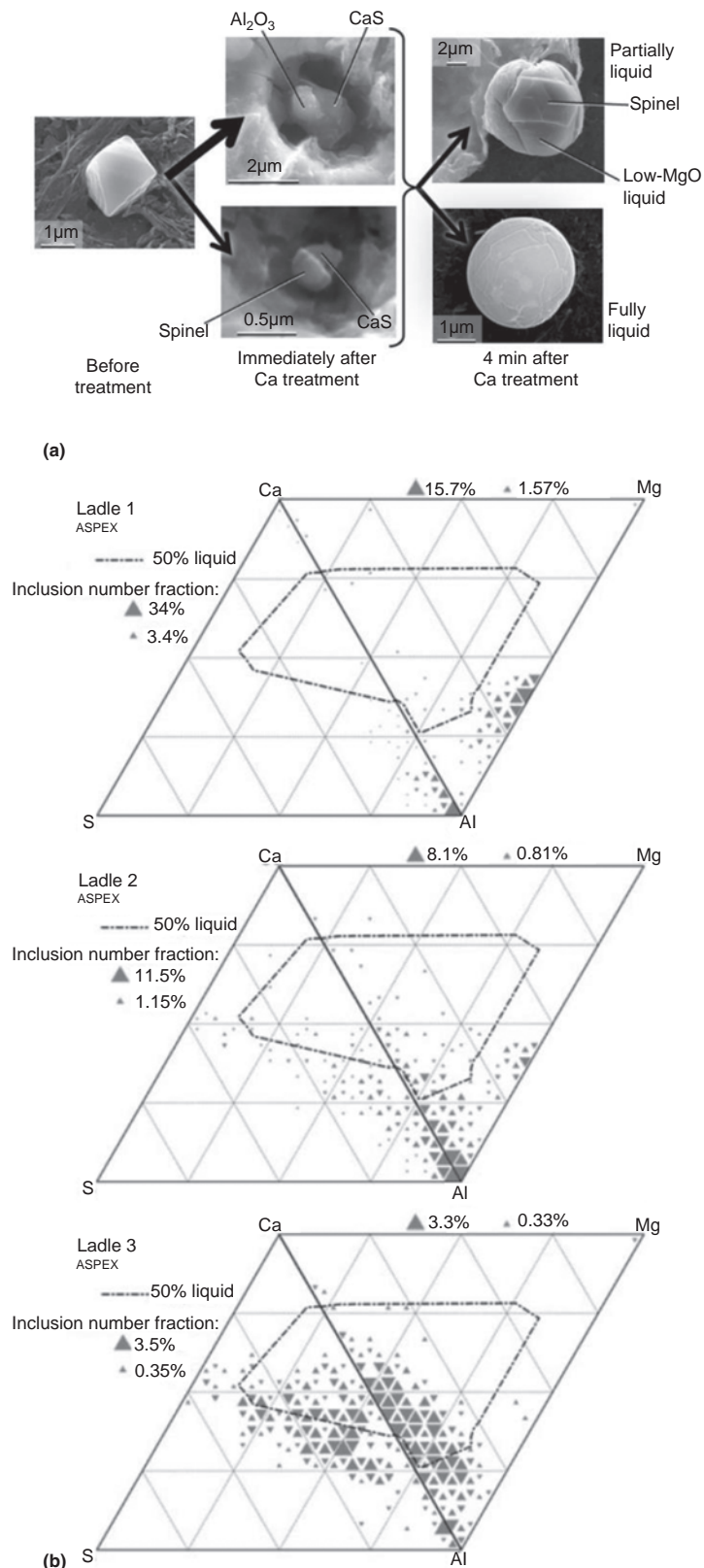


Fig. 40 (a) Secondary electron images of spinel inclusions at various stages of calcium treatment in molten steel. (b) Inclusion compositions for industrial samples before calcium treatment (ladle 1), immediately after calcium treatment (ladle 2), and 5 min after calcium treatment (ladle 3). Source: Ref 56

exhibit depletion of magnesium with calcium treatment. The formation of CaS occurs immediately upon calcium incorporation and then decreases over time as the inclusions exhibit predominantly calcium aluminate compositions after 5 min of calcium treatment. An important implication from this study was that while calcium treatment demonstrated liquefaction of spinel inclusions, magnesium dissolved back into the steel and could serve to form new, unwanted spinel inclusions in the molten steel. The particle analyzer SEMs in this study enabled morphological and compositional analysis of hundreds of micrometer-scale particles to obtain these insights. More details on this study can be found in Ref 56.

Example 2: EBSD and Fractography for Additive Manufacturing

This example highlights the use of EBSD and fractography to correlate fracture behavior and tensile strength to the microstructure of Ti-6Al-4V specimens produced by additive manufacturing (AM). Ti-6Al-4V is an alloy with a high strength-to-weight ratio and good corrosion resistance and is widely used in aerospace and biomedical applications. This dual-phase alloy is composed of a hexagonal close-packed α phase and a body-centered cubic β phase. Depending on the cooling rate from the higher-temperature β -phase region (above 995 $^{\circ}\text{C}$, or 1820 $^{\circ}\text{F}$) through the $\alpha + \beta$ region, α -phase microconstituents can form globular morphologies or Widmanstätten platelets. Sufficiently fast cooling can produce martensitic phases, including a hexagonal α' structure. The mechanical properties can vary significantly based on the thermal history and resultant α - β microstructure.

Selective laser melting (SLM) is a type of AM process that uses a scanned laser to melt controllably fed powder in a layer-by-layer process. Local microstructure can be tailored by controlling laser conditions and feed powder. A study was conducted to explore the mechanical properties of SLM-produced Ti-6Al-4V samples fabricated under various build orientations. Starting powder was plasma-atomized Ti-6Al-4V consisting entirely of the α' phase. During SLM, melting and resolidification of the powders determined the β grain size and texture as well as the eventual α -phase formation during cooling.

Inverse pole figure (IPF) maps obtained by the EBSD method show both the orientations of the hexagonal α phase and a reconstructed IPF map for the prior- β -phase grains. Electron backscatter diffraction was performed for specimens produced at different build orientations by SLM to evaluate both α - and β -phase grain size and texture. For all SLM build orientations, prior- β phase exhibited a dominant (100) solidification texture.

Fractography was performed using SE imaging on fracture surfaces of specimens tensile stressed to failure, as shown in Fig. 41. At higher magnifications, terracelike features were observed, denoted by the black arrows in Fig. 41(b). The terrace size and aspect ratio were consistent with prior- β grains and seemed to indicate crack propagation through prior- β grains. Additionally, it was found that fracture surface profiles differ significantly based on build profile primarily due to prior- β grain-boundary orientation with respect to the external axial loading direction during tensile testing. Ultimately, AM-produced Ti-6Al-4V specimens appeared to be dominated by intergranular-mode fracture along α grain boundaries and along prior- β grain boundaries. In this study, the coordination between EBSD and SE imaging in the SEM was critical in elucidating the mechanical behavior of these AM-produced specimens. More details of this study can be found in Ref 57.

Example 3: EDS and Electron Channeling for High-Entropy Alloys

This example demonstrates coordinated SEM analysis using EBSD, EDS, and electron channeling to investigate the microstructure of a high-entropy alloy (HEA). The HEAs are alloys formed by mixing multiple elemental components, resulting in a crystal structure consisting of elements occupying random locations in the lattice. Interest in HEAs is increasing due to their unusual structure-property relationships and potential superior performance over conventional alloys.

A study was conducted to investigate the addition of interstitial carbon to an HEA. Figure 42 presents SEM analysis of an $\text{Fe}_{49.5}\text{Mn}_{30}\text{Co}_{10}\text{Cr}_{10}\text{C}_{0.5}$ (at.%) HEA after cold rolling and recrystallization annealing. Electron backscatter diffraction, shown in Fig. 42(a), confirmed the HEA was primarily face-centered cubic (fcc) with an $\sim 4\ \mu\text{m}$ average grain size and that twins were present. The EBSD phase map with grain boundaries was correlated to a BE image (Fig. 42b), showing grain orientation contrast via the electron channeling mechanism. The white circles in Fig. 42(b) denote dark particles confirmed by EDS in Fig. 42(c) to be iron-deficient and chromium-rich. Coordinated analysis by atom probe tomography confirmed increased carbon content for these chromium-rich particles. Results indicate that the presence of carbon provided an avenue for forming nanoscale chromium carbides within the HEA microstructure.

Room-temperature mechanical testing indicated improved tensile strength compared with HEAs with similar compositions that did not contain carbon. The mechanical property improvement was tied to the existence of multiple deformation mechanisms for the new alloy composition, including interstitial solid-solution strengthening, microcomposite effects

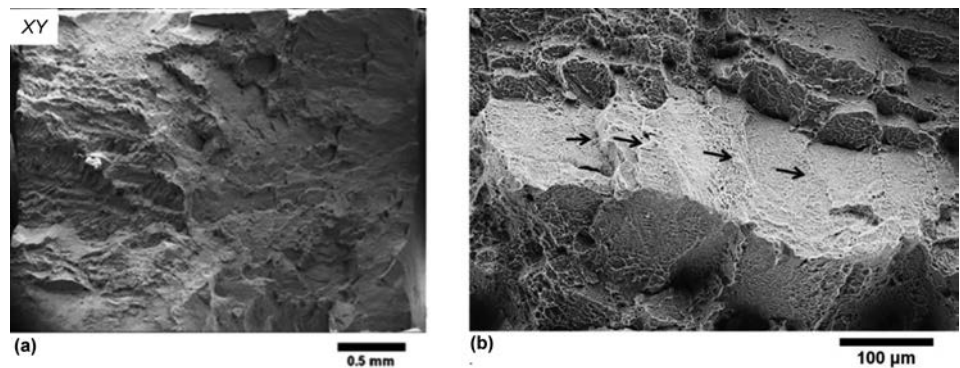


Fig. 41 Scanning electron micrographs by secondary electron detection of a fractured additive-manufacturing-produced Ti-6Al-4V specimen obtained at (a) lower and (b) higher magnifications. Black arrows in (b) denote terraces speculated to occur at prior- β grain boundaries. Reprinted from Ref 57 with permission of Elsevier

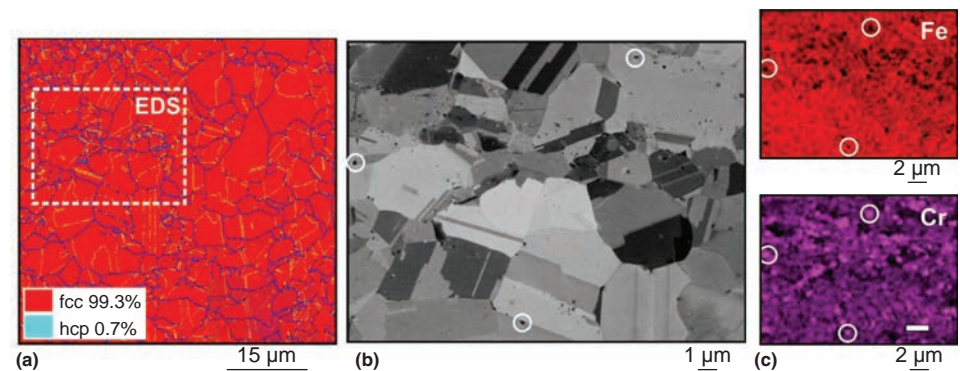


Fig. 42 Coordinated scanning electron microscope analysis of an Fe-Mn-Co-Cr-C high-energy alloy. (a) Electron-backscatter-diffraction-produced phase map with grain boundaries (blue lines) and twin boundaries (yellow lines). EDS, energy-dispersive spectrometry; fcc, face-centered cubic; hcp, hexagonal close-packed. (b) Backscattered electron micrograph of the region highlighted by dotted lines in (a). White circles in (b) denote iron-depleted and chromium-rich regions, as confirmed by (c), which is EDS elemental mapping. Reprinted from Ref 58 under a Creative Commons Attribution 4.0 International License

due to a dual-phase structure with the formation of a hexagonal close-packed (hcp) phase, nanotwinning-induced plasticity, and formation of extended defects such as stacking faults and dislocations. The use of EBSD and x-ray diffraction could confirm the dual-phase nature of this HEA, quantifying the hcp phase as a function of processing conditions and tensile deformation. However, ECCI could also confirm that the hcp phase, when at low phase fractions, existed as a lamellar structure with associated stacking faults within the fcc matrix. Twinning, stacking fault formation, and dislocation formation were also imaged by ECCI and correlated to deformation behavior. All of these insights required the application and coordination of multiple SEM modes (EBSD, ECCI, EDS). More details on this study can be found in Ref 58.

Example 4: CL and ECCI for Wide-Bandgap Semiconductors

Reducing extended defects in GaN, AlN, and InN is an important way to improve the

quantum efficiency of green, blue, and ultraviolet light-emitting diodes. Directly confirming the luminescence behavior of extended defects is an important goal in this field. Coordinating two SEM-based methods, ECCI and CL, provides a direct correlation between individual defects and the local luminescence behavior. Figure 43(a) presents ECCI images of a silicon-doped GaN single-crystal film deposited by metal-organic vapor-phase epitaxy onto a *c*-plane sapphire substrate. The dark/light features in the ECCI micrograph denote vertically oriented line defects, dislocations that have threaded along the *c*-axis of the GaN wurtzite structure and penetrated the (0002) surface. The same region is analyzed using room-temperature monochromatic CL imaging, shown in Fig. 43(b), using integrated light signal intensity centered near $\sim 3.4\ \text{eV}$. Dark spots in the CL map exhibit one-to-one correlation with the dislocation positions determined by ECCI. The coordination of two SEM techniques, ECCI and CL, succeeds in confirming the nonradiative recombination behavior associated with these dislocations. More details regarding this study can be found in Ref 59.

Example 5: Transmission-Mode SEM for Nanoparticles

Nanoparticles range in size from 1 to 100 nm and exhibit a host of unique properties, depending on composition, shape, morphology, and surface structure. Different SEM detectors are used to determine various nanoparticle characteristics. Figure 44 presents SEM micrographs of gold and TiO₂ nanoparticles on a lacey carbon substrate using 20 kV acceleration voltage. Figure 44(c) is an SE image recorded using an in-lens detector. Both isolated nanoparticles and agglomerates are visible, but there is no obvious delineation between the gold and TiO₂ nanoparticles. A modular aperture system (Ref 9) enabled angular selectivity for a commercial SSD positioned below the sample. The result was transmission SEM images produced by collecting electrons over a specific half-angle range, 24 to 48 milliradians in Fig. 44(a) and 496 to 547 milliradians in Fig. 44(b). The larger atomic number of gold can appreciably scatter more electrons in the larger-collection half-angle than the TiO₂ nanoparticles. Thus, the bright features in Fig. 44(b) can be identified as individual gold nanoparticles. For the smaller-collection half-angle image in Fig. 44(a), gold nanoparticles exhibit a more complex contrast (Ref 10), while the TiO₂ nanoparticles, denoted by white arrows, yield uniform bright intensity. Higher-magnification micrographs (not shown here) highlight the superior atomic number (*Z*) contrast for a transmission-mode SEM compared with conventional BE imaging. This study highlights potential advantages in using a transmission mode while also demonstrating the capability of SEM in resolving different nanoparticles. More details regarding this study can be found in Ref 9.

Example 6: Environmental SEM, FIB, and In Situ Heating for Iron Oxidation

Oxidation of metals, such as iron, is investigated in situ by using an environmental SEM (ESEM) in conjunction with a heating stage. An advantage of this approach is the observation of oxidation as a function of local metal grain orientation. Figure 45(a) presents an SEM image of an iron sample prior to oxidation experiments. Individual grains were delineated by their orientation based on the channeling contrast visible due to foreshattered electron (FSE) detection. The SSDs used for FSE detection were mounted on an EBSD system, so the sample was tilted to 70° for FSE imaging. During in situ heating, the sample was at 0° tilt and was imaged using a special heat- and light-insensitive SE detector. A commercial ESEM facilitated in situ exposure to water vapor, dry air (<6 ppm H₂O), and wet air (1% H₂O) during heating.

After 1 h of exposure to water vapor at 500 °C (930 °F) inside the ESEM, different

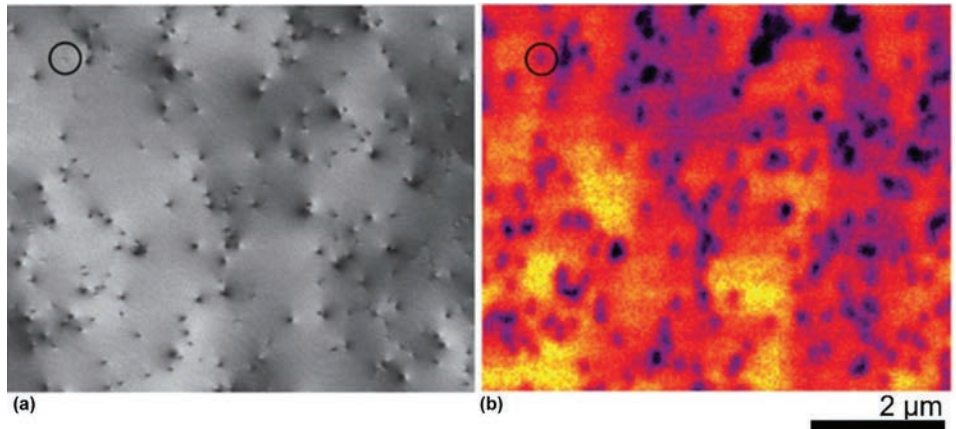


Fig. 43 Coordinated scanning electron microscope analysis of threading dislocations in a GaN (0002) single crystal using (a) electron channeling contrast imaging and (b) cathodoluminescence. Reprinted from Ref 59 with permission of Cambridge University Press

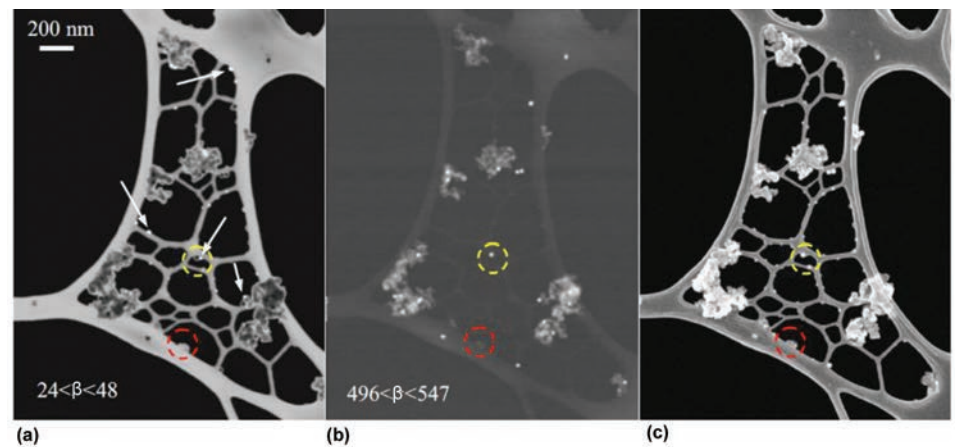


Fig. 44 Scanning electron micrographs of gold and TiO₂ nanoparticles on a lacey carbon substrate acquired at (a) low-angle and (b) high-angle transmission modes using a commercial solid-state detector, and (c) a conventional secondary electron image. Reprinted from Ref 9 with permission of Elsevier

oxide scales were observed for different iron grains, as shown in Fig. 45(b, c). Different oxide thicknesses were determined by using an FIB to cross section two adjacent iron grains. Figure 45(d) shows the thicker and thinner oxide scales revealed by FIB milling. Cross-sectional imaging using the FIB with SE detection provided ion channeling contrast of the iron oxide grain structure. These images (not shown here) revealed that the oxide layers consisted of three layers when ESEM reactions used dry and wet air: a porous magnetite layer, a fully dense magnetite layer, and a thin, fine-grained hematite layer. Oxidation experiments using water vapor showed only a duplex magnetite layer structure. The duplex structure suggested an initial magnetite microstructure lattice matched to the underlying iron grain; the magnetite then transitioned to a densified,

columnar magnetite microstructure. The columnar grains were larger for the water vapor oxidation case than for the wet/dry air oxidation case. This study demonstrates how an ESEM can monitor a process such as oxidation while also coordinating analysis using other SEM-related methods, such as FSE imaging and FIB milling, to correlate oxidation behavior to the local microstructure and oxidation conditions. Additional details of this study can be found in Ref 60.

ACKNOWLEDGMENT

Revised from John D. Verhoeven, Scanning Electron Microscopy, *Materials Characterization*, Vol 10, ASM Handbook, ASM International, 1986.

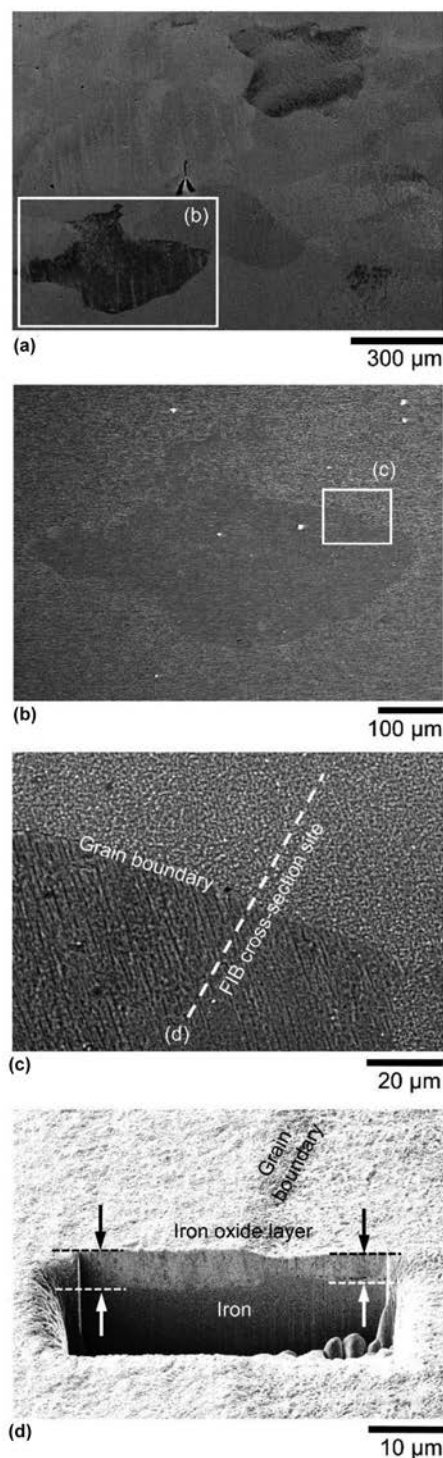


Fig. 45 (a) Forescattered electron micrograph of iron surface before oxidation. (b, c) Environmental scanning electron microscope/secondary electron micrographs during oxidation. (d) Secondary electron micrograph of focused ion beam (FIB)-milled cross section showing oxide scale thickness differences between adjacent grains. Adapted from Ref 60. Courtesy of T. Jonsson, Chalmers University of Technology

REFERENCES

1. M. Ardennevon, Das Elektronen-Rastermikroskop, *Z. Phys.*, Vol 109 (No. 9–10), Sept 1938, p 553–572
2. C.W. Oatley, The Scanning Electron Microscope, *Science Progress* (1933–), Vol 54, Science Reviews 2000 Ltd., 1966, p 483–495
3. C.W. Oatley, The Tungsten Filament Gun in the Scanning Electron Microscope, *J. Phys. E.*, Vol 8 (No. 12), Dec 1975, p 1037–1041
4. J.I. Goldstein et al., The SEM and Its Modes of Operation, *Scanning Electron Microscopy and X-Ray Microanalysis*, Springer US, Boston, MA, 2003, p 21–60
5. J. D. Verhoeven and E.D. Gibson, Evaluation of a LaB₆ Cathode Electron Gun, *J. Phys. E.*, Vol 9 (No. 1), Jan 1976, p 65–69
6. A.E. Vladár and M.T. Postek, The Scanning Electron Microscope, *Handbook of Charged Particle Optics*, CRC Press, 2017, p 437–496
7. T.E. Everhart and R.F.M. Thornley, Wide-Band Detector for Micro-Microampere Low-Energy Electron Currents, *J. Sci. Instrum.*, Vol 37 (No. 7), July 1960, p 246–248
8. V.N.E. Robinson, The Construction and Uses of an Efficient Backscattered Electron Detector for Scanning Electron Microscopy, *J. Phys. E.*, Vol 7 (No. 8), Aug 1974, p 650–652
9. J. Holm and R.R. Keller, Angularly-Selective Transmission Imaging in a Scanning Electron Microscope, *Ultramicroscopy*, Vol 167, Aug 2016, p 43–56
10. T. Woehl and R. Keller, Dark-Field Image Contrast in Transmission Scanning Electron Microscopy: Effects of Substrate Thickness and Detector Collection Angle, *Ultramicroscopy*, Vol 171, Dec 2016, p 166–176
11. D.C. Joy, C.S. Joy, and R.D. Bunn, Measuring the Performance of Scanning Electron Microscope Detectors, *Scanning*, Vol 18 (No. 8), Dec 1996, p 533–538
12. B.J. Griffin, A Comparison of Conventional Everhart-Thornley Style and In-Lens Secondary Electron Detectors—A Further Variable in Scanning Electron Microscopy, *Scanning*, Vol 33 (No. 3), May 2011, p 162–173
13. J.I. Goldstein et al., *Scanning Electron Microscopy and X-Ray Microanalysis*, Springer US, Boston, MA, 2003
14. L. Reimer, *Electron Optics of a Scanning Electron Microscope*, 1998, p 13–56
15. D.J. Stokes, *Principles and Practice of Variable Pressure/Environmental Scanning Electron Microscopy (VP-ESEM)*, John Wiley & Sons, Ltd., Chichester, U. K., 2008
16. B.L. Bramfitt and A.O. Benscoter, *Metallographer's Guide : Practice and Procedures for Irons and Steels*, ASM International, 2001
17. J.I. Goldstein et al., Image Formation and Interpretation, *Scanning Electron Microscopy and X-Ray Microanalysis*, Springer US, Boston, MA, 2003, p 99–193
18. D.C. Joy, Control of Charging in Low-Voltage SEM, *Scanning*, Vol 11 (No. 1), Jan 1989, p 1–4
19. A. Kolmakov, Membrane-Based Environmental Cells for SEM in Liquids, *Liquid Cell Electron Microscopy*, Cambridge University Press, 2016, p 78–105
20. M.T. Postek and A.E. Vladár, Does Your SEM Really Tell the Truth?—How Would You Know? Part 1, *Scanning*, Vol 35 (No. 6), Nov 2013, p 355–361
21. T.C. Isabell, P.E. Fischione, C. O'Keefe, M.U. Guruz, and V.P. Dravid, Plasma Cleaning and Its Applications for Electron Microscopy, *Microsc. Microanal.*, Vol 5 (No. 2), March 1999, p 126–135
22. P.W. Trimby, Orientation Mapping of Nanostructured Materials Using Transmission Kikuchi Diffraction in the Scanning Electron Microscope, *Ultramicroscopy*, Vol 120, Sept 2012, p 16–24
23. E.F. Rauch and M. Véron, Automated Crystal Orientation and Phase Mapping in TEM, *Mater. Charact.*, Vol 98, Dec 2014, p 1–9
24. P. Echlin, *Handbook of Sample Preparation for Scanning Electron Microscopy and X-Ray Microanalysis*, Springer US, Boston, MA, 2009
25. K. Kanaya and S. Okayama, Penetration and Energy-Loss Theory of Electrons in Solid Targets, *J. Phys. D. Appl. Phys.*, Vol 5 (No. 1), Jan 1972, p 308
26. H. Demers et al., Three-Dimensional Electron Microscopy Simulation with the CASINO Monte Carlo Software, *Scanning*, Vol 33 (No. 3), May 2011, p 135–146
27. J.I. Goldstein et al., Electron Beam-Specimen Interactions, *Scanning Electron Microscopy and X-Ray Microanalysis*, Springer US, Boston, MA, 2003, p 61–98
28. R.F. Egerton, *Electron Energy-Loss Spectroscopy in the Electron Microscope*, Springer, 2011
29. L. Reimer and M. Riepenhausen, Detector Strategy for Secondary and Backscattered Electrons Using Multiple Detector Systems, *Scanning*, Vol 7 (No. 5), Jan 1985, p 221–238
30. D. Tang, M.E. Ferreira, and P.C. Pistorius, Automated Inclusion Microanalysis in Steel by Computer-Based Scanning Electron Microscopy: Accelerating Voltage, Backscattered Electron Image Quality, and Analysis Time, *Microsc. Microanal.*, Vol 23 (No. 6), Dec 2017, p 1082–1090
31. J. Cazaux, On Some Contrast Reversals in SEM: Application to Metal/Insulator Systems, *Ultramicroscopy*, Vol 108 (No. 12), Nov 2008, p 1645–1652

32. S. Chung et al., Secondary Electron Dopant Contrast Imaging of Compound Semiconductor Junctions, *J. Appl. Phys.*, Vol 110 (No. 1), 2011, p 014902
33. V.G. Dyukov, S.A. Nepijko, and G. Schönhense, Voltage Contrast Modes in a Scanning Electron Microscope and Their Application, *Adv. Imag. Electron Phys.*, Vol 196, Jan 2016, p 165–246
34. J.I. Goldstein et al., Special Topics in Scanning Electron Microscopy, *Scanning Electron Microscopy and X-Ray Microanalysis*, Springer US, Boston, MA, 2003, p 195–270
35. D.C. Joy, D.E. Newbury, and D.L. Davidson, Electron Channeling Patterns in the Scanning Electron Microscope, *J. Appl. Phys.*, Vol 53, 1982,
36. Y.N. Picard, M. Liu, J. Lamatao, R.J. Kamaladasa, and M. De Graef, Theory of Dynamical Electron Channeling Contrast Images of Near-Surface Crystal Defects, *Ultramicroscopy*, Vol 146, 2014, p 71–78
37. S. Zaefferer and N.-N. Elhami, Theory and Application of Electron Channelling Contrast Imaging under Controlled Diffraction Conditions, *Acta Mater.*, Vol 75, Aug 2014, p 20–50
38. J. Guyon, H. Mansour, N. Gey, M.A. Crimp, S. Chalal, and N. Maloufi, Sub-Micron Resolution Selected Area Electron Channeling Patterns, *Ultramicroscopy*, Vol 149, Feb 2015, p 34–44
39. T. Maitland and S. Sitzman, Backscattering Detector and EBSD in Nanomaterials Characterization, *Scanning Microscopy for Nanotechnology*, Springer, New York, NY, 2006, p 41–75
40. J.I. Hanoka and R.O. Bell, Electron-Beam-Induced Currents in Semiconductors, *Ann. Rev. Mater. Sci.*, Vol 11, 1981, p 353–380
41. P.M. Haney, H.P. Yoon, P. Koirala, R.W. Collins, and N.B. Zhitenev, Electron Beam Induced Current in the High Injection Regime, *Nanotechnology*, Vol 26 (No. 29), July 2015, p 295401
42. F.J. García de Abajo, Optical Excitations in Electron Microscopy, *Rev. Mod. Phys.*, Vol 82 (No. 1), Feb 2010, p 209–275
43. P.R. Edwards and R.W. Martin, Cathodoluminescence Nano-Characterization of Semiconductors, *Semicond. Sci. Technol.*, Vol 26 (No. 6), June 2011, p 064005
44. J. Götze, Application of Cathodoluminescence Microscopy and Spectroscopy in Geosciences, *Microsc. Microanal.*, Vol 18 (No. 6), Dec 2012, p 1270–1284
45. G. Koschek, Origin and Significance of the SEM Cathodoluminescence from Zircon, *J. Microsc.*, Vol 171 (No. 3), Sept 1993, p 223–232
46. R. Podor, G.I.N. Bouala, J. Ravau, J. Lautru, and N. Clavier, Working with the ESEM at High Temperature, *Mater. Character.*, Vol 151, May 2019, p 15–26
47. C. Jiang, H. Lu, H. Zhang, Y. Shen, and Y. Lu, Recent Advances on In Situ SEM Mechanical and Electrical Characterization of Low-Dimensional Nanomaterials, *Scanning*, Vol 2017, Oct 2017, p 1–11
48. D.C. Joy and C.S. Joy, Low Voltage Scanning Electron Microscopy, *Micron*, Vol 27 (No. 3–4), June 1996, p 247–263
49. N. Brodusch, H. Demers, and R. Gauvin, Low Voltage SEM, *Field Emission Scanning Electron Microscopy*, Springer, 2018, p 37–46
50. R.F. Egerton, P. Li, and M. Malac, Radiation Damage in the TEM and SEM, *Micron*, Vol 35 (No. 6), Aug 2004, p 399–409
51. M. Konno, T. Ogashiwa, T. Sunaoshi, Y. Orai, and M. Sato, Lattice Imaging at an Accelerating Voltage of 30 kV Using an In-Lens Type Cold Field-Emission Scanning Electron Microscope, *Ultramicroscopy*, Vol 145, Oct 2014, p 28–35
52. A.L. Eberle, S. Mikula, R. Schalek, J. Lichtman, M.L.K. Tate, and D. Zeidler, High-Resolution, High-Throughput Imaging with a Multibeam Scanning Electron Microscope, *J. Microsc.*, Vol 259 (No. 2), Aug 2015, p 114–120
53. M. Reischl, G. Frank, C. Martinez, S. Aigner, B. Lederhaas, and S. Michelic, Automated SEM/EDX Particle Analysis to Determinate Non-Metallic Inclusions in Steel Samples: Round Robin Tests Aiming at Studying the Comparability of Results from Different Measurement Systems, *Pract. Metallogr.*, Vol 48 (No. 12), Dec 2011, p 643–659
54. L.A. Giannuzzi and F.A. Stevie, Ed., *Introduction to Focused Ion Beams*, Springer US, Boston, MA, 2005
55. C. Sun, E. Müller, M. Meffert, and D. Gerthsen, On the Progress of Scanning Transmission Electron Microscopy (STEM) Imaging in a Scanning Electron Microscope, *Microsc. Microanal.*, Vol 24 (No. 2), April 2018, p 99–106
56. N. Verma, P.C. Pistorius, R.J. Fruehan, M. S. Potter, H.G. Oltmann, and E.B. Pretorius, Calcium Modification of Spinel Inclusions in Aluminum-Killed Steel: Reaction Steps, *Metall. Mater. Trans. B*, Vol 43 (No. 4), Aug 2012, p 830–840
57. M. Simonelli, Y.Y. Tse, and C. Tuck, Effect of the Build Orientation on the Mechanical Properties and Fracture Modes of SLM Ti-6Al-4V, *Mater. Sci. Eng. A*, Vol 616, Oct 2014, p 1–11
58. Z. Li, C.C. Tasan, H. Springer, B. Gault, and D. Raabe, Interstitial Atoms Enable Joint Twinning and Transformation Induced Plasticity in Strong and Ductile High-Entropy Alloys, *Sci. Rep.*, Vol 7 (No. 1), Dec 2017, p 40704
59. G. Naresh-Kumar et al., Coincident Electron Channeling and Cathodoluminescence Studies of Threading Dislocations in GaN, *Microsc. Microanal.*, Vol 20 (No. 1), Feb 2014, p 55–60
60. T. Jonsson et al., An ESEM In Situ Investigation of the Influence of H₂O on Iron Oxidation at 500 °C, *Corros. Sci.*, Vol 51 (No. 9), Sept 2009, p 1914–1924